

**IMPROVING THE EXTRAGALACTIC DISTANCE  
SCALE USING CEPHEIDS IN M33**

**Victoria Scowcroft**  
**Astrophysics Research Institute**

A thesis submitted in partial fulfilment of the requirements of  
Liverpool John Moores University  
for the degree of  
Doctor of Philosophy.  
January 19, 2010

# **Declaration**

The work presented in this thesis was carried out at the Astrophysics Research Institute, Liverpool John Moores University. Unless otherwise stated, it is the original work of the author.

While registered as a candidate for the degree of Doctor of Philosophy, for which submission is now made, the author has not been registered as a candidate for any other award. This thesis has not been submitted in whole, or in part, for any other degree.

Victoria Scowcroft  
Astrophysics Research Institute  
Liverpool John Moores University  
Twelve Quays House  
Egerton Wharf  
Birkenhead  
CH41 1LD  
UK

JANUARY 19, 2010

# Abstract

Cepheids have been used as distance indicators for almost a century. Through their well defined period–luminosity relation, their distance can be found from their period of pulsation alone. However, in recent years, an important uncertainty has arisen in its calibration, namely the effect of metallicity on the period–luminosity relation.

It is important that we quantify this effect as Cepheids are used to tie down the base of the extragalactic distance scale. Without an accurate calibration for the nearest distances, the distances we measure for all other objects will be subject to systematic uncertainties. This thesis studies how the chemical composition of a Cepheid affects the zero-point of the period–luminosity relation, and quantifies the resulting change in measured distance modulus.

The first study uses Cepheids in two areas of M33; a sample from the metal–rich central region is compared with the more metal–poor sample from the southern spiral arm. Period–luminosity relations in the reddening–free Wesenheit index  $W_{vi}$  are constructed for the two samples and the measured distance moduli are compared. A significant offset is found between the two samples. Effects such as reddening and blending are ruled out, leaving the change in metallicity as the only possible explanation for the discrepancy.

The second study presented covers the whole of M33. Here, a sample of around 600 Cepheids is used, and the effect of metallicity on  $W_{gi}$  and  $W_{ri}$  is measured. The same conclusion is found; the change in composition significantly affects the measured distance modulus of the Cepheid and the period–luminosity relation must be changed to take this into account.

In addition, the Sloan band period–luminosity relations are derived empirically for the first time.

The metallicity gradient of M33 is also assessed. It is found that the slope must be steep, at least in the central few kpc of the galaxy, but may flatten off at larger radial distances.

# Publications

In the course of completeing the work presented in this thesis, the contents of Chapter 3 have been submitted and accepted for publication in a refereed journal:

Scowcroft, V., Bersier, D., Mould, J. R. & Wood, P. R., 2009, ‘The effect of metallicity on Cepheid magnitudes and the distance to M33’, *Monthly Notices of the Royal Astronomical Society*, 396, 1287.

# Acknowledgements

I would like to thank my supervisor David Bersier for all the support and encouragement he has given throughout my PhD, and for putting up with me throughout my data-reduction induced rages. Thank you for not laughing too much when I came up with my more special ideas. I hope that we will continue to work together in the future. I would also like to thank all the staff and students at the ARI, for all the discussions, lessons on how to do proper maths and general distractions that have enabled me to finish my thesis. Special thanks go to Dan, Stuart, Neil and Chris for all the times they have fixed my computer when I've tried to do something clever, and for getting my thesis back when I accidentally deleted it.

In addition to everyone at the ARI, who have all helped me in some way, I would like to thank the people who have given time to help me with the huge amounts of data reduction. In particular, Peter Stetson, Kris Stanek and Lucas Macri. Also thanks to Jean-Philippe Beaulieu, Jean-Baptiste Marquette and Joel Hartman for letting me use all their CFHT data after they did all the hard work at the start.

Finally, thank you to Chris for all the proof-reading and tea-making over the last few months. My trigonometry induced breakdowns haven't been easy, but thanks for putting up with me. And last but not least, thank you to my parents, especially for not complaining about the lack of visiting this year whilst I've been locked away with the computer.

The work presented in this thesis is based on observations made with the WIYN 3.5-m telescope, Kitt Peak National Observatory, National Optical Astronomy Observatories, which is operated by the Association of Universities for Research in Astronomy, Inc.

(AURA) under cooperative agreement with the National Science Foundation, observations made with MegaPrime/MegaCam, a joint project of CFHT and CEA/DAPNIA, at the Canada-France-Hawaii Telescope (CFHT) which is operated by the National Research Council (NRC) of Canada, the Institute National des Sciences de l'Univers of the Centre National de la Recherche Scientifique of France, and the University of Hawaii, in addition to observations made with the Isaac Newton Telescope operated on the island of La Palma by the Isaac Newton Group in the Spanish Observatorio del Roque de los Muchachos of the Instituto de Astrofsica de Canarias.

This research has made use of the NASA/IPAC Extragalactic Database (NED) which is operated by the Jet Propulsion Laboratory, California Institute of Technology, under contract with the National Aeronautics and Space Administration.

# Contents

<b>Declaration</b>	<b>ii</b>
<b>Abstract</b>	<b>iii</b>
<b>Publications</b>	<b>v</b>
<b>Acknowledgements</b>	<b>vi</b>
<b>Contents</b>	<b>viii</b>
List of Tables . . . . .	xiv
List of Figures . . . . .	xvi
<b>1 Introduction</b>	<b>1</b>
1.1 Why do we care about distances? . . . . .	1
1.1.1 Large scale distances . . . . .	1
1.1.2 Local distances . . . . .	2
1.2 The cosmological distance ladder . . . . .	3
1.2.1 Parallaxes . . . . .	3
1.2.2 The Cepheid distance scale . . . . .	4

1.2.3	Type Ia supernovae . . . . .	6
1.2.4	Surface brightness fluctuations . . . . .	7
1.2.5	Tully–Fisher relation . . . . .	8
1.3	Cepheid Variables . . . . .	9
1.3.1	Cepheid pulsations . . . . .	10
1.4	The Period–Luminosity Relation . . . . .	13
1.4.1	The linearity of the PL relation . . . . .	14
1.4.2	The possibility of a metallicity effect . . . . .	15
1.4.3	Theoretical metallicity studies . . . . .	20
1.4.4	Observational tests for the metallicity effect . . . . .	22
1.5	Overview of the thesis . . . . .	24
1.5.1	Why M33? . . . . .	24
1.5.2	WIYN survey . . . . .	25
1.5.3	CFHT survey . . . . .	26
1.5.4	Conclusions and Future Work . . . . .	26
<b>2</b>	<b>Photometry Pipeline</b>	<b>27</b>
2.1	Introduction . . . . .	27
2.2	CCDs . . . . .	28
2.3	Aperture Photometry . . . . .	29
2.4	PSF Photometry . . . . .	30
2.5	Photometry Software . . . . .	30
2.6	Pipeline Development . . . . .	32

2.6.1	Photometry procedures . . . . .	32
2.6.2	Initial parameters . . . . .	33
2.6.3	Star detection . . . . .	33
2.6.4	First pass photometry . . . . .	36
2.6.5	PSF modelling . . . . .	37
2.6.6	ALLSTAR photometry . . . . .	43
2.6.7	Automation . . . . .	44
2.7	ALLFRAME . . . . .	44
2.8	Calibration Steps . . . . .	49
2.8.1	Aperture Corrections . . . . .	49
2.8.2	Zero Points . . . . .	52
<b>3</b>	<b>WIYN survey of M33</b>	<b>53</b>
3.1	Introduction . . . . .	53
3.2	Observations . . . . .	54
3.3	Data Reduction . . . . .	56
3.3.1	Standard Calibration . . . . .	57
3.3.2	Astrometry . . . . .	59
3.4	The Catalogues . . . . .	62
3.4.1	Comparison with the Local Group Survey . . . . .	62
3.5	Cepheid Selection . . . . .	68
3.6	Cepheid Period–Luminosity Relations . . . . .	72
3.6.1	Extinction and reddening effects . . . . .	74

3.6.2	Reddening-Free Wesenheit Index . . . . .	80
3.6.3	Blending . . . . .	83
3.6.4	Period Distribution and Slope Changes . . . . .	85
3.7	Metallicity effects . . . . .	86
3.7.1	Effect of chosen metallicity gradient on $\gamma$ . . . . .	89
3.8	Conclusions . . . . .	94
<b>4</b>	<b>CFHT MegaCam Survey</b>	<b>96</b>
4.1	Introduction . . . . .	96
4.1.1	Canada-France-Hawaii Telescope and MegaCam . . . . .	98
4.2	Observations . . . . .	98
4.3	Preliminary data reduction . . . . .	98
4.4	Image subtraction . . . . .	99
4.4.1	Image subtraction on the CFHT data . . . . .	100
4.5	Cepheid Identification . . . . .	101
4.6	Calibration . . . . .	101
4.6.1	Isaac Newton Telescope and WFC . . . . .	102
4.6.2	INT observations . . . . .	102
4.6.3	INT Data Reduction . . . . .	102
4.6.4	SDSS Calibration . . . . .	104
4.6.5	Standard Calibration of the CFHT data . . . . .	106
4.7	Cepheid PL relations in Sloan bands . . . . .	107
4.7.1	Cepheid Selection . . . . .	108

4.7.2	Reddening Corrections . . . . .	109
4.8	Sloan Wesenheit Indices . . . . .	113
4.8.1	Metallicity effects . . . . .	114
4.9	Conclusions . . . . .	121
<b>5</b>	<b>Conclusions</b>	<b>123</b>
5.1	Overview of results . . . . .	123
5.2	Sloan band period–luminosity relations . . . . .	124
5.3	Metallicity effects on Wesenheit indices . . . . .	125
5.3.1	The effect on $W_{vi}$ . . . . .	125
5.3.2	The effect on $W_{gi}$ . . . . .	126
5.3.3	The effect on $W_{ri}$ . . . . .	127
5.3.4	The linearity of the PL relation . . . . .	128
5.4	Metallicity effects on $B, V, I_C$ . . . . .	131
5.5	The metallicity gradient of M33 . . . . .	131
<b>6</b>	<b>Future Work</b>	<b>133</b>
6.1	Metallicity corrections to the Wesenheit indices . . . . .	133
6.1.1	Addition of infra-red data . . . . .	135
6.2	Independent metallicity measurements . . . . .	135
<b>A</b>	<b>CFHT MegaCam Standard Solution</b>	<b>138</b>
<b>B</b>	<b>Fourier Analysis</b>	<b>142</b>
B.1	Fourier parameters . . . . .	142

B.2 Classification of M33 Cepheids . . . . .	143
--	-----

<b>Bibliography</b>	<b>145</b>
---------------------	------------

# List of Tables

1.1	Summary of results from Sandage et al. (1999)	21
1.2	Summary of results from Alibert et al. (1999)	22
2.1	WIYN pipeline parameters	35
2.2	Aperture photometry parameters for WIYN pipeline	37
2.3	WIYN ALLSTAR parameters	44
2.4	Comparison of ALLSTAR and ALLFRAME	45
2.5	Aperture correction parameters	50
3.1	Coordinates of WIYN M33 fields	56
3.2	Photometric solution of 1999 October 3rd for the Imager CCD	58
3.3	Photometric solution of 2000 October 3rd for the Mini-Mosaic Camera	59
3.4	Sample of weighted averages catalogue from the WIYN survey	63
3.5	Typical magnitudes and uncertainties from the weighted averages catalogue	65
3.6	Comparison of photometry with that of Massey et al. (2006)	68
3.7	$B, V, I_C$ period–luminosity relations for the two WIYN regions	72
3.8	Colour excesses derived from fits to Cepheid distance moduli	77

3.9	Confirmation of $R_V = 3.23$ reddening law using extinction terms and colour excesses . . . . .	80
3.10	Reddening-free $W_{vi}$ PL relations . . . . .	81
3.11	Comparison of $W_{vi} \mu s$ with de-reddened $B, V, I_C \mu s$ . . . . .	82
3.12	Comparison of LMC and MW PL relations . . . . .	95
4.1	Exposure times for CFHT observations . . . . .	98
4.2	Read noise and gain of INT WFC chips . . . . .	102
4.3	INT observations — 2008 October 7 . . . . .	103
4.4	INT photometry parameters . . . . .	105
4.5	Standard solution for INT SDSS observations . . . . .	106
4.6	Semi-empirical Sloan PL relations from Ngeow & Kanbur (2007) . .	108
4.7	Sloan band PL relations for the $Z_{LMC}$ sample . . . . .	110
4.8	Sloan dereddened PL relations from outer field . . . . .	113
4.9	$\gamma$ values from $W_{gi}$ and $W_{ri}$ PL relations and different metallicity gradients . . . . .	120
5.1	Summary of metallicity corrections found using different gradients . .	132
A.1	Transformation equation coefficients for CFHT MegaCam . . . . .	139

# List of Figures

1.1	Parallax illustration	4
1.2	Stellar evolution tracks for solar metallicity stars with $4M_{\odot} < M < 12M_{\odot}$ , over-plotted with MW, LMC and SMC Cepheids	11
1.3	Opacity contributions for metallicities between primordial and solar.	18
1.4	Evolution tracks stars with different masses and metallicities	19
2.1	Effect of seeing on the PSF shape	31
2.2	Photometry pipeline flowchart	34
2.3	Example PSF models	40
2.4	PSF star histogram — distribution according to field	41
2.5	PSF star histogram — distribution according to filter	42
2.6	Efficiency of the median	47
2.7	Example curve of growth	51
3.1	Regions of M33 observed in WIYN survey	55
3.2	Median stacked image for the inner field.	60
3.3	Median stacked image for the outer field.	61
3.4	Hess diagrams of M33 fields	64

3.5	Magnitude – $\sigma$ relation for $V$ in the outer field . . . . .	65
3.6	Comparison of Imager and Mini-Mosaic photometry — inner field . .	66
3.7	Comparison of Imager and Mini-Mosaic photometry — outer field . .	67
3.8	Comparison of photometry with Massey et al. (2006) — inner field . .	69
3.9	Comparison of photometry with Massey et al. (2006) — outer field . .	70
3.10	$B,V$ and $I_C$ PL relations — inner field . . . . .	73
3.11	$B,V$ and $I_C$ PL relations — outer field . . . . .	73
3.12	Comparison of CCM reddening law with a linear model . . . . .	76
3.13	Reddening determination for the inner field . . . . .	78
3.14	Reddening determination for the outer field . . . . .	79
3.15	Reddening-free $W_{vi}$ PL relations . . . . .	82
3.16	Period distribution of Cepheid samples . . . . .	85
3.17	$W_{vi}$ PL relation fit using $\log P < 1$ criteria. . . . .	87
3.18	Measured distance modulus for each Cepheid as a function of deprojected galactocentric distance and metallicity. . . . .	90
3.19	Comparison of different metallicity gradients . . . . .	93
4.1	Colour–composite image of M33 taken with MegaCam . . . . .	97
4.2	Orientation of the INT WFC chips . . . . .	103
4.3	Period distributions of CFHT Cepheids at different metallicities . . .	111
4.4	Sloan band PL relations for the $Z_{LMC}$ sample . . . . .	111
4.5	CFHT outer field $g'r'i'$ PL relations . . . . .	112
4.6	Sloan band Wesenheit PL relations for $Z_{LMC}$ sample . . . . .	115

4.7	Wesenheit PL relations for the entire sample . . . . .	116
4.8	Histograms of deviations from PL relation . . . . .	117
4.9	Change in measured $\mu$ with deprojected galactocentric distance . . . .	119
5.1	Proof of the linearity of the $W_{gi}$ PL relation . . . . .	129
5.2	Proof of the linearity of the $W_{ri}$ PL relation . . . . .	130
6.1	Petersen diagram for double mode Cepheids in different galaxies . . .	137
B.1	Fourier parameters of M33 Cepheids . . . . .	144

# Chapter 1

## Introduction

### 1.1 Why do we care about distances?

In this work, observations of Cepheid variables in the M33 galaxy are used in order to improve the accuracy of the extragalactic distance scale. But why do we care about the distance scale? The foundation of generally accepted cosmological models is that the Universe is isotropic and homogeneous; our position within it is not special. If this is the case, why would we need to know how near or far away anything is relative to us? There are two answers to this question, concerning both the large and small<sup>1</sup> scales.

#### 1.1.1 Large scale distances

The first answer to the question “Why do we care about distances?” can be traced back to the dawn of time — the Big Bang. The Universe is postulated to have originated in the Big Bang, when it exploded from a single, infinitely small point, continuously expanding into what we know today.

In his famous 1929 paper Hubble discovered that the distance of a galaxy is directly related to its recession velocity. He found that the further away a galaxy is, the faster it

---

<sup>1</sup>astronomically speaking

is moving away from us. This is direct evidence that the universe is still expanding. By plotting distance vs recession velocity the rate of expansion can be determined. This is what we now refer to as the Hubble constant ( $H_0$ ).

Since the time of Hubble’s discovery great advances have been made in the study of distances, and the value of  $H_0$  is known to within 5%. This is a giant leap forward from the factor-of-two problem that plagued the field just two decades ago. Although Cepheid measurements alone cannot give us  $H_0$  to 5%, even when combined with the large distance baseline of supernovae, using them in combination with measurements of other cosmological features such as baryon-acoustic-oscillations and the cosmic-microwave-background provides the extra constraints needed to bring the uncertainty down. Once an accurate value of  $H_0$  is obtained, the uncertainties on other important values such as the equation of state parameter,  $w$ , and the density parameters  $\Omega_{matter}$  and  $\Omega_\Lambda$  will also be reduced. Therefore, it is imperative that we improve our knowledge of the distance scale if we wish to expand on our knowledge of the Universe as a whole.

### 1.1.2 Local distances

You may now ask, “If we know about distances on a large scale, why do we need to know about the small scale?”. With the advent of large telescopes we can observe objects such as quasars, galaxies, supernovae and so on at high redshifts, so why are local distances so important? The answer is simple — stars. Galaxies, however big, far away and fancy looking they are, are all made up of stars. To really understand what is going on inside them we need to understand the stars. In most galaxies the individual stars cannot be resolved, but in our Local Group we can study resolved stellar populations.

Stars are far from simple objects, but our observations of them can be summed up in three quantities, brightness, colour and radius. Colour is fine, the colour we observe is independent of distance. Brightness and radius are a different story altogether.

In an observational context, the brightness of a star is measured by its apparent mag-

nitude. But, as we know from the inverse–square law, the brightness observed at a distance from the star will not be equal to its *intrinsic* brightness. Radius measurements have the same problem. This observation was perhaps best summarised by Father Ted Crilly, in his famous quote “These cows are very small, but those cows are far away”. Stars that are further away will appear smaller, so to know the true radius we must know the distance.

To properly quantify the intrinsic properties of a star, such as its luminosity, temperature and size, we must combine our observed values with its distance.

## 1.2 The cosmological distance ladder

Measurements of distances to objects within our Universe are all linked by the cosmological distance ladder. That is, distances of nearby objects are used to calibrate the distances of things further away. This means that our measurements for the furthest objects can only be as good as the determination of the nearest object, be it an individual star, stellar cluster or galaxy. Only by pinning down the bottom rung of the cosmological distance ladder can we know the true distance to the top. The work presented in this thesis aims to improve the constraints on the bottom rung, and hence the extragalactic distance scale as a whole.

### 1.2.1 Parallaxes

Parallaxes are the geometrically most straight forward way to measure the distance to the nearest of astronomical objects. Using a baseline of known length and observing the object in question from either side, it is simple to construct a geometric solution for the distance. This is illustrated in Figure 1.1. By taking observations of an object spaced by 6 months, so that the Earth is at opposite sides of its orbit, the apparent distance that the object moves,  $\theta$  (in arcsec), can be measured. This is equal to twice the parallax angle,  $\pi$ . Using simple trigonometry, the distance of the object can be

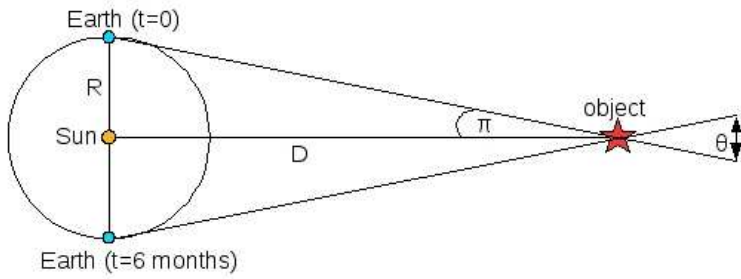


Figure 1.1: Using parallax measurements to determine distances. The distance that an object appears to move between observations spaced by 6 months ( $\theta$ ) can be used to derive the distance to the object by using a baseline of 2 AU, such that  $D = \frac{R}{\tan \pi}$

found by setting  $R = 1$  AU, such that

$$D = \frac{R}{\tan \pi}. \quad (1.1)$$

Ground based parallax measurements are limited by the observing conditions, and can be used to measure distances up to around 50 pc. The HIPPARCOS mission overcame this problem by taking space-based parallax measurements. They were able to measure parallaxes with accuracies of 1 milli-arcsec, and distances up to 1 kpc.

Parallaxes are useful by themselves; they can determine local distances to a high degree of accuracy, without the need to correct for extinction (which is, at least in the Galactic plane, a loose function of distance). However, the power of the parallax method can be increased by applying it to objects which are themselves distance indicators — namely Cepheid variable stars.

### 1.2.2 The Cepheid distance scale

Observations of Cepheids go back over two centuries, but surprisingly did not begin with the prototype  $\delta$  Cep. In 1784 Edward Pigott discovered the variability of  $\eta$  Aquilae. Although other variable stars were known at this time this was the first Cepheid. It was not until a month later that John Goodricke, Pigott's collaborator,

discovered the variability of  $\delta$  Cep (Goodricke & Bayer, 1786). As  $\delta$  Cep was circum-polar Goodricke observed it every night for many months. He calculated the period to be 5.14 days, very close to the 5.37 days we know it to be today, and efficiently described the shape of the Cepheid light curve. However, his gruelling observation schedule led to him developing pneumonia and dying in 1786.

The first inference of a relation between period and luminosity was from Leavitt (Leavitt & Pickering, 1912), who noted that “...the brighter variables have the longer periods.”. This simple observation is the reason that Cepheids are such important objects today. The period of pulsation for Cepheids is known to be strongly linked to their average luminosity, via the period–luminosity (PL) relation:

$$M = a \log P + b, \quad (1.2)$$

where  $M$  is the absolute magnitude,  $P$  is the period of pulsation, and  $a$  and  $b$  are constants which depend on the passband.

This is an extremely useful relation as, if  $a$  and  $b$  are known,  $M$  can be derived from the period alone, which is an extremely simple quantity to measure. Using this in combination with the apparent magnitude of the Cepheid, its distance can be found using the equation

$$m - M - A = 5 \log d - 5 = \mu \quad (1.3)$$

where  $m$  is the apparent magnitude,  $A$  is the extinction (which may or may not be present),  $d$  is the distance in parsecs and  $\mu$  is the distance modulus. As mentioned above, this is only possible if both  $a$  and  $b$  are already known. The slope of the PL relation can easily be found using a sample of Cepheids at a common distance (such as in the Large Magellanic Cloud, for example); plotting  $m$  vs.  $\log P$  for even a relatively small sample will give a good estimate of  $a$ . However, the zero-point  $b$  is more difficult to determine; independent distance measurements of Cepheids are required. This is where parallax measurements come in. Using the apparent magnitude of a galactic Cepheid in combination with its parallax distance, Equation 1.3 can be used to derive the absolute magnitude. This can then be fed into Equation 1.2 to derive  $b$ .

As mentioned above, an important work on this subject is the HIPPARCOS Space Astrometry mission. In this, the HIPPARCOS satellite made observations of the positions of around 100,000 stars, including 223 type I Cepheids (Feast & Catchpole, 1997). The parallax measurements of the fundamental mode Cepheids were used to calibrate the PL zero-point (Groenewegen & Oudmaijer, 2000).

The HIPPARCOS results were superceded by the work of Benedict et al. (2007). This study used the Hubble Space Telescope Fine Guidance Sensors, originally designed purely for pointing the instrument, to measure high precision parallaxes of nine Galactic Cepheids, producing improved PL relations. The data were later combined with revised HIPPARCOS measurements by van Leeuwen et al. (2007) to further improve the precision.

The combination of the PL relation with parallaxes sounds like an ideal way to study the extragalactic distance scale. However, the parallax method can only be applied to nearby stars, and Cepheids can only be observed in galaxies nearer than 10s of Mpc. To investigate larger distances, different techniques utilising intrinsically brighter objects must be explored.

### 1.2.3 Type Ia supernovae

Type Ia supernovae (SNe) are also used as standard candles. Their peak brightness was found to be constant at  $M_{pg} = -18.6 + 5 \log(H_0/100)$ , where  $M_{pg}$  is the photographic magnitude and  $H_0$  is the Hubble constant (Kowal, 1968). More recent studies, such as Phillips (1993), have found that there is considerable dispersion in the peak absolute magnitude, ranging from  $\pm 0.8$  mag in  $B$  to  $\pm 0.5$  mag in  $I$ . Although this may seem like a problem for the supernova distance scale, the shape of the light curve is found to be correlated with the peak brightness, such that the intrinsically brighter SNe decline more slowly than the fainter ones. They also found that the colour of a SNe at maximum brightness is correlated with the decline rate, showing that the redder events are intrinsically fainter.

In a similar way to the parallax calibration of the PL relation, distances to nearby SNe host galaxies are calibrated using Cepheids. This is necessary, as although Cepheids are observable in some SNe galaxies, they are only visible to scales of the order of 10s of Mpc. On the other hand, SNe are around 14 magnitudes brighter, hence are visible to scales of Gpc. One of the highest redshift Ia SN observed to date was found to have a redshift of  $z = 1.2$  (Coil et al., 2000), hence a distance of 2.75 Gpc (assuming a Hubble constant of  $71 \text{ kms}^{-1} \text{ Mpc}^{-1}$ ). Therefore, once we have a hold on the absolute magnitude of SNe in Cepheid galaxies, the distance scale can be extended out to much greater distances.

#### 1.2.4 Surface brightness fluctuations

Unlike the previous methods, the surface brightness fluctuations (SBF) technique, first described by Tonry & Schneider (1988), uses the properties of stellar *populations*, rather than individual stars. The fact that galaxies are composed of a population of discrete stars can be taken advantage of, even when the stars themselves cannot be resolved. To demonstrate this, the methodology presented by Binney & Merrifield (1998)[p. 426] is followed.

Firstly, consider a galaxy observed with angular resolution  $\delta\theta$ . Each element  $\delta\theta \times \delta\theta$  will contain, on average,  $\langle N \rangle$  stars, where

$$\langle N \rangle = n(D\delta\theta)^2, \quad (1.4)$$

$n$  is the total number of stars in the galaxy and  $D$  is the distance. From this, the average total flux  $\langle F \rangle$  from each element can be determined:

$$\langle F \rangle = \langle N \rangle f = \frac{nL(\delta\theta)^2}{4\pi} \quad (1.5)$$

where  $f$  is the flux from an individual star, and  $L$  is its luminosity. On its own this cannot be used to obtain the distance, as  $D$  is not present in Equation 1.5; the statistics of the stellar spatial distribution must now be brought into play.

A reasonable first approximation is that each  $(\delta\theta)^2$  element will contain  $\langle N \rangle$  stars, and have  $\langle F \rangle$  flux. However, Poisson fluctuations will be present in the distribution of stars (and hence flux), giving the distribution of stars a dispersion of  $\sqrt{\langle N \rangle}$ . This does not translate directly to flux, instead the distance dependence returns:

$$\sigma_{\langle F \rangle} = \sqrt{\langle N \rangle} f = \frac{\sqrt{n}\delta\theta L}{4\pi D} \quad (1.6)$$

meaning that the Poisson noise in the flux is inversely proportional to the distance of the galaxy. Like the majority of distance indicators, this does not give an absolute distance. It is simple to see that the ratio of  $\sigma_{\langle F \rangle}$  for different galaxies will give a relative distance. Once again, to get an absolute value one of the distances must be calibrated using an independent indicator, such as Cepheids.

### 1.2.5 Tully–Fisher relation

The Tully–Fisher relation, like the SBF technique, uses properties of galaxies rather than stars to derive distances. In this case, the kinematics of the galaxy are used to derive a distance. The basis of this comes from the virial theorem. The virial theorem implies that the average orbital speed of material in a system increases with the mass of that system, i.e. the stars in a more massive galaxy will orbit the centre faster than in a lower mass galaxy. The logical progression of this is that, as the width of spectral lines increases with velocity, there will be a correlation between the width of the lines and the mass of the galaxy, once inclination effects have been taken into account. Combining this with the mass–luminosity relation, we arrive at the theoretical basis for the Tully–Fisher relation.

The technique was developed by Tully & Fisher (1977), who demonstrated that the global HI profile widths of spiral galaxies show a good correlation with the galaxy’s absolute magnitude. They measured the HI widths of nearby galaxies with already known distances, to be used as calibrators, along with galaxies in the Virgo and Ursa Major clusters. For the nearby galaxies a strong correlation between absolute magni-

tude and global profile width was found. They then added in the data from the Virgo and Ursa Major galaxies, offsetting the apparent magnitudes by a constant amount for each sample so that they were on the same scale as the local galaxies.

The correlation between magnitude and line width lead to the Tully–Fisher distance equation:

$$\mu_0 = 3.5 + 6.25 \log \Delta V(0) + m_{pg}(0) \quad (1.7)$$

where  $\mu_0$  is the distance modulus,  $\Delta V(0)$  is the line width in  $\text{km s}^{-1}$  and  $m_{pg}$  is the apparent photographic magnitude of the galaxy. Their method gave distances to Virgo and Ursa Major as  $\mu_{\text{Vir}} = 30.6$  mag and  $\mu_{\text{UMa}} = 30.5$  mag, consistent with other measurements.

The beauty of the Tully–Fisher relation is that the observables are not themselves distance dependent. However, the results are only as good as the local calibration. The nearby galaxies used Cepheids as calibrators; so once again, even with the farthest distances, the Cepheid calibration is key.

## 1.3 Cepheid Variables

Cepheid variables are young stars of several solar masses, with luminosities of the order of  $10^3$  to  $10^4 L_\odot$ . They are situated in the instability strip of the colour–magnitude diagram, meaning that they are unstable to radial pulsations. Cepheids can enter and leave this area via blue loops several times during their lifetime. The amount of time that a Cepheid spends on the instability strip depends on its mass and composition but all Cepheids appear to take at least an order of magnitude longer to cross the instability strip for the second time than any other crossing (Bono et al., 1999). The position of the instability strip can be seen in Figure 1.2. The points show the colour–magnitude positions of Cepheids from the Large and Small Magellanic clouds (LMC and SMC) and the Milky Way (MW), which trace out the shape of the instability strip (IS). The curves represent the theoretical evolutionary tracks of stars with solar metallicity and masses between  $4M_\odot$  and  $12M_\odot$ . In this figure, the blue loops of low-mass stars do

not overlap with the instability strip, although Cepheids are clearly observed in the SMC at these colour-magnitude positions. This is because the SMC Cepheids have lower metallicity, and therefore have more extended blue loops. The tracks shown in the figure are for *solar* metallicity, corresponding with the blue points in the diagram. This is not to say that the figure is incorrect, but that the differing composition of the three populations shown will affect the position of the instability strip.

### 1.3.1 Cepheid pulsations

Once a Cepheid arrives on the instability strip its mass and luminosity are such that it becomes unstable to radial pulsations. These occur when radiation streams through the star, ionising some of the  $\text{He}^+$  in the star's envelope to  $\text{He}^{2+}$ . This causes the envelope to become more opaque, trapping the radiation that is being emitted. As the radiation can no longer escape the gas heats up, increasing the pressure inside the envelope. The increase in pressure causes the envelope to be pushed out, in turn increasing the size and luminosity of the star. While the star is expanding it begins to cool, which allows the  $\text{He}^{2+}$  to recapture an electron to become  $\text{He}^+$ . The opacity then drops, and the envelope becomes transparent once more, allowing the radiation to escape and lowering the pressure. The envelope contracts once more and the process starts again.

For fundamental mode Cepheids the case is this simple. A single node is situated at the star's centre, and the Cepheid expands and contracts regularly with a single period, as if it is breathing in and out. Fundamental mode pulsations can be described by the period–mean density relation, as described in section 1.3.5 of Hansen et al. (2004).

Firstly, if the sound speed inside the star is taken to be a constant  $v_s$ , the period,  $\Pi$ , of a wave in the star will be defined as

$$\Pi = \frac{2R}{v_s}. \quad (1.8)$$

The sound speed can also be related to the pressure,  $P$ , and density,  $\rho$ , of the material

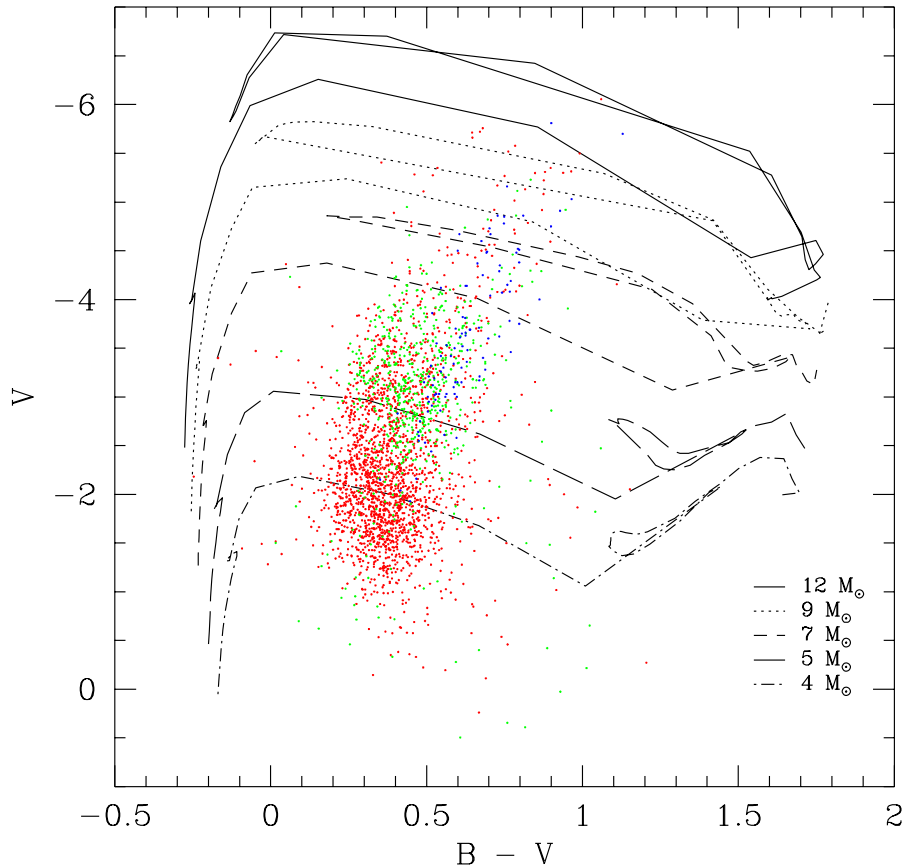


Figure 1.2: Stellar evolution tracks for solar metallicity stars with  $4M_{\odot} < M < 12M_{\odot}$ . Cepheids from the MW (blue), LMC (green) and SMC (red) are over-plotted. The different trends seen for the Cepheid points are believed to be due to the differing metallicities of the host galaxies. Evolution tracks taken from Lejeune & Schaerer (2001), Galactic Cepheid data from Fernie et al. (1995), LMC and SMC Cepheids from OGLE (Udalski et al., 1999a,b).

by

$$v_s^2 = \Gamma_1 \frac{P}{\rho} \quad (1.9)$$

where  $\Gamma_1$ , the first adiabatic component, is approximately 1. This means that, for an ideal monatomic gas,  $v_s$  is proportional to the square root of the temperature.

The next step assumes that hydrostatic equilibrium is approximately maintained throughout the pulsation. This is reasonable, as otherwise if the star deviated from this model too far it would not pulsate; it would overshoot equilibrium and either carry on expanding or contracting. For hydrostatic equilibrium, the virial theorem reduces to

$$-\Omega = \int_M \frac{3P}{\rho} dM_r = \frac{-GM^2}{R}. \quad (1.10)$$

Equation 1.9 can be substituted into the integral term, and the  $M$  and  $R$  terms can be related to density, leaving a relation between period and density:

$$\Pi \approx \frac{1}{(G\langle\rho\rangle)^{1/2}} \approx \frac{0.04}{(\langle\rho\rangle/\langle\rho_{\odot}\rangle)^{1/2}} \text{ days.} \quad (1.11)$$

The period–density relation shown in Equation 1.11 describes very simply the physical source of changes in period. However, it would be more useful if there was a relation between the period and something that could be measured observationally. This is done by expanding the density term into a function of mass and radius.

$$\Pi = \left( \frac{4\pi R^3}{3GM} \right)^{\frac{1}{2}} \quad (1.12)$$

This is not the result that we require; measuring the mass and radius of a star are not simple problems. The derivation must be taken one step further, using the definition of luminosity,

$$L = 4\pi R^2 \sigma T_{eff}^4. \quad (1.13)$$

By replacing the radius terms in Equation 1.12 with a function of luminosity and temperature, and considering the Cepheid population is homogeneous in terms of its mass

distribution, the period–luminosity–temperature relation is found:

$$\Pi \propto \left( \frac{L^{\frac{3}{2}}}{T_{eff}^6} \right)^{\frac{1}{2}}. \quad (1.14)$$

Equation 1.14 is more commonly known as the period–luminosity–colour (PLC) relation, as the temperature of a star defines its colour.

Although the PLC relation is used, the period–luminosity relation is much more commonplace. The PL relation is a projection of the PLC relation onto the period–luminosity plane, which leads to its main down-side. As it is a projection of a three–dimensional function onto a two–dimensional plane, the PL relation is not infinitesimally thin, but has an intrinsic width. This is not a major problem, but it is wise to remember that for a given period, there will be a range of possible luminosities, the scatter in which will depend on the range of temperatures. This is one reason why it is important to use a reasonable number of Cepheids when deriving the PL relation.

## 1.4 The Period–Luminosity Relation

As explained in Section 1.2.2, Cepheids are important distance indicators. Using the period–luminosity relation, the true brightness of a Cepheid can be determined from just its period of pulsation. By combining this with its apparent magnitude, the distance to the Cepheid can be found very easily, using Equation 1.3.

It is now almost a century since the PL relation was first discovered by Leavitt & Pickering. Recently, Cepheid samples of increasing size have been used to find the true value of the slope and zero–point of the relation. Surveys such as the Optical Gravitational Lensing Experiment (OGLE) (Udalski et al., 1992) have observed large areas of the sky, producing catalogues of thousands of Cepheids. It is with these samples that the PL relation can be calibrated to very high accuracy. The detail that these surveys produce, however, leads to new questions about the nature of the relation.

### 1.4.1 The linearity of the PL relation

Up until ten years ago, it was accepted as fact that the slope of the PL relation was universal over the whole period range for fundamental Cepheids<sup>2</sup>. This changed with the publication of a study of SMC Cepheids from EROS (Bauer et al., 1999). The EROS survey is a microlensing experiment, similar to OGLE. They obtained data on 290 and 590 Cepheids in the LMC and SMC respectively. Their intriguing result was that the fundamental PL relation for the SMC appeared to exhibit a slope change at  $P = 2$  days. However, this effect did not appear in their LMC sample, nor in the overtone Cepheids.

Observational effects were ruled out as the cause, as well as several physical possibilities. These included the superposition of different Cepheid populations of different ages, the superposition of a population of Anomalous Cepheids, and a non-uniform filling of the IS due to the blue loops of low mass Cepheids not entering the pulsation region. Each of these causes was ruled out; the metallicity of the SMC is too low for Anomalous Cepheids to be observed, and none of these theories could explain why the slope change wasn't observed in the overtone pulsators.

One suggestion for the cause of the slope change is the topology of the IS. Figure 1.2 shows that lower mass Cepheids are much more abundant in the SMC than those with higher masses. In addition Figure 1.4 (which will be discussed further later), shows that Cepheids with lower masses tend to sit lower down on the colour-magnitude diagram, hence they have shorter periods. It is possible that the high number of low-mass, short-period Cepheids, compared to the number of high-mass, long-period Cepheids, is causing the IS to be filled non-uniformly. Although this effect is not seen in the overtone Cepheids, (Bauer et al., 1999) themselves note that the smaller sample size means that they would be less sensitive to a slope change in the overtone PL relation.

Although the slope change in the SMC sample can now be explained, the problem of a non-linear PL relation has not gone away.

---

<sup>2</sup>There were suggestions that the slope may change gradually with increasing period (Sandage & Tammann, 1968, for example), but in general linear models were assumed.

Using data for 593 Cepheids from OGLE, in addition to 97 long period Cepheids, Sandage et al. (2004) found that the LMC PL relation also exhibited a slope change, this time at  $P = 10$  days. Although a reason for the slope change was not apparent, they noted that several other parameters were also subject to discontinuities at this period. The Fourier coefficients (See Appendix B), which describe the shape of the light curve, were seen to change dramatically, with the direction of the trend in the  $\log P - R_{21}$  plane changing sign, and the  $\log P - \phi_{21}$  trend showing a clear break. Similar discontinuities were seen in the  $\log P$  – Amplitude plane, as well as a break in the ridge line of the IS. The evidence all points to a physical change at  $P = 10$  days, but no theory has been able to predict either the nature of the change, or why it may occur at that period.

The recent OGLE–III data also show a break in the PL relation at 10 days, although many other surveys do not. For example, Fouqué et al. (2007), who re-examine data on Galactic and LMC Cepheids from several sources including OGLE–II find no evidence for a non–linear relation. This is clearly still a problem that must be examined if Cepheids are to be used as the basis of the extragalactic distance scale. Until a consensus is reached on this matter there is a simple way around the problem. By splitting the sample such that it only includes either Cepheids with  $P < 10$  days, or  $P > 10$  days, any effects that may be present will be removed, allowing consistent comparisons to be made between different populations. This is not the ideal solution, as it essentially throws away data, but it does remove the possibility of a slope change affecting the results.

### 1.4.2 The possibility of a metallicity effect

We will assume for now that the PL relation can be considered linear, at least when the sample includes only Cepheids with  $P > 10$  days<sup>3</sup>. This should mean that Cepheid samples from different host galaxies may be used together to create a universal PL

---

<sup>3</sup>The PL can also be considered linear in the  $P < 10$  days regime, but for this example the high  $P$  region is considered.

relation. Alas, this may not be the case. Different galaxies have different properties; an obvious and important example is their chemical composition.

It was explained previously that fundamental mode Cepheids obey the period–density relation, and consequently display a period–luminosity relation. But if the pulsations can be explained by density changes alone, why would a change in composition alter the PL relation if the density of the star remained constant? The answer comes from mechanism driving the pulsations, i.e. the ionisation process.

As described in Section 1.3, the pulsations in Cepheid envelopes arise from the ionisation and recombination of Helium ions. However, metallicity is a measure of the abundance of elements *heavier* than Helium. This would imply that the process would not be affected by the metallicity. This is not the correct assumption; we must consider the star as a whole, rather than thinking of the Helium as a separate entity. The heavier elements in the star will be present in the pulsation region, which will affect its opacity. This also applies to the atmosphere; the changes in opacity caused by the heavy elements will affect both the magnitude and colour of the star.

Opacity is a measure of how much radiation is absorbed by the stellar material. Higher opacities mean that more radiation will be absorbed on its way out of the star, and the star will appear fainter. There are several sources of stellar opacity in Cepheids — electron scattering, free–free, and bound–free absorption.<sup>4</sup> The opacity arising from each of these sources depend on different quantities. Electron scattering depends on the hydrogen mass fraction ( $X$ )

$$\kappa_e = 0.02(1 + X) \text{ m}^2 \text{ kg}^{-1}, \quad (1.15)$$

and free–free absorption includes both the hydrogen and helium ( $Y$ ) mass fractions

$$\kappa_{ff} \approx 4 \times 10^{21}(X + Y)(1 + X)\rho T^{-3.5} \text{ m}^2 \text{ kg}^{-1}. \quad (1.16)$$

---

<sup>4</sup>Bound–bound absorption is also present, but the opacity arising from this in the envelope is around an order of magnitude less than free–free or bound–free absorption. In the atmosphere it does have a significant effect, and will affect the colour of the star, via line blanketing.

Bound–free opacity however, also depends on the metal mass fraction ( $Z$ ), via the relation

$$\kappa_{bf} \approx 4 \times 10^{24} Z(1 + X)\rho T^{-3.5} \text{ m}^2 \text{ kg}^{-1}. \quad (1.17)$$

Using Equations 1.15 to 1.17, the effect of changing  $Z$  can be determined. In the first instance, primordial abundances of  $X = 0.75$ ,  $Y = 0.25$  and  $Z = 0.0$  are assumed, along with a density of  $\rho_\odot$  and  $T_{eff} = 5000\text{K}$ . In this case, the free–free absorption would dominate the opacity at  $1.12 \times 10^{12} \text{ m}^2\text{kg}^{-1}$ , with the  $\kappa_e = 0.035 \text{ m}^2\text{kg}^{-1}$ . At this point the contribution from bound–free absorption is zero, as there are no heavy elements present ( $Z = 0.0$ ).

The next step is to assume that  $Z$  increases by some fraction  $\Delta Z$ , and that  $Y$  also increases, but at a faster rate of  $2.5\Delta Z$ . The value of each opacity, and the total opacity can then be calculated for different metallicities. This is shown in Figure 1.3. It is clear from this figure that once metals are present in the star the dominant source of opacity is  $\kappa_{bf}$ , which increases proportionally with  $\Delta Z$ . As the luminosity of a star will decrease with opacity, it can be assumed that the luminosity is inversely proportional to  $Z$ .

This effect is seen in Figure 1.4. The tracks represent metallicities approximating solar and SMC for  $5M_\odot$  and  $7M_\odot$  stars. The solid black lines represent the edges of the instability strip (Sandage et al., 1999)[table 17], with the dotted lines showing lines of constant period. Both of these assume solar metallicity. Once they evolve off the main sequence, it becomes clear that metallicity is having a significant effect on their appearance. If we assume that metallicity does not affect the lines of constant period, we can see that a more metal–poor star will appear brighter and bluer than the more metal–rich one. However, the constant period lines and the instability strip will both be shifted with metallicity. This means that we must take it into account when measuring Cepheid distances via the PL relation. By neglecting the effect, any Cepheids with  $Z$  not equal to  $Z_\odot$  will be given erroneous absolute magnitudes, and in turn, incorrect distances. This affects more than just the Cepheid distance scale. As Section 1.2 explained, the extragalactic distance ladder uses Cepheids as a base, so any systematic effects that we choose to ignore for Cepheids will be carried through the distance scale

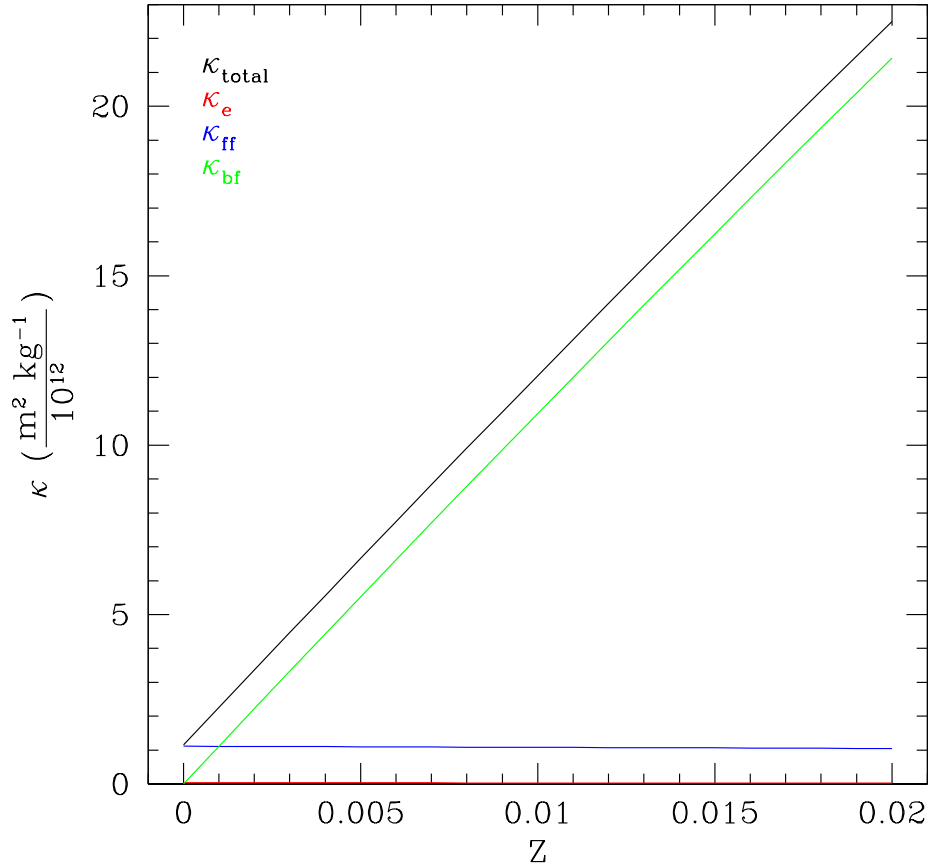


Figure 1.3: Changing contributions to the total opacity from  $\kappa_e$ ,  $\kappa_{ff}$  and  $\kappa_{bf}$  with changes in  $Z$ . The figure assumes  $\rho = \rho_\odot$  and  $T_{eff} = 5000\text{K}$ . At the primordial value ( $Z = 0$ ), the total opacity is dominated by  $\kappa_{ff}$ , but this is quickly overtaken by  $\kappa_{bf}$  as the metal fraction is increased. As the metallicity is increase through the values for the SMC, LMC and MW,  $\kappa_{total}$  increases proportionally with  $\Delta Z$ .

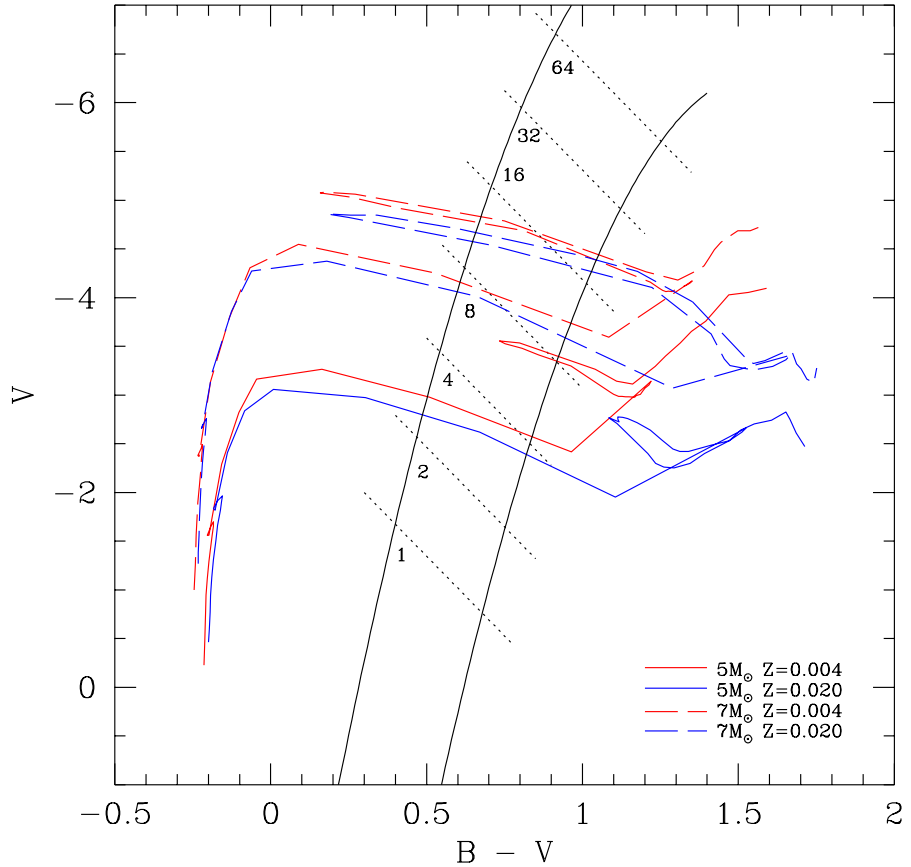


Figure 1.4: Evolution tracks for  $5 M_{\odot}$  and  $7 M_{\odot}$  stars with different metallicities. Blue represents solar metallicity and red represents  $Z = 0.004$ , slightly lower than the SMC. Solid black lines denote the position of the instability strip (Sandage et al., 1999)[table 17]. Lines of constant period are shown with dotted lines labelled with the period in days. Evolution tracks are taken from Lejeune & Schaerer (2001). It is clear from this that both the initial mass and the metallicity of the star will affect its position in the log  $P - Mag$  plane.

as a whole.

### 1.4.3 Theoretical metallicity studies

As explained in the previous section, there is a strong basis for the assumption that distances derived using the Cepheid PL relation should take metallicity into account. It is clear, both from the the differing locations of the Cepheids in Figure 1.2 and evolutionary tracks in Figure 1.4, that metallicity has some bearing on their intrinsic brightness. The question is whether changes in metallicity result in measurable differences in Cepheid magnitudes, and hence their distances.

The earliest work to address the problem was Gascoigne (1974), using the Cepheids in the SMC. This sample, when compared with the galaxy and LMC, was found to contain a greater proportion of short period ( $1 < P < 3$  days) Cepheids, which were also found to be around 0.1 mag bluer in  $(B - V)$ . The hypothesis was that the difference in colour could be explained by the difference in metallicity of the galaxies.

The work of Stothers (1988) addresses exactly this problem. The effect of abundance changes, namely  $Y$  and  $Z$ , on both the colour and absolute magnitude of Cepheids are analysed using theoretical data on stellar evolution, atmospheric models and pulsations. The main conclusion of this work was that the absolute magnitude of a Cepheid *is* dependent on metallicity, in the sense that

$$\delta M_V = 0.5\delta Y - 2.8\delta Z \quad (1.18)$$

where  $\delta Y$  and  $\delta Z$  are both in the sense (solar – observed). Using this result Stothers found that a Cepheid in the SMC (where  $Z = 0.005$ ) will be around 0.04 mag fainter than a Cepheid in the Galaxy if both  $Y$  and the period are fixed. Note that this is the opposite to what is predicted in Figure 1.4, as the constant-period lines for different metallicities are not shown.

This can be extended to the effect on distance moduli. Firstly we assume that a Cepheid with  $Z_\odot$  has absolute magnitude  $M_{V,\odot}$ . A second Cepheid with  $Z_{SMC}$  will have an

Filter	$\frac{dM}{d\log Z}$ mag dex $^{-1}$	$\frac{d\mu}{d\log Z}$ mag dex $^{-1}$
<i>B</i>	+0.02 ± 0.02	-0.02 ± 0.02
<i>V</i>	-0.08 ± 0.02	+0.08 ± 0.02
<i>I</i>	-0.10 ± 0.02	+0.10 ± 0.02

Table 1.1: Summary of results from Sandage et al. (1999) on the effect of metallicity on the absolute magnitudes of Cepheids. The values of  $dM/dZ$  are measured at  $P = 10$  days; the *V* and *I* magnitudes were not found to change at  $P = 31.6$  days, although the effect on *B* is considerably higher at this period ( $dM/dZ = 0.08 \pm 0.02$  mag dex $^{-1}$ ).

absolute magnitude 0.04 mag fainter, i.e.  $M_{V,SMC} = M_{V,\odot} + 0.04$ . If both Cepheids are observed to have the same apparent magnitude, neglecting metallicity, their distance moduli would be found to be the same. However, by including  $\delta M_V$  in the distance equation it is clearly seen that this is not the case:

$$\delta\mu = m - (M_{V,\odot} + \delta M_V). \quad (1.19)$$

This shows that the distance modulus of the second Cepheid is in fact 0.04 mag smaller than that of the first; the second Cepheid is closer. Thinking about it another way, if the second Cepheid appeared 0.04 mag fainter than the first, by including metallicity in the calculation they would be found to be at the same distance.

Since Stothers' work there have been several attempts to theoretically predict the effect using the more sophisticated stellar models that have become available. For example, Sandage et al. (1999) use theoretical evolutionary tracks computed by three independent groups. The pulsation equation, which calculates  $P$  as a function of  $M, L, T_{eff}, Z$  and  $Y$ , is used to calculate the position of the Cepheid instability strip. Using this information they calculate PL relations for Cepheids with a selection of metallicities of  $-1.7 \leq [Fe/H] \leq 0.0$ , allowing  $dM/dZ$  to be evaluated at several wavebands. Although they found that there would be no effect on the bolometric magnitude ( $dM_{bol}/dZ = 0.0$  mag dex $^{-1}$ ), the absolute magnitudes in the Cousins broad-band filters would differ measurably. Their results are summarised in Table 1.1.

Sandage et al. find that, although the bolometric magnitude does not change with metallicity, the broad-band Cousins magnitudes undergo a measurable change. In

$Z$	$\log P$ cut	Low $P$ slope	High $P$ slope	$\Delta$ slope
0.02	0.8	1.36	1.237	-0.123
0.01	0.7	1.46	1.248	-0.212
0.004	0.6	1.47	1.239	-0.231

Table 1.2: Summary of results from Alibert et al. (1999) on the change in PL slope.

the  $B$  band,  $dM/dZ$  is positive, meaning that a Cepheid of lower metallicity will be brighter. Referring back to Figure 1.4, brighter magnitudes are expected with decreasing metallicity, so this is no great surprise. However, as the effective wavelength of the filter is increased, the effect goes the other way;  $dM/dZ$  becomes negative for these wavelengths, and one might expect that the effect would increase as you move towards the infra-red.

Other recent theoretical works, such as Alibert et al. (1999), found no evidence for a change in magnitude with metallicity from the  $V$  to  $K$  bands. They did, however, find that the *slope* of the PL relation would change at low periods, with the period-cut depending on the metallicity of the sample, as summarised in Table 1.2.

From this brief summary, it is evident that there is no consensus on the effect that metallicity has on the PL relation. As with every other astronomical problem, observations are needed as well as theory. The next section summarises past observational works on this problem.

#### 1.4.4 Observational tests for the metallicity effect

The first observational test for a metallicity effect was by Freedman & Madore (1990), who studied the Cepheid population of M31. Taking advantage of its radial metallicity gradient, they observed three radially distinct fields in the  $B, V, R$  and  $I$  bands and obtained distance moduli to each of the fields. By fitting PL relations to the three Cepheid samples they derived distance moduli of each of the fields. After correcting for reddening effects, they found there was no statistically significant difference in the distances, hence no metallicity effect on the distance moduli. However, it is apparent that a metallicity trend is present in the data, but the errorbars on each distance modulus

are such that the results cannot be claimed statistically significant.

Two breakthroughs in the field came in the late 1990s, from two very different sources. The first came from the EROS microlensing survey (Aubourg et al., 1993). This survey was looking for microlensing events in the Magellanic clouds; essentially it was a large set of time-series photometry. Due to the nature of the survey, a large number of Cepheids were detected and measured, and rather than just throw the data out they were analysed. When the LMC Cepheids were compared with those in the SMC, the slope of the PL relation was found to be constant. However, the zero-point (and hence the distance modulus) of the SMC relation was found to be 0.139 mag too faint (Sasselov et al., 1997). Their method had already eliminated reddening from the problem, so this was put down to the metallicity difference, contradicting the result of Freedman & Madore, who stated that there was no metallicity effect.

The second major result came from the Hubble Space Telescope (HST) Key Project. The aim of this study was to measure  $H_0$  to as high a precision as possible by removing systematics that were present in the distance scale. To assess the effect of metallicity, nearby Cepheid host galaxies with small reddening values were observed with HST. In particular, two fields of the nearby spiral galaxy M101 were observed in the  $V$  and  $I$  bands. The test was essentially the same as Freedman & Madore (1990); by observing different regions of an object that are known to be at the same distance, any difference in distance modulus can be attributed to an external effect, i.e. reddening or metallicity. After correcting for reddening, they still found a significant difference in distance modulus, which is parametrised by  $\gamma$ :

$$\gamma = \frac{d(m - M)}{d \log(O/H)}. \quad (1.20)$$

Using the differential method, they found  $\gamma = -0.24 \pm 0.16 \text{ mag dex}^{-1}$ . This is in the same direction as the Sasselov et al. result; lower metallicities will give a higher distance modulus. However, there was still a significant uncertainty on the result, and in the final HST Key Project results they adopted  $\gamma = -0.2 \pm 0.2 \text{ mag dex}^{-1}$  as the metallicity correction (Freedman et al., 2001).

Over the past twenty years the value of  $\gamma$  has ranged from positive values from theoretical calculations, to zero using theoretical and observational data, to negative values from differential tests such as the ones described above. It is clear that there is not currently a consensus; the issue has still not been addressed satisfactorily, and plagues Cepheid distances to this day.

If we truly wish to understand the nature of the Universe as a whole, we must take each and every systematic into account. This work makes no claim to account for every possible source of error, but attempts to improve the extragalactic distance scale by assessing the effect of metallicity on the Cepheid period–luminosity relation.

## 1.5 Overview of the thesis

The aim of this work is to improve the extragalactic distance scale using Cepheids in M33. This is achieved by assessing the effect that metallicity has on Cepheid distances. By calibrating this effect, accurate distances to M33 and other local galaxies can be obtained, hence the accuracy of the distance scale as a whole will be improved. The most obvious question that could be asked at this point is “Why use M33?”. There are many galaxies in our locality that have been observed to house Cepheids, so why chose just one? And if you were to just use a single galaxy, why M33 in particular?

### 1.5.1 Why M33?

Firstly, the question of why only one galaxy. The technique that is used in this work to calculate  $\gamma$  uses differential distances, i.e. the difference in distance moduli rather than their absolute values. Rather than use a selection of galaxies, such as the Magellanic Clouds, and find their relative distances, it makes sense to use a single galaxy and find the distances to different points *within* that galaxy. Using this method, the true distance modulus can be assumed to be the same for all fields, so any differences in distance will be due to metallicity. This is explained in detail in Chapter 3. However, to assume

that all points in the galaxy are at the same distance we must first confirm that they actually are. This brings us to the second question — why choose M33?

M33 is a type Sc spiral galaxy in the local group, with an angular size of  $70.8' \times 41.7'$  (NASA/IPAC Extragalactic Database). M33 is a well studied galaxy, with observations of Cepheids performed by Hubble as early as 1926 (Hubble, 1926). As it is nearby many studies have determined the distance of M33 using different and independent methods, such as eclipsing binaries (Bonanos et al., 2006), the tip of the red giant branch (Kim et al., 2002), and masers (Brunthaler et al., 2005). Although these methods may not provide the same accuracy that a Cepheid distance does, they allow us to have an independent starting point for our analysis of the PL relation of M33.

The galaxy has an inclination angle of  $53^\circ$ . The effect on the Cepheids distances is small enough that they can be assumed to be at the same distance. The metallicity gradient across the galaxy is well defined, so the chemical composition of the Cepheids is relatively easy to determine from their position in the galaxy. These properties inherent to M33 make it the ideal target for a study of this nature.

### 1.5.2 WIYN survey

The following two chapters of (Chapters 2 and 3) describe the methodology and results for the WIYN survey<sup>5</sup>. This survey compared Cepheids in the metal-rich, central region of the galaxy with those in the metal-poor southern spiral arm. Using the reddening-free Wesenheit index (Madore, 1976) PL relations, the distances of each region are obtained. Combining this with the two-component metallicity gradient of Magrini et al. (2007), a value for  $\gamma$  is calculated. In addition, the effects of reddening, crowding, period distribution and PL slope changes are explored.

---

<sup>5</sup>Based on observations obtained with the WIYN 3.5m telescope, Kitt Peak National Observatory, National Optical Astronomy Observatories, which is operated by the Association of Universities for Research in Astronomy, Inc. (AURA) under cooperative agreement with the National Science Foundation. The WIYN Observatory is a joint facility of the University of Wisconsin-Madison, Indiana University, Yale University, and the National Optical Astronomy Observatories.

### 1.5.3 CFHT survey

Chapter 4 takes the work one step further. Rather than using just the central and outer regions of M33, the whole galaxy is observed using CFHT and its one square degree camera, MegaCam<sup>6</sup>. In this study, the galaxy is split into rings of different metallicities, and the PL relations at different radii/metallicities are examined. This study contains around 600 Cepheids, and allows  $\gamma$  to be determined from a consistent set of observations covering a large range of metallicities.

### 1.5.4 Conclusions and Future Work

Chapter 5 summarises the conclusions of the two studies. Chapter 6 discusses the future of the study, and the extensions that will be possible with the addition of infrared observations.

---

<sup>6</sup>Based on observations obtained with MegaPrime/MegaCam, a joint project of CFHT and CEA/DAPNIA, at the Canada-France-Hawaii Telescope (CFHT) which is operated by the National Research Council (NRC) of Canada, the Institut National des Sciences de l'Univers of the Centre National de la Recherche Scientifique of France, and the University of Hawaii.

# **Chapter 2**

## **Photometry Pipeline**

### **2.1 Introduction**

This chapter discusses the photometric procedures adopted to analyse the CCD images of M33 that were used in this project. Photometry is the technique of deriving of magnitudes from an image of an object. Historically, photographic plates were used to record the images, with magnitudes determined visually by ‘human computers’. Photographic plates were ideal when multiple objects were to be observed simultaneously, but the accuracy of the measurements was limited. They also had very low quantum efficiencies (QEs), that is the efficiency with which the detector converted incoming photons into useful output was low. Normal photographic plates had QEs of around 2% (which is surprisingly very similar to the QE of the human eye (Barlow, 1962)), with the specially treated ‘hypersensitised’ plates reaching QEs up to 10% (Howell, 2006, p. 5). In addition to the issues arising from such low QEs, such as low count rates, the plates were intrinsically more sensitive in the blue end of the spectrum so had to be specially treated if the observer wished to detect photons from the redder end of the visual spectrum.

Electronic photometry was to revolutionise the field, allowing robust magnitudes to be obtained by eliminating the cumbersome task of comparing the brightnesses with

nearby stars. An early electronic photometer was a selenium cell devised by Stebbins & Brown (1907). Their technique used the change in resistance of the selenium with temperature to compare the brightness of the moon at different phases with a standard candle. Photomultiplier tubes came next, using the photoelectric effect to measure the intensity of light coming from a single source. They were a great improvement over visual measurements as they have a large range of linearity, allowing the number of photons to be accurately measured. The use of electronic photometers meant that accuracies of milli-magnitudes were finally achievable. However, their main disadvantage over photographic plates was that they could only observe a single source at any time. This problem was overcome by the next advancement in observational astronomy — the charge-coupled device (CCD).

## 2.2 CCDs

The CCD is one of the most significant inventions of the 20<sup>th</sup> century for astronomy, and is credited to Boyle & Wilson (1970). They have progressed from small fields of view to the large-scale giga-pixel arrays that are being developed for telescopes such as Pan-STARRS (e.g., Onaka et al., 2008). The advantages of using CCDs are many, the most significant being their quantum efficiency and linearity. Their use in photometric measurements has transformed the field, allowing measurements accurate to milli-magnitudes whilst still covering large fields of view.

A single CCD chip is made up of many smaller silicon pixels. When the CCD is exposed to light the incident photons excite electrons in the valence band of the silicon, moving them into the conduction band, leaving a ‘hole’ in the valence band. Under normal conditions these electron would recombine with the hole on a very short time-scale. This is stopped by applying a voltage to the pixel, which keeps the freed electron in a potential well. Each pixel has three different voltage ‘gates’ which are kept constant during the exposure. The electrons are confined in the deepest potential well for the duration of exposure. Once it has been completed the voltages of the gates are manipulated in sequence to shift the charge of each pixel along the CCD so that the

total charge can be read out and converted into an integer value by an analogue to digital converter. These values are then stored as a two-dimensional map of the incident photon density — an image of the region that has been observed.

Developments in CCD technology over the past few decades have been immense, leading to fast read-out times with low noise and wide-field cameras capable of viewing vast areas of the sky simultaneously. Without the invention of the CCD the project that is described in this work would not have been possible.

## 2.3 Aperture Photometry

Photometry is a technique which measures the brightness of an astronomical object in an image. In uncrowded fields this is typically done by adding up the number of counts in a circular ‘aperture’ of a given radius centred on the object. The sky signal is estimated using a larger annulus surrounding the object that is free of stars. These values are then converted to a magnitude via the equation

$$m = ZP - 2.5 \log(N - \langle S \rangle) + 2.5 \log dt, \quad (2.1)$$

where  $m$  is the magnitude of the object,  $ZP$  is an arbitrary zero-point constant,  $N$  is the number of counts in the aperture,  $\langle S \rangle$  is the average sky value and  $dt$  is the exposure time in seconds. The magnitude derived from this equation will be purely instrumental; details of how this would be calibrated to a standard photometric system are discussed in Section 3.3.1.

This method is fine for uncrowded fields; both the object aperture and the sky annulus will be free of contaminating stars, meaning that  $dN$  and  $dS$  will be robust measurements. However, as the stellar density increases the distance between neighbouring stars will decrease. The aperture and sky annulus will include other stars and the magnitude measurements will become erroneous. In this situation we must use a different technique, one which considers the shape of an individual stellar profile, which is known as the point spread function.

## 2.4 PSF Photometry

When a star is imaged through a telescope onto a CCD or photographic plate it no longer appears as an infinitesimally small point. Effects such as turbulence in the atmosphere (known as the ‘seeing’) and the optical set-up (the arrangement of lenses, mirrors and detectors) of the telescope cause the point source to be spread out over a finite area in an approximately Gaussian fashion. This shape is known as the point spread function (PSF), examples of which are shown in Figure 2.1. In ground-based, non-adaptive-optics observations the seeing is dominates the shape of the stellar profile, and therefore corresponds to the full-width at half-maximum (FWHM) of the Gaussian profile.

When using the PSF technique the number of counts  $dN$  is no longer the sum of the counts in an aperture, but is essentially the value found by integrating under the PSF function. This is a vast improvement over aperture photometry; provided that all the stars are detected and have accurate positions, the effect of close and overlapping stellar profiles can be removed.

## 2.5 Photometry Software

The data for this project are all digital CCD images, consequently they must be analysed computationally. There are a number of software packages available to perform photometry on such data; for example IRAF<sup>1</sup>, DAOPHOT (Stetson, 1987), DOPHOT (Schechter et al., 1993) and SExtractor (Bertin & Arnouts, 1996). All of these work on the same principle, but have their own advantages and disadvantages. A comparison of recent versions of the programs can be found in Becker et al. (2007). They compare DAOPHOT, DOPHOT, SExtractor and the SDSS photometry pipeline Photo (Lupton et al., 2002), as well as making comparisons between the aperture and PSF

---

<sup>1</sup>IRAF is distributed by the National Optical Astronomy Observatories, which are operated by the Association of Universities for Research in Astronomy, Inc., under cooperative agreement with the National Science Foundation.

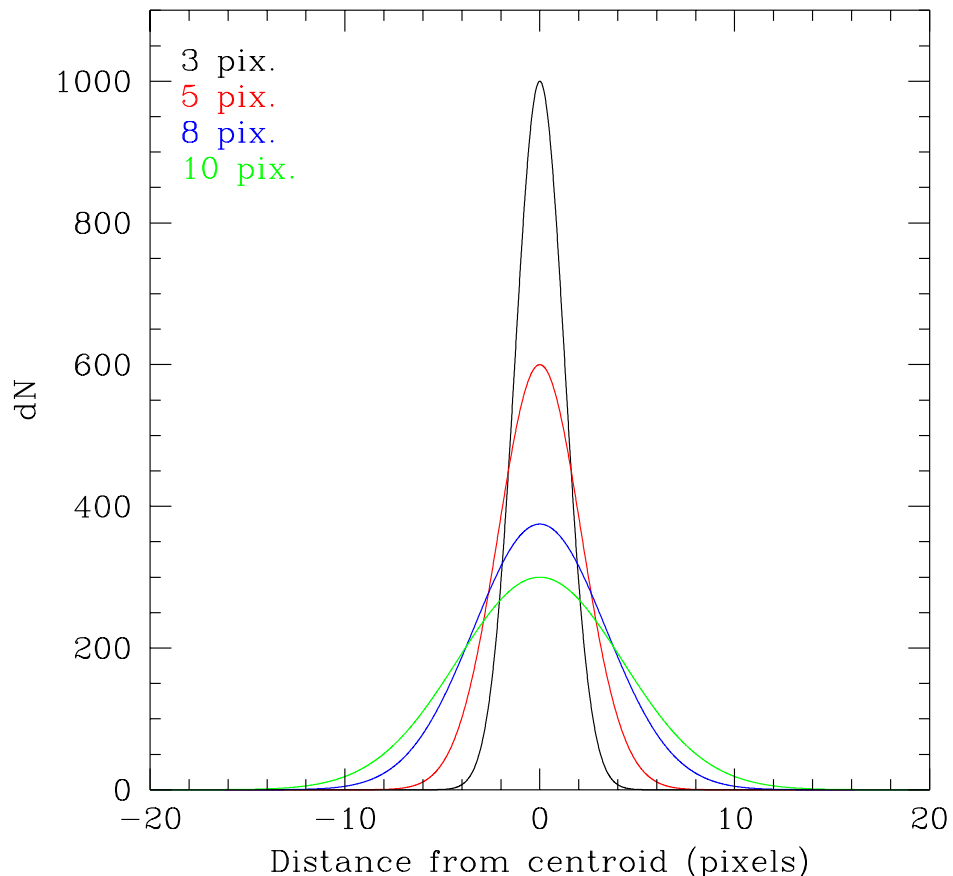


Figure 2.1: Example 1-D Gaussian PSF models for a star observed at different seeing values. The area under the Gaussian stays the same, but as the seeing spreads out the distribution the peak number of counts decreases proportionally to the FWHM.

photometry routines available in the different packages. Their testing shows what is already well known; PSF modelling is essential when dealing with crowded fields. They also found that the DAOPHOT algorithm produces the best photometry in this domain.

For this project, DAOPHOT, along with its companion package ALLFRAME, is used to produce the photometry. It uses an extremely robust algorithm, capable of producing highly accurate results in heavily crowded regions. ALLFRAME is used in addition to DAOPHOT to enable the detection of very faint objects and to bring down the uncertainty on the resulting magnitudes.

## 2.6 Pipeline Development

The pipeline used to process the images was developed using a large data set from the WIYN 3.5m telescope, taken between 1998 and 2001 in the  $B$ ,  $V$  and  $I_C$  filters. Four fields in M33 were observed; two in the centre of the galaxy and two covering the southern spiral arm. A full description of the data set is given in Chapter 3.

The DAOPHOT package was chosen to analyse the data. The standalone version was used, rather than the IRAF version, as the additional packages that are available are essential to this work.

The WIYN data set is extremely large; it contains 25 epochs of four fields in three colours. Due to its vast size it had to be reduced automatically. Processing such a large data set by hand would not only be time consuming, but could also introduce uncertainties due to human error. To remove this possibility, a pipeline was developed that would require minimal human interaction, covering all steps from the star selection to the final PSF photometry.

### 2.6.1 Photometry procedures

The procedures required to obtain PSF magnitudes of the stars on an image are independent of the data in question, and can be summarised as follows:

1. Locate the stars in the image.
2. Obtain a rough aperture magnitude for each star.
3. Select suitable stars for the PSF model and create a model star
4. Fit the PSF model to each star, calculating the magnitude and uncertainty of each one, and subtract each fitted PSF model from the image.
5. Assess the suitability of the model by examining the residuals of the fits on the subtracted image.

The process itself is relatively simple, particularly when performed by hand. However, high levels of crowding and large data sets complicate matters. A flow chart of the pipeline process is shown in Figure 2.2. The pipeline works on each image independently. The images are run through the entire pipeline one by one, with no knowledge of previous images. The steps taken to process a single image using the pipeline are described in the following sections, following the route shown in Figure 2.2.

## 2.6.2 Initial parameters

Before any images can be processed by the pipeline the correct parameters must be input to DAOPHOT. These are shown in Table 2.1. Any parameter not shown was left at its default value. The parameters become important at different steps of the process, and their meanings are explained in the appropriate sections. It is important to note that these values (with the exception of read noise and gain, which were changed for the different CCDs) were kept constant for the entire data set.

## 2.6.3 Star detection

Once the parameters have been set up correctly, the DAOPHOT FIND algorithm makes a first pass of the image to detect the stars. An estimate of the sky brightness is determined from 10,000 pixels uniformly spread over the frame. The high and low tails of

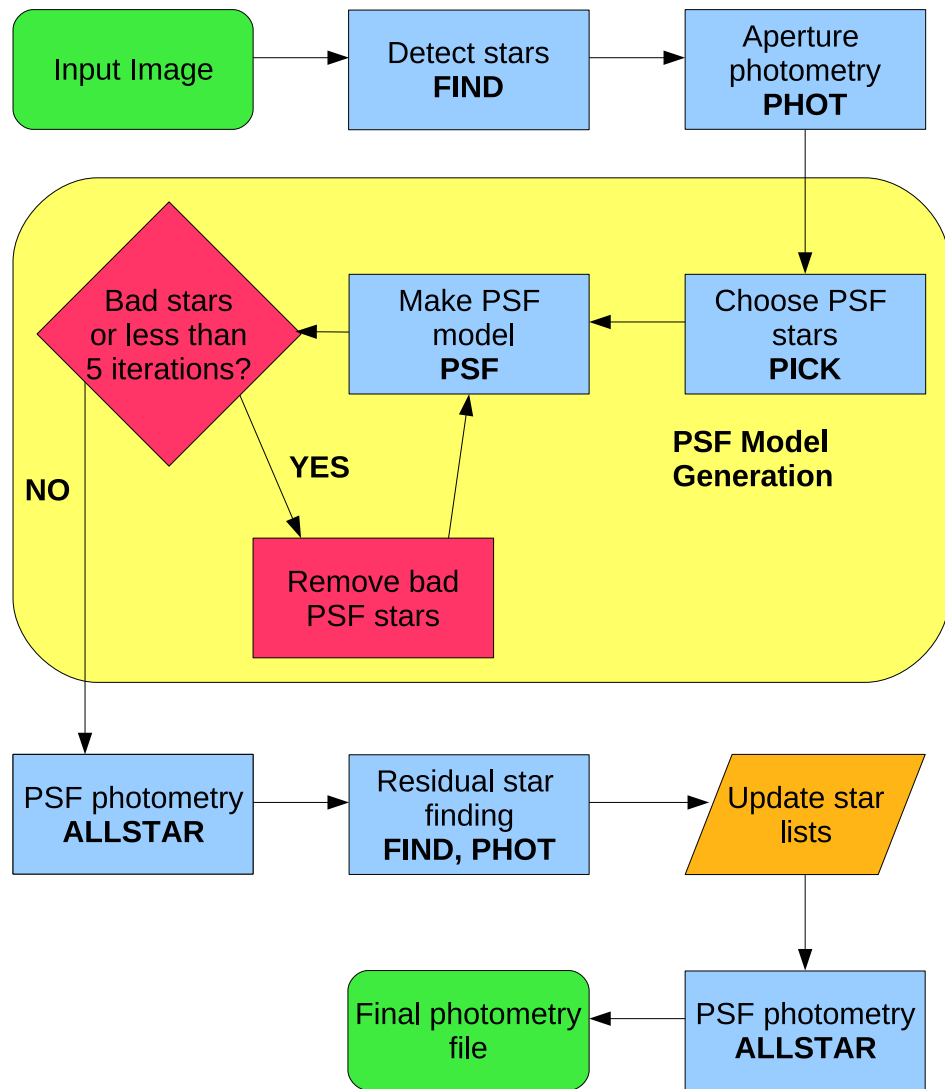


Figure 2.2: Flowchart describing the automated photometry pipeline. Blue boxes denote tasks mainly performed with the DAOPHOT packages, with the package names in capital letters. Pink symbols represent the python scripts used to analyse output files. The orange symbol denotes a book-keeping step which is essential to the pipeline.

Parameter	Value
Read Noise	$8.0 \text{ e}^-$
Gain	$2.8 \text{ e}^- \text{ ADU}^{-1}$
FWHM	4.5 pixels
PSF radius	19 pixels
Fitting radius	4 pixels
High good data threshold	30000 counts
Low good data threshold	$30 \sigma$
Detection threshold	$3 \sigma$
Order of PSF variability	1
Analytic PSF model	-6
Extra PSF cleaning passes	5

Table 2.1: DAOPHOT parameters used in the WIYN pipeline. Any parameters not shown were left at their default value.

the pixel brightness distribution are clipped and the mean and median values are found. The modal value of the sky is then calculated as three times the median minus twice the mean. This value is combined with the read noise and gain parameters in Table 2.1 to calculate the value of  $\sigma$ . Once  $\sigma$  has been obtained it is combined with the threshold parameters to find the number of counts corresponding to the low good data threshold and the detection limit.

The image is then convolved with a Gaussian with the given FWHM and searched for local brightness enhancements whose peaks exceed the detection threshold. The suitability of candidate objects is assessed by the sharp and round parameters.

The sharp value is calculated by fitting a Gaussian and a delta function to the brightness enhancement and examining their ratio:

$$\text{sharp} = \frac{\text{height of best fitting delta function}}{\text{height of best fitting Gaussian function}} \quad (2.2)$$

If the enhancement is due to a bright artifact such as a cosmic ray the height of the delta function will be large whilst the height of the Gaussian will be low, leading to

large sharp values. Conversely, if the local brightness enhancement is due to a nearby cold pixel the height of the delta function will tend to zero and the Gaussian height will be small, bringing sharp towards zero. The acceptance range for sharp was kept at its default value of  $0.2 \leq \text{sharp} \leq 1$  as these are typically the best values for stellar profiles.

Once a candidate passes the sharp criteria two one-dimensional Gaussians are fitted to the brightness enhancement; one each in of the x and y directions. This allows the roundness of the profile to be assessed. Round is defined as

$$\text{round} = \frac{\text{height of } y \text{ Gaussian} - \text{height of } x \text{ Gaussian}}{\text{average of the two heights}} \quad (2.3)$$

where the limits of acceptance were again left at their default values of  $-1 \leq \text{round} \leq 1$ . This test will remove extended objects such as galaxies. However, it is only capable of excluding objects that are extended in either the x or y directions and will not flag objects where the axis of elongation is at a significant angle to the axes. All objects that pass both the sharp and round tests are added to the star list to be processed by the rest of the pipeline.

It is interesting to note that although the frames were taken under different conditions, and hence the FWHM differed between frames, the most appropriate solution found was to use a single, relatively large FWHM for all the frames. By using a FWHM larger than the true value all the stars were detected without the need for the time consuming task of recalculating a new value for each frame. A subset of images taken in various conditions was used to test whether a single value would be appropriate and it was found to produce just as good results in a significantly shorter time.

#### 2.6.4 First pass photometry

Initial estimates of the magnitudes of each star detected by FIND are obtained using the aperture photometry routine PHOT. Although the fields are crowded and aperture photometry will not provide reliable results for the majority of objects, rough magnitudes

Parameter	Value
Aperture 1	11 pixels
Inner sky	19 pixels
Outer sky	23 pixels

Table 2.2: PHOT parameters used for aperture photometry in WIYN pipeline

are required before PSF star selection can take place. The parameters used in PHOT are shown in Table 2.2. Magnitudes are calculated using the equation

$$M = 25 - 2.5 \log(N_* - N_S n_{pix}) \quad (2.4)$$

where  $M$  is the magnitude,  $N_*$  is the number of counts in the aperture,  $N_S$  is the average sky value, estimated this time using the modal value of the pixels in the sky annulus and  $n_{pix}$  is the number of pixels in the aperture. The signal-to-noise ratio is used to calculate the error on each magnitude via the equation

$$\sigma_{mag} = \frac{1.0857 \sqrt{N_* + (1 + n_{pix}/n_B)(N_S + N_R^2 + G^2 \sigma_f^2)}}{N_*}, \quad (2.5)$$

where  $n_B$  is the number of pixels in the sky apertures,  $N_R$  is the read noise,  $G$  is the gain and  $\sigma_f$  is an estimate of the  $1\sigma$  error introduced in the analogue-to-digital converter. The 1.0857 term arises from the conversion between flux and magnitudes (Howell, 1993). In the high signal limit Equation 2.5 reduces to

$$\sigma_{mag} = \frac{1.0857 \sqrt{N_*}}{N_*} \quad (2.6)$$

as Poisson noise will dominate the uncertainty.

### 2.6.5 PSF modelling

Creating an accurate model of the point spread function is the most important step in the pipeline. To achieve the best photometry possible the model must be representative

of all stars in the frame and extreme care must be taken in its creation. When dealing with a small number of images the PSF star selection can be done by hand to ensure that the best stars are chosen, but when vast data sets such as the one in this project are being analysed it would be unwise to attempt such a task by hand.

The process of selecting suitable PSF stars and creating the model is summarised in the yellow area of Figure 2.2. The main steps in the process are as follows:

1. The PICK algorithm selects 200 bright, isolated stars with instrumental magnitudes brighter than 17 as the initial candidate list.
2. The PSF routine creates six models using the different Gaussian, Moffat and Lorentzian functions available, selecting the most suitable by analysing the fitting residuals. This creates a log file showing the differences between the best fit model and each PSF star.
3. A python script analyses the log file, removing any stars from the PICK list which have fitting residuals greater than twice the root-mean-squared value for the ensemble or are labelled as saturated or defective.
4. The updated star list is fed back into PSF and steps 2 and 3 are repeated until no bad stars remain or the process has been completed five times, whichever is the latter.

As mentioned in point 2, there are six PSF models available to DAOPHOT; shown below are the  $x$  components of each function.

$$\text{Gaussian : } f(x) = \alpha e^{\frac{-(x-x_0)^2}{2\delta^2}} \\ FWHM = \delta 2\sqrt{2 \ln 2} \quad (2.7)$$

$$\text{Moffat : } f(x) = \frac{\alpha(\beta-1)}{\pi\delta^2} \left[ 1 + \frac{x-x_0}{\delta} \right]^{-\beta} \\ FWHM = \delta 2\sqrt{2^{\frac{1}{\beta}} - 1} \quad (2.8)$$

$$\text{Lorentz : } f(x) = \frac{\alpha}{\pi} \left[ \frac{\delta}{(x-x_0)^2 + \delta^2} \right] \\ FWHM = 2\delta \quad (2.9)$$

$$\text{Penny : } f(x) = \alpha \left( e^{\frac{-(x-x_0)^2}{2\delta^2}} + \frac{1}{\pi} \left[ \frac{\gamma}{(x-x_0)^2 + \gamma^2} \right] \right) \\ FWHM = \delta 2\sqrt{2 \ln 2} = 2\gamma \quad (2.10)$$

Profiles of these models are shown in Figure 2.3. The Moffat and Penny functions both have two versions available; The  $\beta$  parameter in the Moffat function can be either 1.5 or 2.5, whilst the Lorentz component of the Penny function can either be fixed or allowed to be tilted relative to the Gaussian component. In each case, the parameters  $\alpha$  is used to calculate the intensity of the profile. The values of  $\delta$  and  $\gamma$  can be derived from the FWHM that is given in the parameter file and  $\beta$  has a fixed value depending on the model. In the case of ALLSTAR, the  $x_0$  values (also  $y_0$  when we extend the above functions to two dimensions) are recalculated from their initial FIND values. However, in ALLFRAME  $x_0$  and  $y_0$  are left fixed. This point is discussed further in Section 2.7.

The method produced a well-fitting PSF model and look-up table for each frame. The PSF model is the analytical function (e.g. Gaussian, Moffat, etc.) and the look up table contains the deviations of the averaged PSF star and the analytical function. Increasing the number of iterations and the order of variability of the model were both tested but were not found to significantly improve the result. The distributions of the number of PSF stars according to field and filter are shown in Figures 2.4 and 2.5.

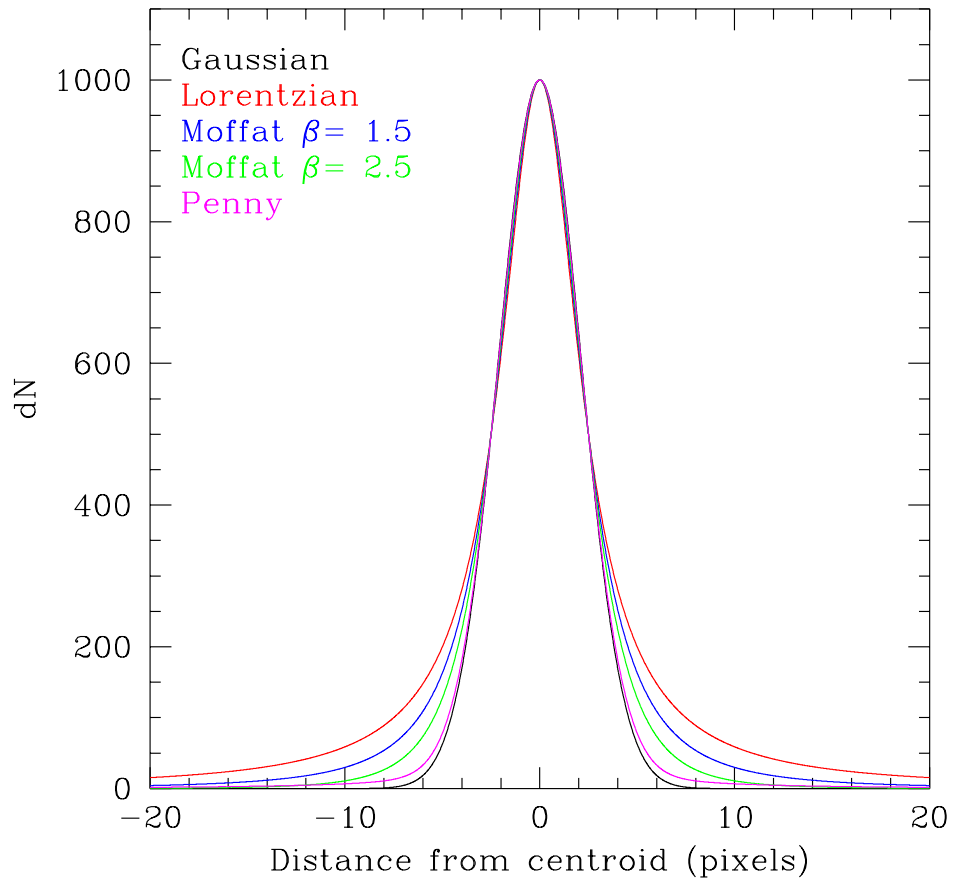


Figure 2.3: Examples of the different PSF models available in DAOPHOT. The models are almost identical in the core of the PSF, but differ noticeably in the wings. It is important to be able to model the outer regions as accurately as the inner regions so that systematics will not be introduced into the photometry.

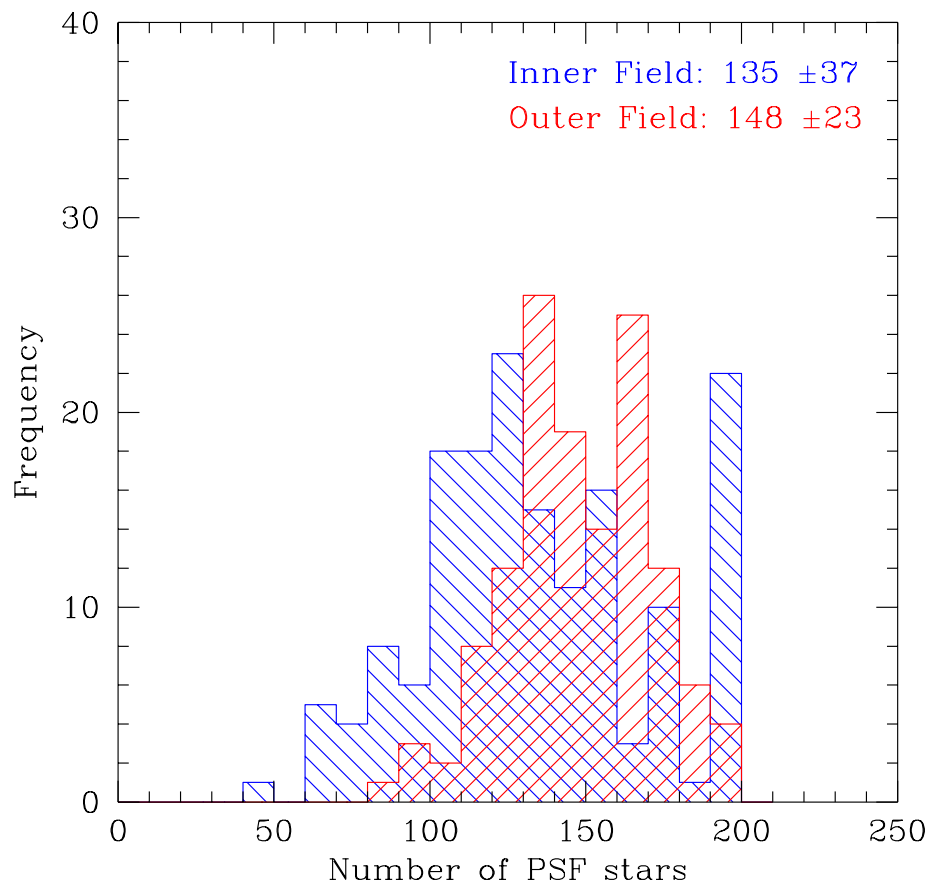


Figure 2.4: Histogram of number of stars in final PSF list in the inner and outer fields. The inner field has a lower average number of stars but a higher dispersion than the outer field.

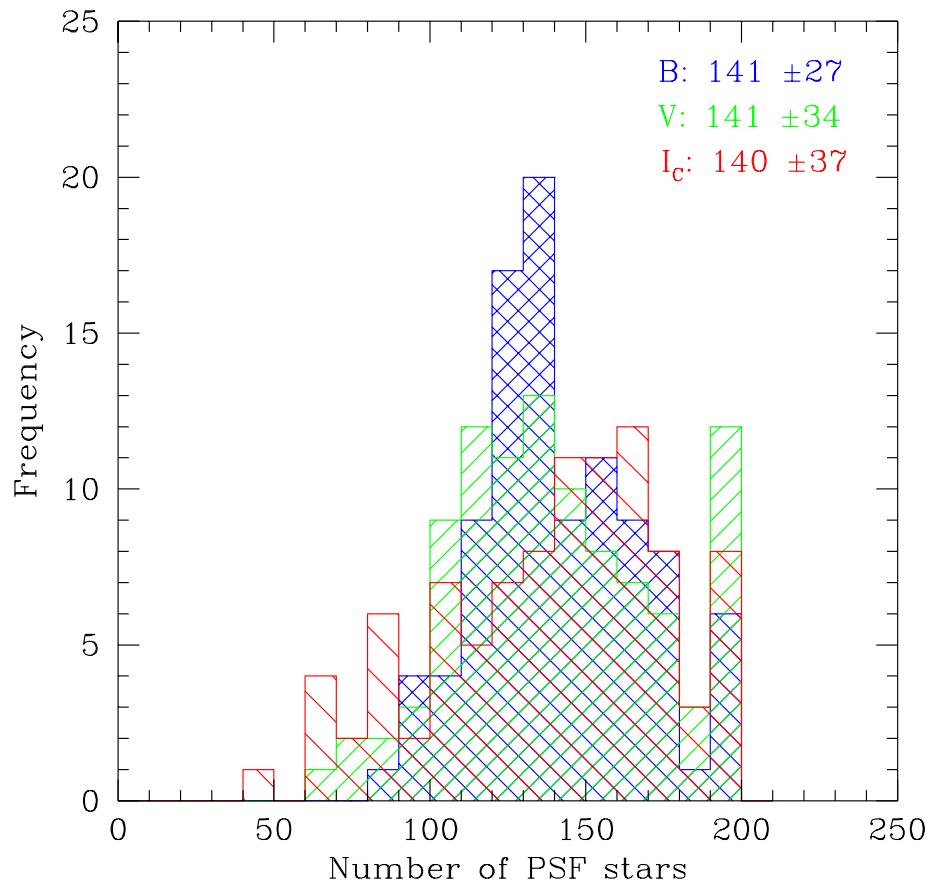


Figure 2.5: Histogram of number of stars in final PSF list in each filter. The average number of stars chosen can be seen to be independent of filter, although the dispersion increases with wavelength.

Figure 2.4 shows that the mean number of PSF stars selected in the inner field images is slightly lower than in the outer field. This is because the inner region is much more crowded, and so more stars will be affected by nearby objects, hence will be rejected. Although it may seem counter-intuitive, this is also the reason behind the slightly higher number of inner field frames with 200 PSF stars. In frames with poorer seeing, the stellar profiles will overlap more as the FWHM increases. The degree of overlap is increased for the inner field because of the high level of crowding. In these images the average fitting residual was quite high, so no stars were flagged up as bad. However, this was not found to affect the photometry in a significant way.

It is clear from Figure 2.5 that the number of PSF stars is independent of the filter. The mean number of PSF stars does not change between filters, but the dispersion of the distribution increases with wavelength. This is similar to the effect seen in Fig. 2.4. For a given set of observing conditions,  $I_C$  frames will have better seeing (i.e. smaller FWHM) and a larger number of stars than the  $V$  and  $B$  frames. This affects the distribution in two ways, worse seeing will increase the fitting residuals and allow more PSF stars to be chosen, better seeing will generally give a better PSF model as the effects of crowding will be lessened, but this will push the average fitting residual down, meaning that a star is more likely to be rejected. However, these effects only affect the *dispersion* of the number distribution, not the quality of the PSF model itself, as large numbers of stars are still used.

## 2.6.6 ALLSTAR photometry

Once a suitable PSF model has been made the image is then passed to ALLSTAR for the first pass PSF photometry. ALLSTAR fits the PSF model to every star in the image simultaneously, determining improved values for their positions and magnitudes. Each fitted model is subtracted from the image and the residuals analysed. Once a star's position and magnitude has converged the star is subtracted from the image permanently. This process generally takes ten iterations to complete and provides good PSF magnitudes, and an image with all the converged stars subtracted. The parameters used

Parameter	Value
Fitting radius	4 pixels
Inner sky radius	19 pixels
Outer sky radius	23 pixels

Table 2.3: WIYN ALLSTAR parameters. Any not shown were left at their default values.

are shown in Table 2.3. The fitting radius is the distance from the centroid position to which the PSF model is fit. This was intentionally kept small as to minimise the contamination from nearby objects. The sky values were estimated from the annulus from 19 to 23 pixels.

The subtracted image produced by ALLSTAR was run through the FIND and PHOT tasks again so that any stars that were too faint or crowded in the first pass could be identified. The new faint-star list was appended to the original list and this was run through ALLSTAR again to get an initial PSF magnitude for every star in the field.

### 2.6.7 Automation

All the data reduction steps up to this point are completed by the automated pipeline. The individual processes are controlled by a series of C shell scripts, with the book-keeping steps in the PSF creation handled by Python routines. The final ALLFRAME processing was completed by hand, as visual inspection of the output images was required at each step to ensure the most accurate results.

## 2.7 ALLFRAME

Although ALLSTAR provides reasonable magnitudes, it is possible to reduce the uncertainties using ALLFRAME (Stetson, 1990). This algorithm works in a similar way to ALLSTAR, but uses fixed values for the centroid positions. By fixing the  $x$  and  $y$  coordinates in each fit, the number of free parameters is reduced, thus reducing the error on the final magnitude.

Algorithm	Free Parameters	Observables per variable
ALLSTAR	$7.5 \times 10^6$	16.67
ALLFRAME — No updates	$2.6 \times 10^6$	48.08
ALLFRAME — Updates	$2.6003 \times 10^6$	48.02

Table 2.4: Comparison of the number of free parameters to be fitted for a sample of 50 frames each with 50,000 stars. Assuming a fitting radius of 4 pixels, each star is fitted using  $4^2\pi$  pixels, leading to  $1.25 \times 10^8$  observables for the entire set. Both ALLFRAME methods have almost three times as many observables as free parameters compared to ALLSTAR, resulting in improved uncertainties on the final magnitudes.

Comparing the number of free parameters in each fit in ALLSTAR and ALLFRAME shows how the improvements in uncertainty are achieved. In ALLSTAR the coordinates and magnitude of each star are fitted, leading to  $3Nn$  free parameters for a set of  $N$  stars in  $n$  frames. In contrast, ALLFRAME uses a fixed set of coordinates, reducing the number of free parameters to  $N(n + 2)$ . It is also possible to allow ALLFRAME to improve the transformation equations that are used for each frame (which are shown in Equations 2.11 and 2.12). This will increase the number of free parameters to be fitted to  $N(n + 2) + 6n$ . Table 2.4 illustrates this for a set of 50 images, each containing 50,000 stars using a fitting radius of 4 pixels; values which are comparable to the WIYN data set.

Before ALLFRAME can be run a single reference frame must be created using DAOMATCH, DAOMASTER and MONTAGE2 (all kindly provided by P. Stetson). DAOMATCH uses the brightest 30 stars in each ALLSTAR output file to create an initial transformation for each frame, shifting each image to the reference image. In the case of the WIYN data, the highest-quality  $V$  band frames of each observed region were chosen to be the reference. The transformations are then fed into DAOMASTER, which calculates a six order transformation using all the stars in each photometry file. The DAOMASTER transformations take the form:

$$x(1) = A + C \times x(n) + E \times y(n) \quad (2.11)$$

$$y(1) = B + D \times x(n) + F \times y(n) \quad (2.12)$$

Where '1' denotes the reference coordinate system and  $n$  represents the frame being

transformed. The transformation information is fed into MONTAGE2, along with the PSF model for each image, to create a medianed image of the field. The program takes into account the different PSF models, seeing and average sky values of each frame to ensure a clean, and statistically correct, final image.

A medianed image is used for the reference frame for two reasons. Firstly, medianing is the most effective way of removing cosmic rays that could otherwise make their way into the reference list as false detections. Secondly, the signal to noise of the image is improved. For a single image the error in a single pixel is defined as

$$\sigma_1 = \sqrt{\frac{\text{sky}}{\text{gain}} + \text{readnoise}^2} \quad (2.13)$$

where the sky and readnoise are both in ADU, and gain is in  $\text{e}^{-}\text{ADU}^{-1}$ . When  $N$  frames are averaged the effective gain increases by a factor of  $N$  as the signal is boosted. The readnoise terms for each frames are added in quadrature, resulting in an effective readnoise which is a factor of  $\sqrt{N}$  lower than for a single frame. This leads to a reduced value for the single pixel error:

$$\sigma_N = \sqrt{\frac{\text{sky}}{N \times \text{gain}} + \left(\frac{\text{readnoise}}{\sqrt{N}}\right)^2} = \frac{\sigma_1}{\sqrt{N}} \quad (2.14)$$

meaning that the number of counts constituting a statistically significant detection is reduced by  $\sqrt{N}$ . In this case median values are used rather than the mean. The effect of this on the signal to noise ratio can be found by examining the efficiency of the median; that is the ratio of the variances of the mean and median:

$$\frac{\sigma_{\text{mean}}^2}{\sigma_{\text{median}}^2} = \frac{2N - 2}{\pi N} \quad (2.15)$$

which is shown in Figure 2.6

If we set  $N = 5$  in Equation 2.14 it can be seen that the detection threshold is approximately half that of a single image. This is ideal for ALLFRAME; as the positions of the stars on the individual frames are fixed, it is possible to fit the PSF to very faint stars

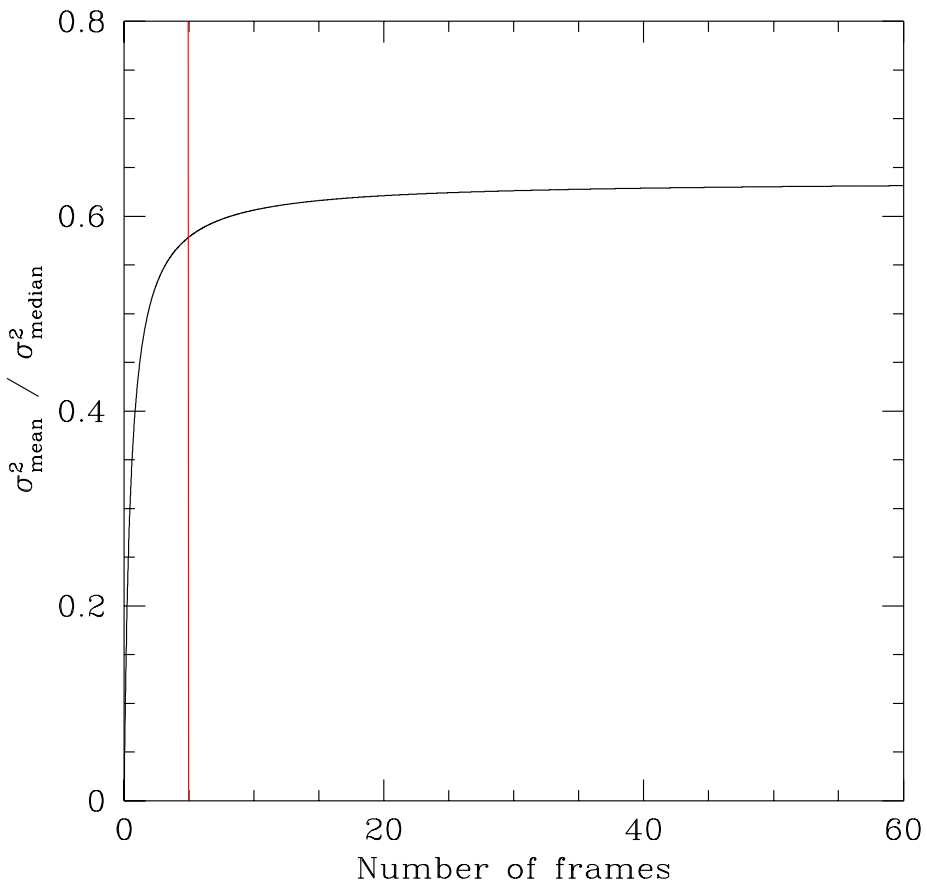


Figure 2.6: Efficiency of the median for  $0 \leq N \leq 60$  frame stacks. The asymptotic efficiency (Stuart & Ord, 1991)[p. 950] of the median is found to be  $2/\pi$ . This value is quickly approached, even with a relatively low number of frames.

without compromising the accuracy of the results.

Although the median may seem a poor choice compared to the mean in terms of the signal-to-noise ratio achievable, it is more effective at removing cosmic rays and other bad pixels. This is a crucial step as any high bad pixels that are falsely recorded as stars in the master image will be passed through the ALLFRAME reduction process and attempts will be made to fit them in the individual frames.

The medianed image is put through the same pipeline as the individual images, but with the detection threshold set to take into account the improved signal to noise ratio. The final star list is offset in  $x$  and  $y$  to take into account the shift between the medianed frame and the reference image. In the case of the WIYN data, two reference frames were made, one for each region observed. The individual fields in the each region overlap; this fact was taken advantage of to create a consistent reference frame and star list for each region. This made it much simpler to put all the frames on the same zero-point.

The reference star list is fed into ALLFRAME, along with the single image PSF models, photometry files and images. Each star in the reference list is fit in all the frames. The most important problem solved by this process is that of matching detections in separate images. For example, in a frame with good seeing two close neighbours may be detected as such, but in a frame with poorer seeing the profiles will overlap and the two objects will be detected as a single star. By using a deep master list this problem is removed — if a close pair is seen as two stars on the reference frame then they will be fitted as two separate objects on *every* frame.

Another important feature of ALLFRAME is that an object is no longer automatically discarded if it does not meet the detection threshold in a frame. Although this may sound counterintuitive, consider the case of a faint star with  $(B - V) < 0$ . If all the frames were to be treated independently, the star may be detected in the  $B$  frame at the  $3\sigma$  level, but may just fall short of the  $V$  detection level at  $2.9\sigma$ . In this case there would be no recorded detection in  $V$  and it would not be possible to calculate the colour of the star. With ALLFRAME, the presence of the star in the reference list proves it to be

a true detection and the star will be measured.

The output from ALLFRAME consists of a photometry file and subtracted image for each frame. This is the final step of the instrumental PSF photometry process.

## 2.8 Calibration Steps

To complete the photometry process the instrumental magnitudes from ALLFRAME must be converted to a standard system; a process which itself requires several steps. The aperture and zero-point corrections were both automated, again using C shell scripts. The task of transforming the photometry on to a standard system was performed by hand.

### 2.8.1 Aperture Corrections

Aperture corrections are essential when calibrating to a standard photometric system. The science frames in this project were analysed using PSF photometry as they are crowded. However, the images of the Landolt fields that are used to derive the photometric transformation use aperture photometry. In principle, these two methods would be compatible if the science frames were uncrowded; a large fitting radius could be used to calculate the PSF magnitudes and the flux from the wings of the stellar profile would be included in the calculation. In crowded fields this is not practical; the fitting radius is typically much smaller than the aperture that is used to measure the standard stars, hence the derived PSF magnitudes will be systematically offset from the true values.

To remove this effect a correction factor must be applied. The aperture correction is calculated by measuring a number of stars across the frame in a series of apertures with increasing radii. The aperture sizes are listed in Table 2.5. The correction must be calculated from stars which are isolated to remove the possibility of contamination from nearby stars in the larger apertures. This makes the stars used to make the PSF

Aperture	Radius (pixels)
A1	4
A2	6
A3	8
A4	10
A5	12
A6	14
A7	16
A8	18
A9	20
Inner sky	25
Outer sky	30

Table 2.5: Aperture and sky annulus sizes used in the curve of growth analysis

model ideal for this task. Images were prepared for the analysis by subtracting all stars *except* the PSF stars from the image. This subtracted image was then run through PHOT using the parameters shown in Table 2.5. The smallest aperture size was chosen to correspond to the PSF fitting radius, with the largest aperture and the sky annulus matching the values used in the analysis of the Landolt fields (which is discussed in Section 3.3.1).

The results from the multi-aperture photometry are processed by DAOGROW (Stetson, 1990). This produces growth curves showing how the amount of flux recorded changes with aperture size. Example growth curves are shown in Figure 2.7.

The individual aperture correction for each star is defined as the magnitude in the largest aperture minus the PSF magnitude. The average value for the frame is then found by iteratively removing the furthest outliers from the sample until the result converges. The WIYN data set contains images taken using two different cameras, the Imager which is a single CCD and the MiniMosaic which is made of two larger CCDs. To ensure consistent photometry, aperture corrections were calculated for a reference frame for each field, filter and CCD combination, i.e. 12 corrections for the Imager and 24 for the MiniMosaic. The correction was subtracted from the original magnitude to account for the flux missed by the PSF fit.

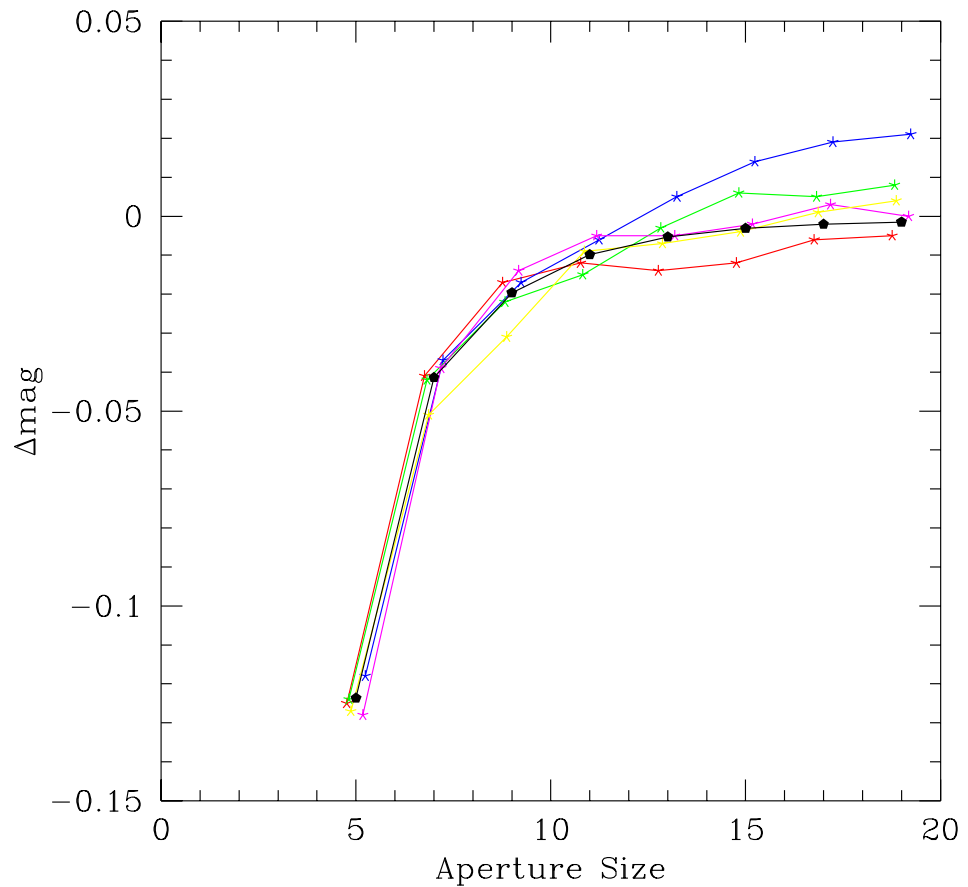


Figure 2.7: Example individual growth curves for five stars are shown in colour. The final growth curve derived from 113 stars is shown in black. It is clear that the 20 pixel aperture size is appropriate for the standards and aperture correction.

## 2.8.2 Zero Points

Before the final standard calibration the frames from different nights must be set to the same zero-point as the reference night. The zero-point difference was found by calculating the average difference between a selection of stars appearing in the reference and the frame in question. A lower instrumental magnitude limit of 13 was imposed to ensure that the average was not affected by the faintest end of the distribution.

DAOMASTER was used to find stars that appeared in both frames, producing a ‘raw’ magnitude file, showing the two magnitudes for each matched star. A list of  $\Delta\text{mag}$  for each star was produced and was sorted numerically. The average offset and its dispersion were calculated, with the star with the largest deviation removed from the list repeatedly until the dispersion on the offset was less than 0.01 mag. This proved to be a robust method of calculating the zero-point offset, typically using 1000 to 2000 stars and distinguishing offsets down to one-hundredth of a magnitude.

# Chapter 3

## WIYN survey of M33

### 3.1 Introduction

This chapter describes the analysis of the WIYN survey of M33, in which two regions of the galaxy were observed with the intention of assessing the effect of metallicity on the zero-point of the Cepheid period–luminosity relation.

As described in Chapter 1, the effect of chemical composition on Cepheid magnitudes and colours is one of the few remaining uncertainties in the local distance scale. If this problem was just confined to the stars themselves it could be considered less of an issue. However, Cepheids are used as the bottom rung of the extragalactic distance ladder, and as a consequence any systematic errors introduced at this level would not be self-contained; they would have implications for astronomical distance measurements from within our own galaxy to the very furthest objects.

This work uses a multi-epoch survey of M33 conducted with the WIYN 3.5-m telescope. M33 is a well studied galaxy, with observations of Cepheids performed by Hubble as early as 1926 (Hubble, 1926). As it is nearby, many studies have determined the distance of M33 using different and independent methods, such as eclipsing binaries (Bonanos et al., 2006), the tip of the red giant branch (TRGB) (Brooks et al., 2004; Galleti et al., 2004; McConnachie et al., 2004), masers (Brunthaler et al., 2005)

and Cepheids themselves (Freedman et al., 1991). Although some of these methods may not provide the same accuracy that a Cepheid distance does, they allow us to have an independent starting point for our analysis of the PL relation in M33.

In this study we examine the effect of metallicity on the Cepheid PL relation by observing two regions of the galaxy with differing compositions; the central, metal-rich region is compared with the metal-poor southern spiral arm. By comparing two areas with such disparate metallicity values that are known to be at the same distance, the effect of changing metallicity on the observed Cepheid distance modulus can be explored.

## 3.2 Observations

The data set consists of 25 epochs of  $BVI_C$  images of two regions of M33 obtained between 1998 and 2001 on the WIYN telescope. Four fields were observed for the survey, two in the centre of M33, and two in the outer, southern part of the galaxy. The locations of the fields are shown in Figure 3.1<sup>1</sup>. The J2000.0 coordinates of the fields are shown in Table 3.1. The first 20 epochs used the WIYN s2kb Imager, a single thinned Tek/STIS 2048x2048 CCD with 21  $\mu\text{m}$  pixels. For the final 5 epochs the new Mini-Mosaic (MiMo) camera was used. The Mini-Mosaic consists of two thinned SITe 2048x4096 CCDs with 15  $\mu\text{m}$  pixels. A single exposure covered  $6.8 \times 6.8$  arcmin for the Imager, and  $9.6 \times 9.6$  arcmin for the Mini-Mosaic, with pixel scales of 0.195 and 0.141 arcsec pixel<sup>-1</sup> respectively.

All the fields were observed in the  $B$ ,  $V$  and  $I_C$  filters with both cameras. The positions of the fields were chosen such that the metal-rich population at the centre of the galaxy could be compared with the more metal-poor population in the outer region. Cepheids tend to be concentrated in the spiral arms, so the outer fields were located in the part of the galaxy which coincided with the clearest arm. The addition of the Mini-Mosaic

---

<sup>1</sup>Original image copyright: National Optical Astronomy Observatory/Association of Universities for Research in Astronomy/National Science Foundation

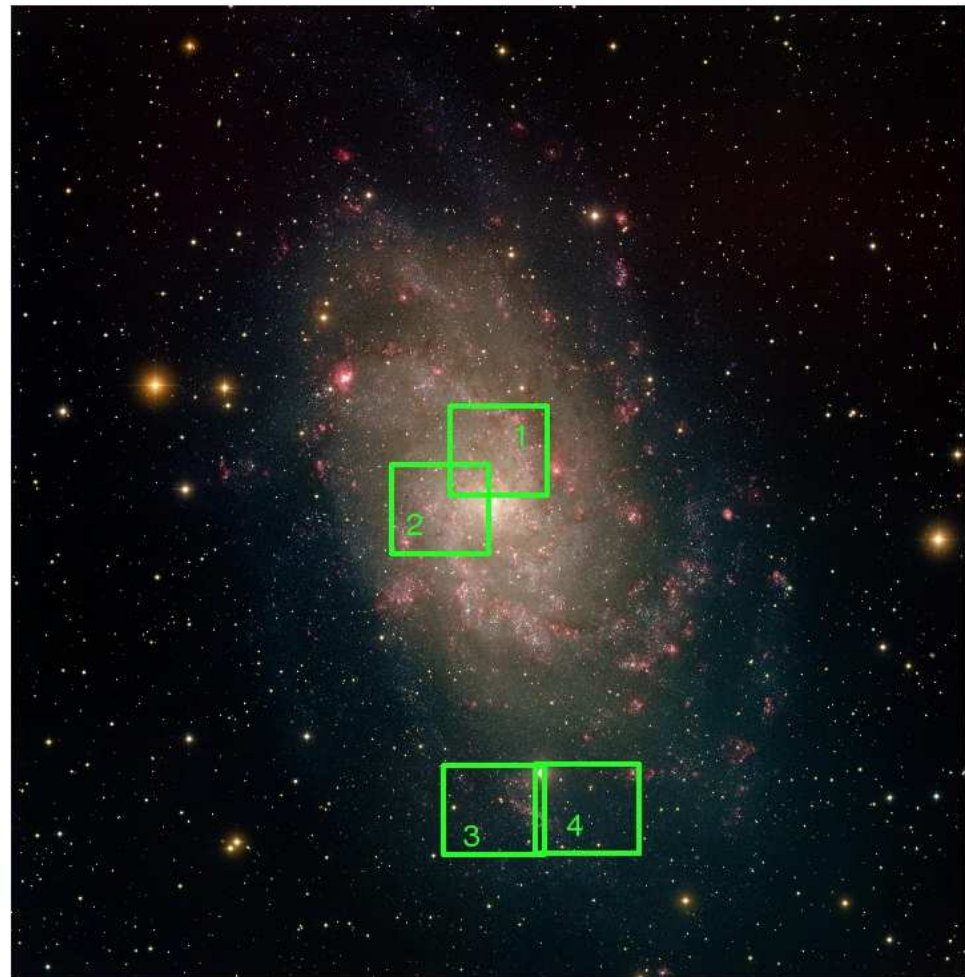


Figure 3.1: The two regions observed for this survey. The inner region contains fields 1 and 2; the outer region contains fields 3 and 4. The fields were chosen such that they would cover the whole metallicity range of the galaxy. Orientation: North up, East left.

Field	$\alpha$	$\delta$	Angular	Linear
<b>Imager</b>				
M33-1	1 <sup>h</sup> 33 <sup>m</sup> 49.12 <sup>s</sup>	30°42'56.48"	217.64"	0.886 kpc
M33-2	1 <sup>h</sup> 34 <sup>m</sup> 06.13 <sup>s</sup>	30°38'52.50"	217.10"	0.884 kpc
M33-3	1 <sup>h</sup> 33 <sup>m</sup> 48.99 <sup>s</sup>	30°20'24.58"	1242.13"	5.059 kpc
M33-4	1 <sup>h</sup> 33 <sup>m</sup> 25.63 <sup>s</sup>	30°20'25.25"	1290.30"	5.255 kpc
<b>Mi-Mo</b>				
M33-1	1 <sup>h</sup> 33 <sup>m</sup> 51.77 <sup>s</sup>	30°45'16.56"	367.50"	1.497 kpc
M33-2	1 <sup>h</sup> 34 <sup>m</sup> 16.75 <sup>s</sup>	30°36'35.64"	409.13"	1.666 kpc
M33-3	1 <sup>h</sup> 34 <sup>m</sup> 00.16 <sup>s</sup>	30°21'46.08"	1161.16"	4.729 kpc
M33-4	1 <sup>h</sup> 33 <sup>m</sup> 21.13 <sup>s</sup>	30°21'52.20"	1220.28"	4.970 kpc

Table 3.1: J2000.0 coordinates of the four fields. M33-1 and M33-2 are situated in the centre of the galaxy. M33-3 and M33-4 are in the southern spiral arm. Deprojected angular and linear distances of each field to the centre of the galaxy are given, assuming M33 is at a distance of 840 kpc, has an inclination angle of 53° and the major axis has a position angle of 22°.

camera meant that some objects were observed by both cameras in either both inner or both outer fields, giving up to 38 observations for objects in the overlap regions. All fields were observed with 300s exposure times.

### 3.3 Data Reduction

Preliminary reductions of the data were performed using the routines in the IRAF<sup>2</sup> CCDPROC package. This consisted of overscan correction, bias subtraction and flat fielding. The photometry was performed using the standalone DAOPHOT (Stetson, 1987) and ALLFRAME (Stetson, 1994) packages kindly provided by P. Stetson.

The data set used in this project is fairly large, containing over 300 images of the four fields. To process such a large data set, a completely automatic photometry pipeline was developed, covering all the steps from initial star selection to the final PSF photometry, details of which are given in Chapter 2.

---

<sup>2</sup>IRAF is distributed by the National Optical Astronomy Observatories, which are operated by the Association of Universities for Research in Astronomy, Inc., under cooperative agreement with the National Science Foundation.

### 3.3.1 Standard Calibration

Standard calibration of the photometry is essential to this work. The calibration must be as accurate as possible, as small differences in magnitudes could easily be misconstrued as differences in distance modulus. To this end, the IRAF PHOTCAL tasks were used to produce standard solutions for both the Imager and Mini-Mosaic cameras. The first step of the process is to put all the science images on the same instrumental zero-point as the corresponding reference night for the CCD in question, which is described in Section 2.8.2.

The Imager fields were calibrated using observations of Landolt standards (Landolt, 1992) taken on 1999 October 3rd. Three standard fields were imaged, containing 17 different standard stars. The observations were repeated through the night so that any time-dependent effects, such as changing extinction, could be taken into account in the final solution. Each star was measured in a 20 pixel aperture with the sky measured from an annulus from 25 to 30 pixels.

To generate a standard solution the aperture magnitudes are matched with the true magnitudes in the standard Landolt catalogue in IRAF. The solution takes the form

$$m_{inst} = m_{cal} + a + b \times X_M + c \times Colour + d \times UT \quad (3.1)$$

where  $m_{inst}$  is the instrumental magnitude,  $m_{cal}$  is the calibrated magnitude,  $X_M$  is the airmass and *Colour* corresponds to  $(B - V)$  for the  $B$  and  $V$  frames and  $(V - I_C)$  for  $I_C$ . The coefficients for each transformation equation are shown in Table 3.2. The *UT* term has units of hours, and was included in the solution as the extinction changed very slowly over the reference night. Although the coefficient of this term in the solution is much smaller than the others we believe that it is still important to include it. The aim of the process is to get the most accurate photometry possible, so if an effect is present and can be measured on a scale comparable to the accuracy we are trying to achieve then it should be considered. The transformation is then applied to *all* Imager frames using INVERTFIT.

Filter	a	b	c	d	RMS
$B$	24.155	0.276	-0.068	-0.006	0.010
$V$	24.305	0.201	-0.012	-0.006	0.011
$I_C$	23.714	0.090	-0.055	-0.003	0.019

Table 3.2: Photometric solution of 1999 October 3rd for the Imager CCD

This calibration is only appropriate for the frames taken with the Imager CCD. Once applied to the Imager frames, the stars on the reference frames could be used as local standards to derive separate photometric solutions for the two Mini-Mosaic CCDs. The reference night for the Mini-Mosaic was chosen to be 2000 October 3rd, as this had the best image quality for all fields. Stars that appeared in all frames of field 3 on both the photometric reference night and on the Mosaic reference night with  $\sigma_V \leq 0.02$  mag were selected as the local standards — around 200 stars for each chip. The PHOTCAL routines were used to find the solution of the transformation equations from the Mosaic instrumental magnitudes to the Imager Landolt calibration. For this transformation the time dependence and airmass term are absorbed into the zero-point coefficient of this solution and a quadratic colour term was added, resulting in transformation equations of the form

$$m_{MiMo} = m_{Im} + a + b \times \text{Colour} + c \times (\text{Colour})^2 \quad (3.2)$$

where  $m_{MiMo}$  refers to the magnitude on the Mini-Mosaic instrumental scale and  $m_{Im}$  refers to the calibrated Imager scale. The quadratic colour term of the Mini-Mosaic camera is a feature that has been described before by Stetson (2005). The coefficients of the equations are shown in Table 3.3.

By putting all the Mini-Mosaic frames on the same zero-point then transforming the magnitudes to the standard system used for the Imager frames, the Mini-Mosaic frames are themselves transformed to the Landolt system, removing the need to observe standards with every camera used.

Filter	a	b	c	RMS
<i>Chip 1</i>				
<i>B</i>	23.912	-0.094	0.017	0.049
<i>V</i>	24.148	-0.024	0.008	0.036
<i>I<sub>C</sub></i>	23.644	-0.037	-0.008	0.047
<i>Chip 2</i>				
<i>B</i>	23.912	-0.059	-0.014	0.049
<i>V</i>	24.147	0.013	-0.025	0.030
<i>I<sub>C</sub></i>	23.637	-0.061	0.004	0.046

Table 3.3: Photometric solution of 2000 October 3rd for the Mini-Mosaic Camera

### 3.3.2 Astrometry

The stacked frames created for making the ALLFRAME master lists were also used to perform the astrometry. The images are shown in Figures 3.2 and 3.3. In each case, the stacked images were matched by eye with a reference image of the region, to select a number of tie-point stars, around 10 in both cases. With these as a starting point, CCMAP was used to compute an initial astrometric solution. The entire catalogues are then fed into the task to compute a more accurate solution that can be applied to the whole image.

For the outer field the USNO-B catalogue (Monet et al., 2003) was used. A total of 5679 stars were matched, resulting in a solution with RMS values of 0.4''. The USNO-B catalogue was not appropriate for the inner field as it covers the central part of the galaxy, which is extremely crowded. For this region the astrometric solution was found by matching to the catalogues published in Massey et al. (2006). They also use USNO-B catalogue for this region but have many fewer stars, making it much easier to identify the tie-points. Again, CCMAP was used to compute an initial solution, then to match the whole image. This process gave a much better solution, with an RMS below 0.07'' from 3842 stars.

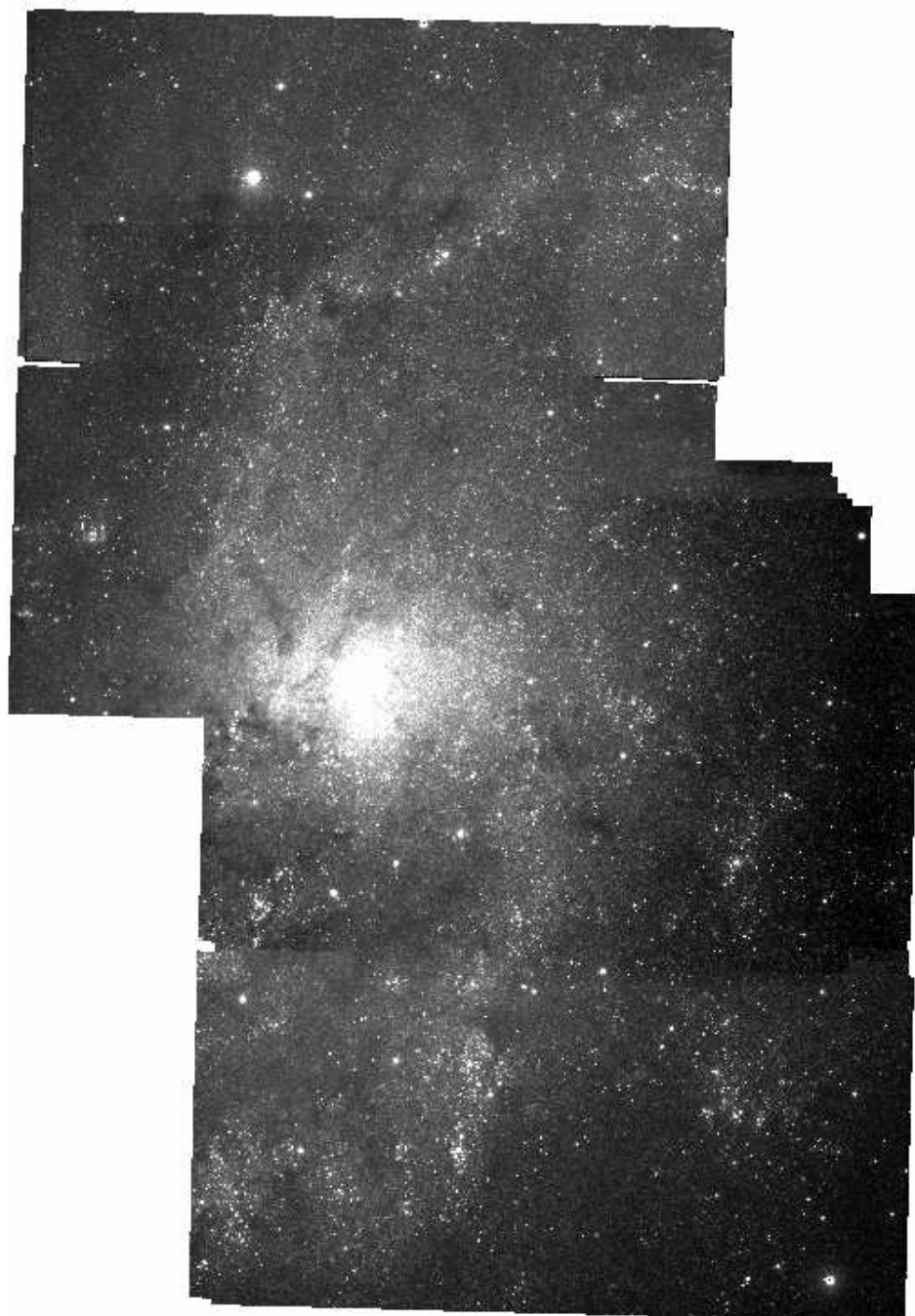


Figure 3.2: Median stacked image for the inner field. Orientation: North up, East right.

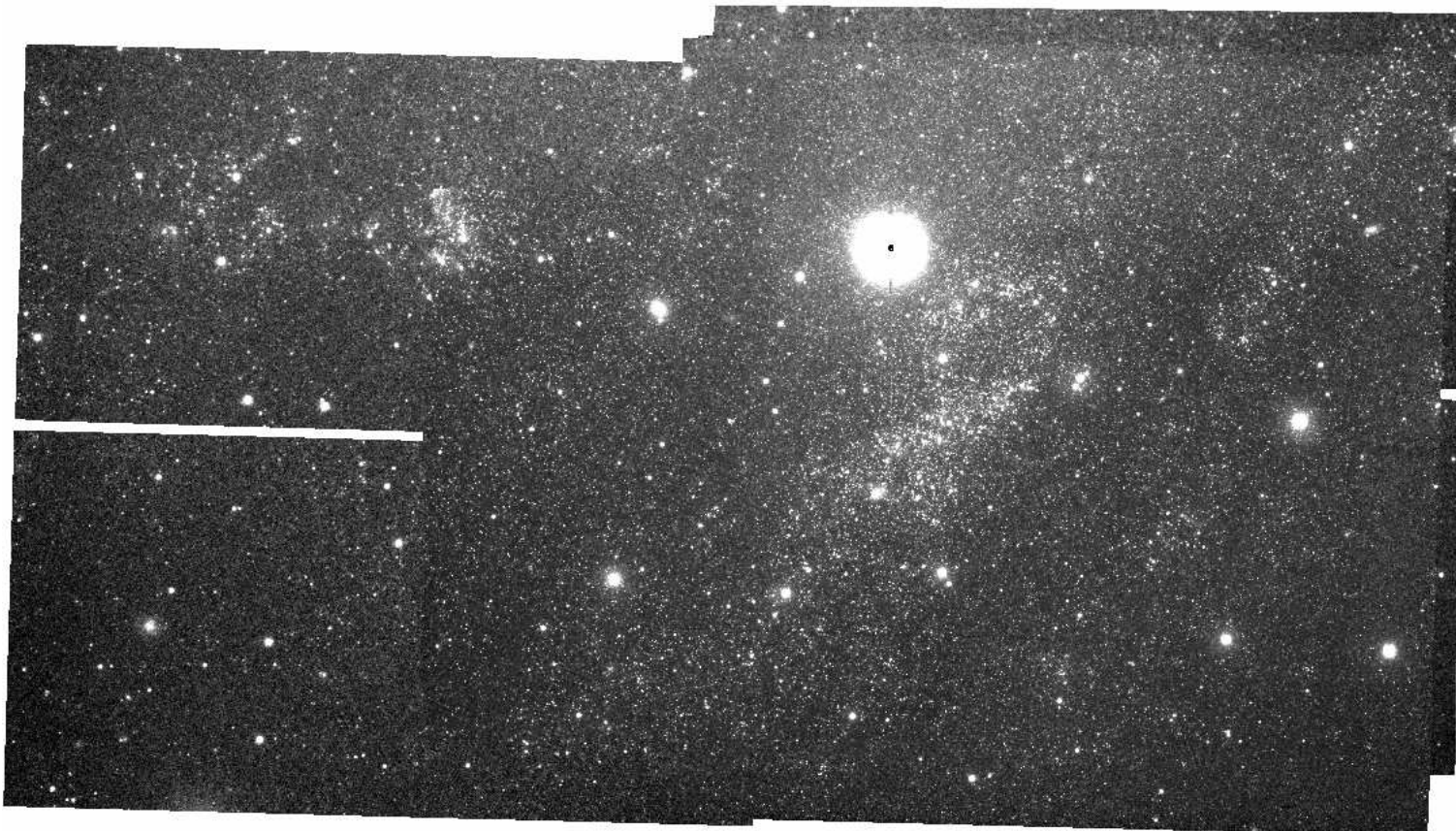


Figure 3.3: Median stacked image for the outer field. Orientation: North up, East right.

## 3.4 The Catalogues

Two catalogues were produced for the WIYN M33 Survey. The first contains weighted average  $B$ ,  $V$  and  $I_C$  magnitudes for each star. A sample of this catalogue is shown in Table 3.4. They cover the magnitude range between  $13.8 \leq V \leq 26.7$ , with 75465 and 146820 in the final outer and inner field lists respectively. The magnitude range of the inner field is limited slightly by the degree of crowding, and only contains objects down to  $V = 25.7$ . Colour–magnitude diagrams for both fields are shown in Figure 3.4. The second contains all the individual measurements for all the variables cross-identified with the Deep CFHT Photometric Survey of M33 (Hartman et al., 2006).

The uncertainties given in the average photometry catalogue are the errors on the weighted average magnitudes, calculated from the ALLFRAME results. Figure 3.5 shows the relation between magnitude and uncertainty for the  $V$  band in the outer field. A second series becomes visible around  $m_V = 20$  mag. These objects have fewer measurements, a maximum of five, as they appear only on the Mini-Mosaic frames (which has a large field of view than the Imager). However, a comparison between magnitudes calculated from the Imager and the Mini-Mosaic reference nights (illustrated in Figures 3.6 and 3.7) shows the photometry is compatible. Neglecting the second series in Figure 3.5 we obtain 1% photometry for objects brighter than  $m_V = 22$ , and 10% down to  $m_V = 24$ . The full analysis is shown in Table 3.5. These results are compatible with theoretical estimates from signal to noise calculations.

### 3.4.1 Comparison with the Local Group Survey

To check the accuracy of our results the average magnitudes were compared with those obtained by Massey et al. (2006). Their survey covers a larger area than the survey presented here but does not go as deep. The comparison for each filter in both fields is shown in Figures 3.8 and 3.9. The photometry from this work is considered as the reference, such that  $\Delta\text{mag} = m_{\text{Scowcroft}} - m_{\text{Massey}}$ . These plots show that the photometry is sound. Most objects have a difference near zero as expected. For the

ID	$\alpha$	hh:mm:ss	$\delta$	dd:mm:ss	B	$\sigma_B$	V	$\sigma_V$	$I_C$	$\sigma_I$	$N_B$	$N_V$	$N_I$
OUT-14501	1:33:10.21		30:17:22.7		24.946	0.423	23.733	0.161	99.999	9.999	1	1	0
OUT-14510	1:33:10.25		30:17:05.8		22.484	0.155	22.269	0.096	99.999	9.999	2	2	0
OUT-14523	1:33:10.26		30:17:07.2		22.525	0.092	22.872	0.075	99.999	9.999	2	2	0
OUT-14527	1:33:10.19		30:17:50.4		23.608	0.312	24.306	0.248	99.999	9.999	1	1	0
OUT-14532	1:33:10.26		30:17:15.2		23.475	0.109	22.943	0.067	99.999	9.999	2	2	0
OUT-14539	1:33:10.27		30:17:17.2		23.474	0.125	23.576	0.098	23.232	0.335	2	2	1
OUT-14546	1:33:10.27		30:17:23.2		24.193	0.184	23.556	0.092	23.002	0.219	2	2	1
OUT-14551	1:33:10.14		30:18:33.5		24.732	0.373	23.040	0.129	99.999	9.999	1	1	0
OUT-14554	1:33:10.17		30:18:20.5		22.238	0.096	22.313	0.075	99.999	9.999	1	1	0
OUT-14555	1:33:10.20		30:18:06.2		24.940	0.410	23.103	0.084	99.999	9.999	1	1	0

Table 3.4: Sample of the weighted averages catalogue. The uncertainties are from the weighted average calculations derived from the ALLFRAME results. Where no observations were made the magnitude and error are represented by 99.999 and 9.999 respectively.

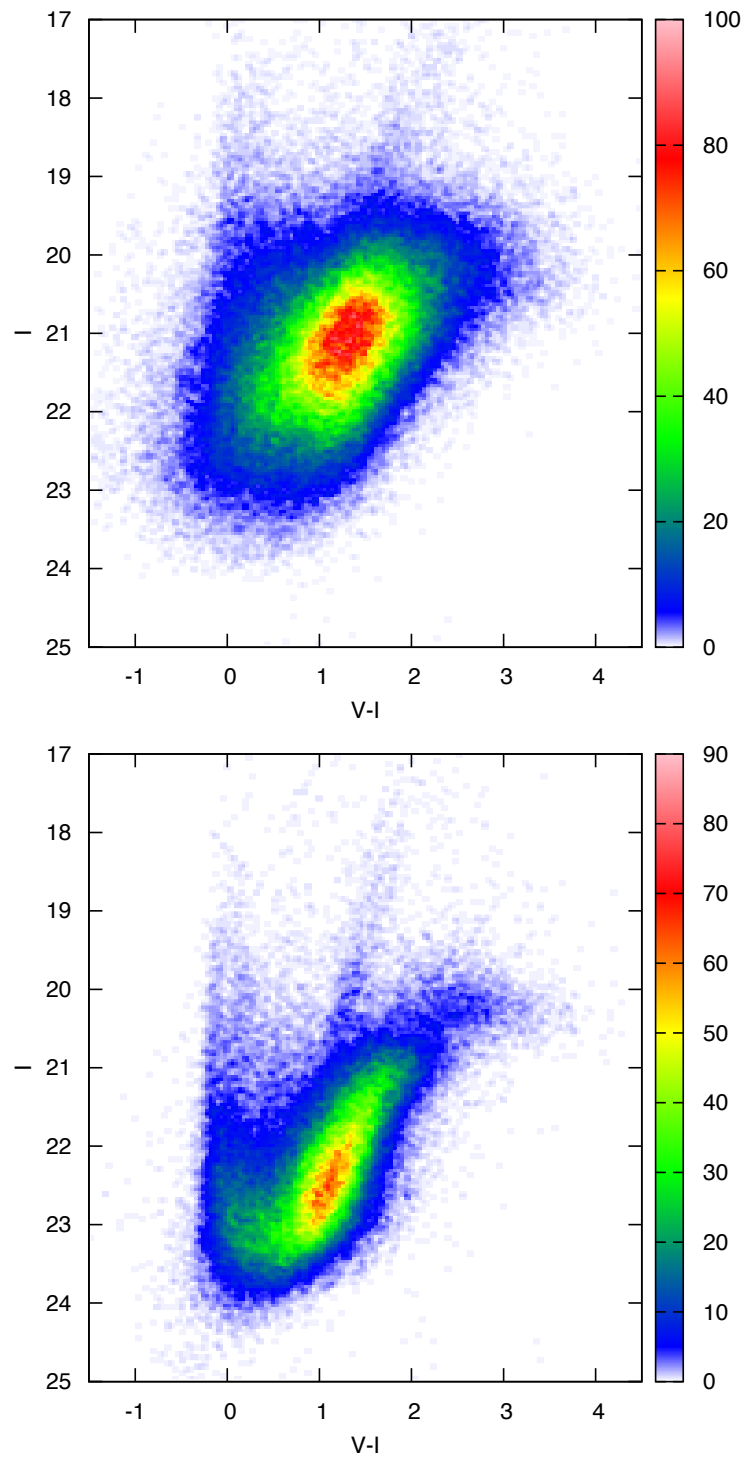


Figure 3.4: Hess diagrams for the inner (top) and outer (bottom) fields, with 0.025 mag bins. The inner field does not go as deep as the outer field as the degree of crowding is much higher. The effects of crowding and differential reddening are obvious in the inner field but are much less so in the outer field

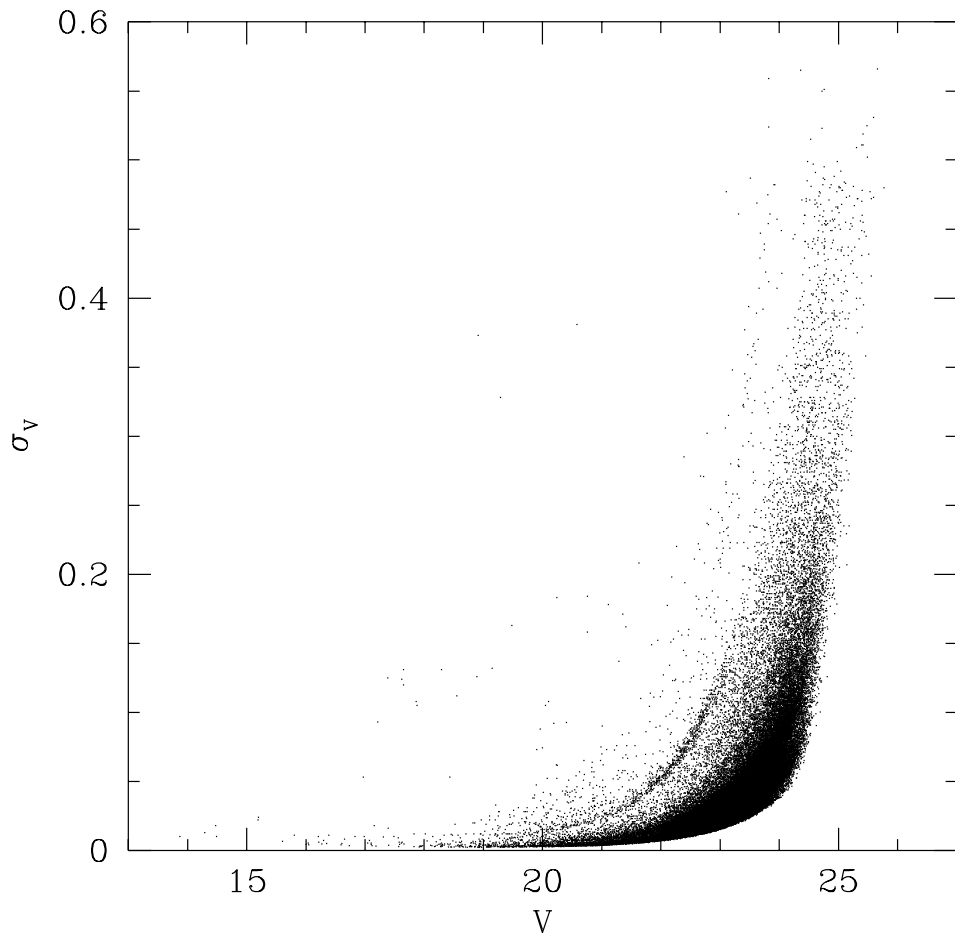


Figure 3.5: Magnitude –  $\sigma$  relation for  $V$  in the outer field. The second series with slightly higher uncertainties for a given magnitude is due to the Mini-Mosaic magnitudes dominating these objects, as these stars have few measurements.

Field	Filter	$\sigma = 1\%$	$\sigma = 10\%$
Inner	$B$	21.125	24.129
	$V$	21.693	23.854
	$I_C$	19.896	22.597
Outer	$B$	21.336	24.404
	$V$	22.136	24.195
	$I_C$	20.840	22.643

Table 3.5: Typical magnitudes and uncertainties from the weighted averages catalogue.

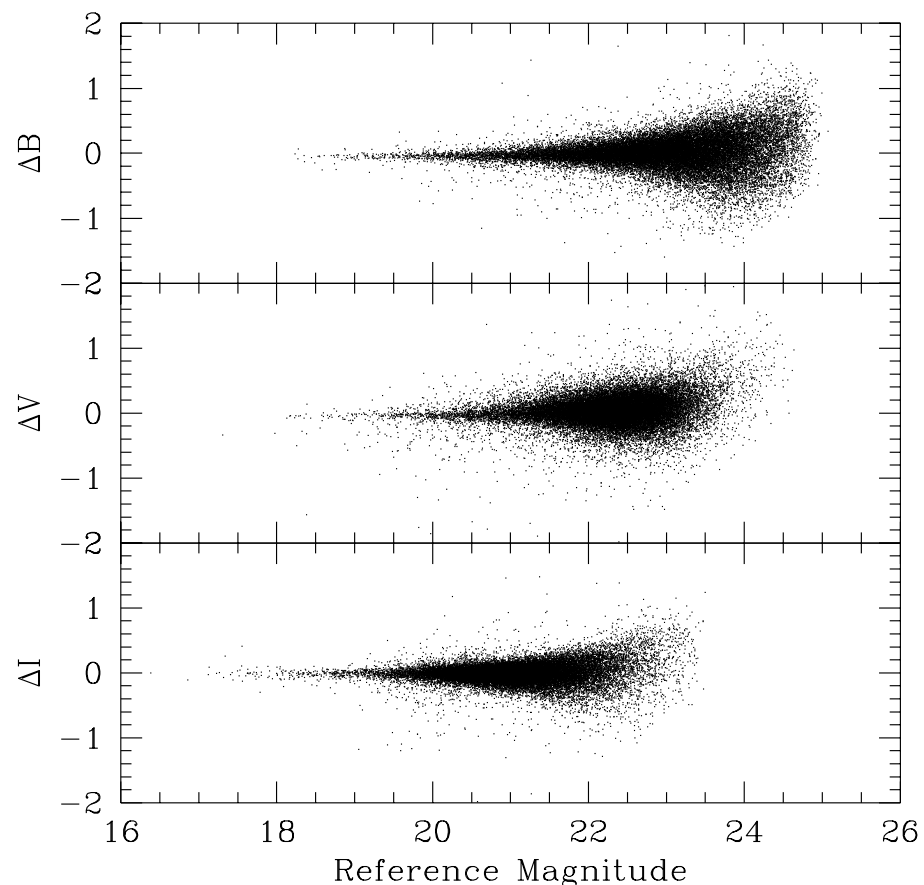


Figure 3.6: Comparison of Imager and Mini-Mosaic photometry for the inner field. In each case the reference magnitude is the calibrated Imager magnitude, and  $\Delta\text{mag} = \text{Imager} - \text{Mini-Mosaic}$ .

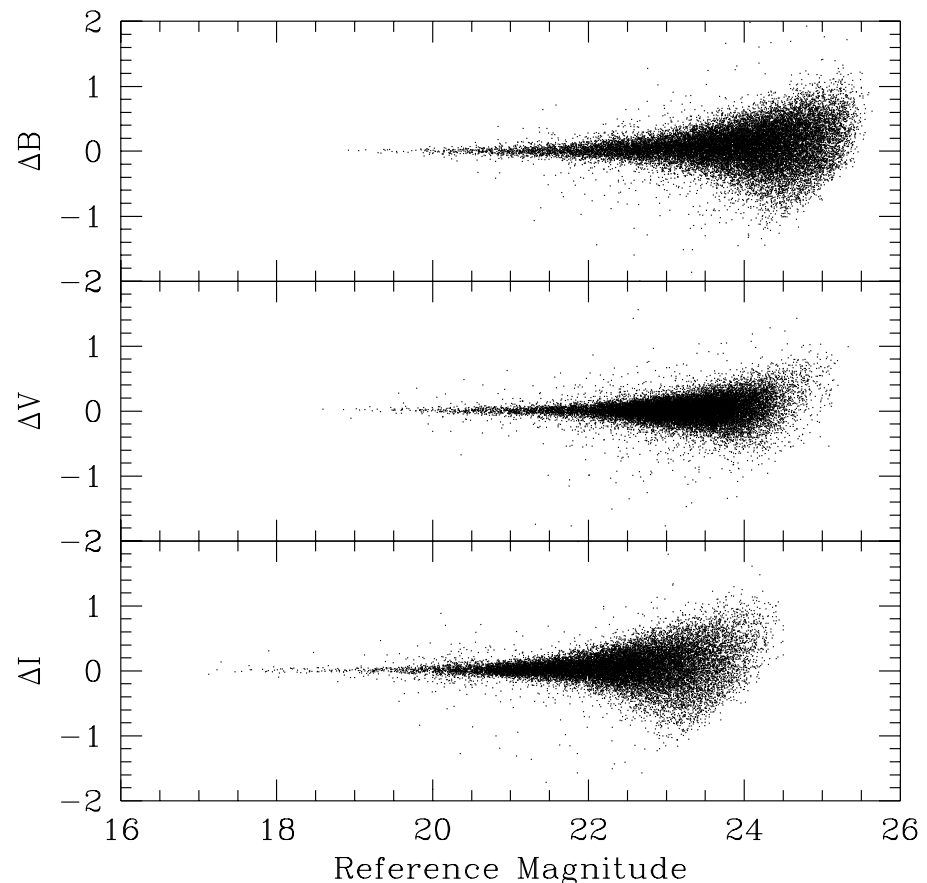


Figure 3.7: Comparison of Imager and Mini-Mosaic photometry for the outer field. In each case the reference magnitude is the calibrated Imager magnitude, and  $\Delta\text{mag} = \text{Imager} - \text{Mini-Mosaic}$ .

Field	Filter	$\Delta mag$	$\sigma_{\Delta mag}$	Range
Inner	$B$	0.008	0.005	16–19
	$V$	-0.009	0.008	15–18
	$I_C$	0.031	0.008	15–18
Outer	$B$	-0.013	0.008	16–19
	$V$	-0.014	0.005	16–19
	$I_C$	0.021	0.005	16–19

Table 3.6: Differences between weighted average magnitudes in this catalogue and Massey et al. (2006).  $\Delta mag$  was found from a least squares fit to the brightest end of the comparison, the range is given in column 4.  $\sigma_{\Delta mag}$  is the uncertainty on  $\Delta mag$ . Outliers with  $\Delta mag > \pm 0.5$  were rejected, as they are most likely misidentifications due to the crowding in the inner field.

inner field in particular, there seems to be a secondary sequence near  $\Delta mag \approx -0.8$ . We attribute this to misidentifications due to the high level of crowding. By excluding the central 4 arcmin of the galaxy from the comparison the effect was significantly reduced.

The average differences were found using a least squares fit to the brightest three magnitudes in the comparison and are shown in Table 3.6. Only the brightest stars in the comparison were chosen as the two catalogues are optimised for different magnitude ranges; were we to consider the whole range we would be basing the fit on the very faintest stars in Massey’s catalogue. However, gradients in  $\Delta mag$  were checked for, and the differences for each field–filter combination were found to be constant over the whole range of magnitudes. We find a larger average  $\Delta mag$  for  $I_C$ , which is believed to be because the  $I_C$  frames are more crowded than  $B$  and  $V$ , particularly in the inner field.

## 3.5 Cepheid Selection

The Cepheids were identified by cross referencing the catalogue with the fundamental mode Cepheid catalogue produced as part of the deep CFHT survey of M33 (Hartman et al., 2006). A full description of their data is given in Chapter 4. The fundamental

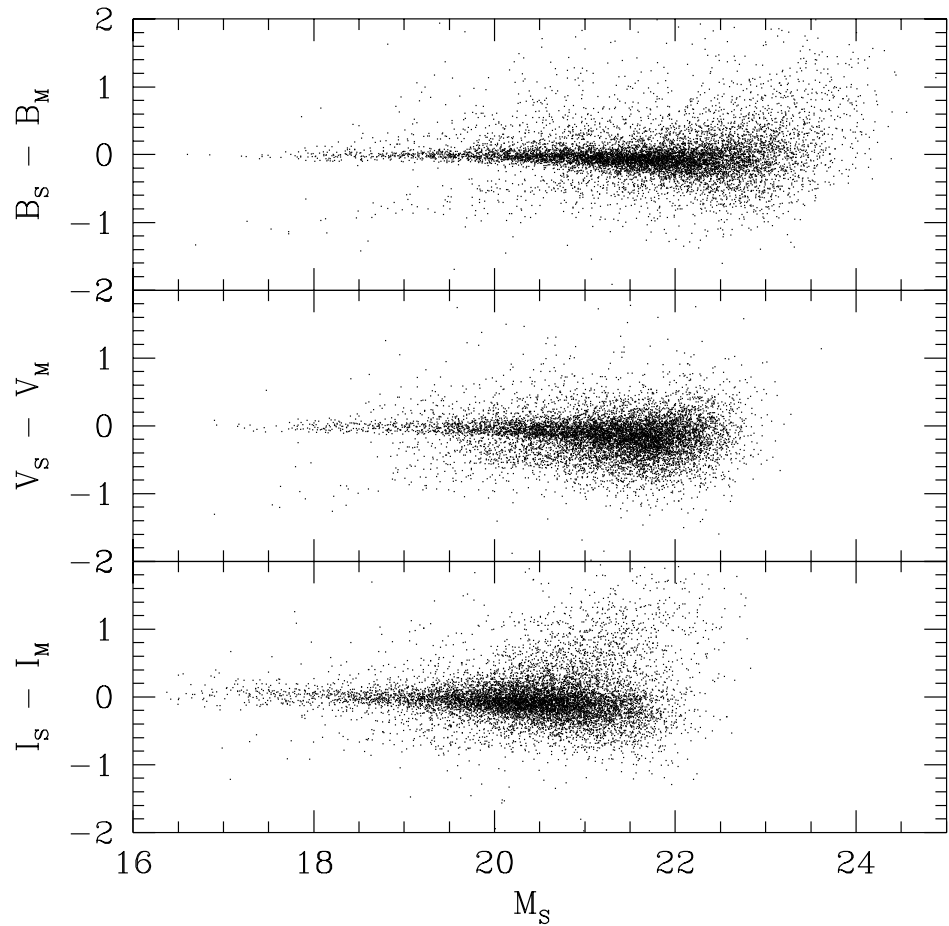


Figure 3.8: Comparison between this work and the catalogues of Massey et al. (2006) for the inner field. This work is considered to be the reference and is denoted by  $M_S$ , Massey et al. (2006) by  $M_M$  and  $\Delta\text{mag} = M_S - M_M$ . The average number of stars compared is 9700, corresponding to roughly 5% of our catalogue. All matched stars with  $\sigma < 0.5$  mag that were outside the central 4 arcmin were included. The secondary  $M_S - M_M < 0$  trends that are visible are believed to be due to the severe crowding of the region, as the matching algorithm used will tend to match to slightly brighter stars in highly crowded regions.

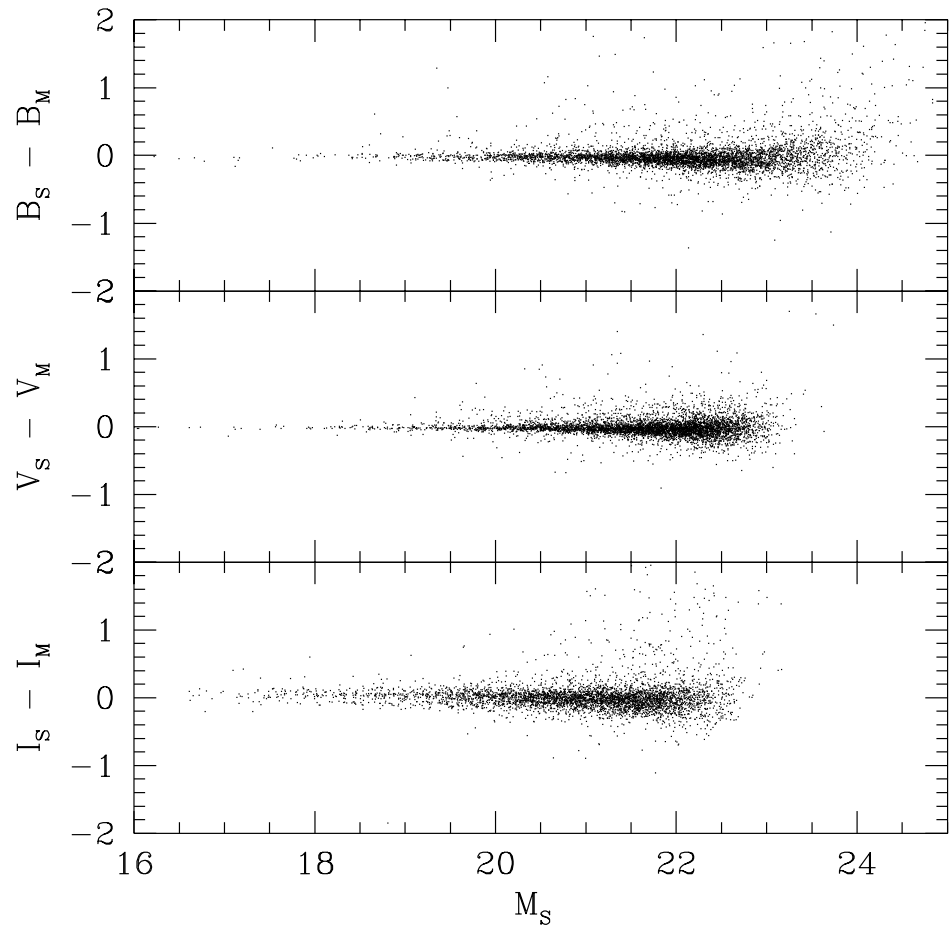


Figure 3.9: Comparison between this work and the catalogues of Massey et al. (2006) for the outer field. This work is considered to be the reference and is denoted by  $M_S$ , Massey et al. (2006) by  $M_M$  and  $\Delta\text{mag} = M_S - M_M$ . The average number of stars compared is 5100, corresponding to roughly 5% of our catalogue. All matched stars with  $\sigma < 0.5$  mag were included.

mode Cepheids were identified by J. B. Marquette using Fourier parameters (Simon & Lee, 1981). First overtone Cepheids were excluded from the analysis as they are known to sit slightly higher in the log  $P$ –Mag plane than fundamental Cepheids and would bias any zero-point fitting towards brighter magnitudes.

To ensure an accurate PL relation the average magnitudes for each Cepheid were recalculated by fitting Fourier series to the light curves, using the form shown in Equation 3.3, where  $m(\phi)$  is the magnitude at phase  $\phi$  and  $a$  becomes the phase averaged magnitude.

$$m(\phi) = a + \sum_{i=1}^3 b_i \cos(2\pi i \phi + c_i) \quad (3.3)$$

The light curve of each Cepheid was examined visually to remove any misidentifications or ones with incorrect periods. Obviously erroneous data points (ones which may have been affected by bad pixels within the PSF, for example) were removed, to ensure that the Fourier magnitudes were as accurate as possible.

The amplitude of each Cepheid was calculated and Cepheids with  $A_B > A_V > A_{I_C}$  were included in the final sample. This is similar to the selection criteria of Pietrzynski et al. (2002). Amplitude ratio selection is an important step as large numbers of classical Cepheids are known to exist in binary systems (Szabados, 2003). Very close companions would not be identified as separate stars in the initial photometry. They can however be identified by their characteristic effect on the Cepheid light curve. A Cepheid with an unidentified companion will still appear variable, but the light curve would not reach the minimum value expected. The effect will be seen to different extents in the different photometric bands depending on the colour of the companion. This explanation can also be extended to blending; if a Cepheid is within a background of unidentified faint stars these objects will affect the shape of the light curve in the same way. By requiring that the amplitudes of the Cepheids follow the criteria set out above we can remove these effects from the sample. The visual inspection and amplitude selection left 91 and 28 Cepheids in the inner and outer field samples respectively.

Band	$a_{LMC}$	$b$	$\mu$
<b>Inner field</b>			
$B$	$-2.393 \pm 0.040$	$23.92 \pm 0.04$	$24.97 \pm 0.06$
$V$	$-2.374 \pm 0.028$	$23.47 \pm 0.03$	$24.82 \pm 0.04$
$I_C$	$-2.957 \pm 0.020$	$22.84 \pm 0.02$	$24.65 \pm 0.03$
<b>Outer field</b>			
$B$	$-2.393 \pm 0.040$	$23.85 \pm 0.06$	$24.89 \pm 0.07$
$V$	$-2.374 \pm 0.028$	$23.52 \pm 0.04$	$24.87 \pm 0.05$
$I_C$	$-2.957 \pm 0.020$	$22.88 \pm 0.03$	$24.69 \pm 0.04$

Table 3.7:  $B, V, I_C$  period–luminosity relations for the two WIYN fields.  $a_{LMC}$  represents the slope of the LMC PL relation taken directly from F07,  $b$  is the zero–point from a least–squares fit to the data. The distance modulus found from each relation is given in the final column. This assumes that  $\mu_{LMC} = 18.4$ . The distances have not been corrected for reddening.

## 3.6 Cepheid Period–Luminosity Relations

PL relations were fitted to the Cepheids in both fields in  $BVI_C$ . The PL relations take the form  $M = a \log P + b$ . The values for the slopes,  $a$ , were taken directly from the Fouqué et al. (2007) (hereafter known as F07) LMC relations, whilst the intercept,  $b$ , was derived from an iterative weighted least–squares fit for each relation. The  $BVI_C$  relations are shown in Figures 3.10 and 3.11. The distance modulus can be found from the apparent magnitude of a Cepheid with a period of one day, such that  $\mu = b - M_0$ , where  $b$  is the zero–point of the PL relation and  $M_0$  is the absolute magnitude of a one day Cepheid, which is taken directly from the LMC PL relations from F07. The equations for each relation are shown in Table 3.7. The derived distance modulus ( $\mu$ ) for each band is given in the final column, although it is important to note that the distance moduli have not been corrected for reddening.

At first glance, the fits shown in Figure 3.11 may look incorrect — this is not the case. The PL relations were found by fixing the value of the slope to the LMC slope value from F07, with the zero–point fitted using an iterative weighted–least–squares method. This was found to be the most robust technique, as it accounted for the larger uncertainties on the fainter stars. As the slope was fixed, an unweighted fit would have

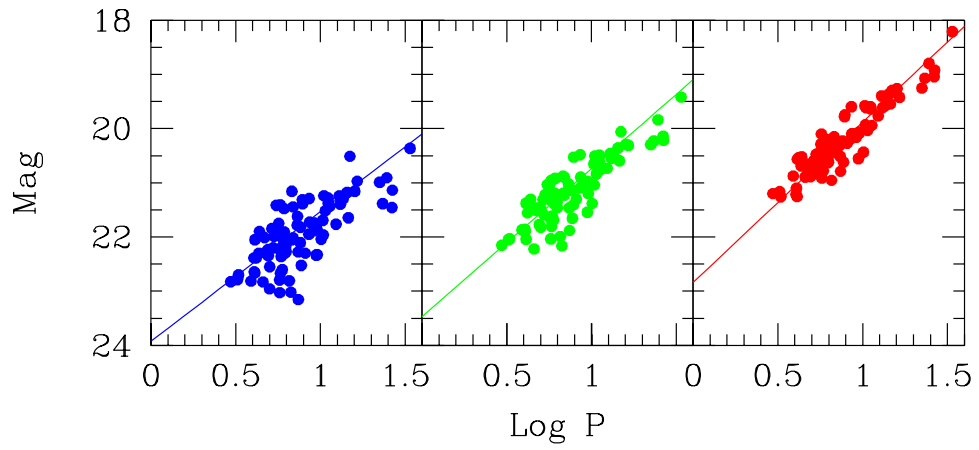


Figure 3.10: PL relations for the inner field,  $B, V$  and  $I_C$  go from left to right. The lines correspond to fits based on the LMC PL relations described in Fouqué et al. (2007). The slope was kept constant, with the zero-point fitted using an iterative weighted-least-squares technique. The magnitudes have not been corrected for reddening

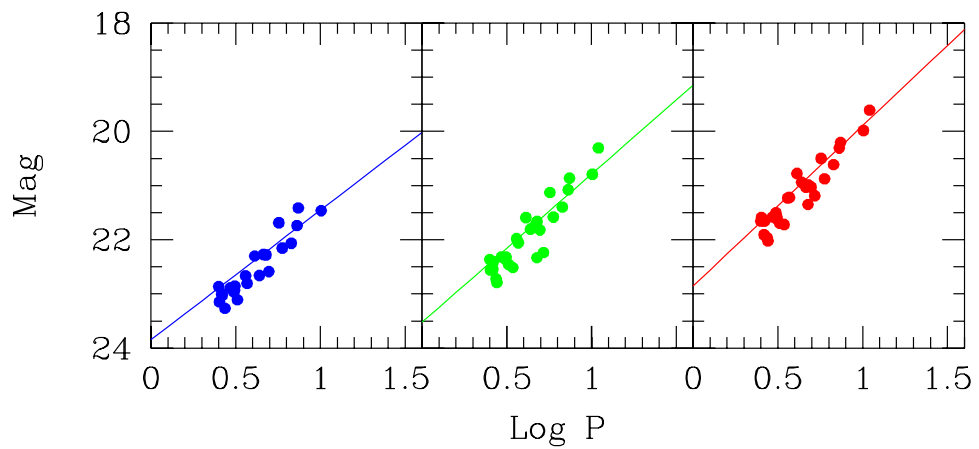


Figure 3.11: PL relations for the outer field,  $B, V$  and  $I_C$  go from left to right. The lines correspond to fits based on the LMC PL relations described in Fouqué et al. (2007). The slope was kept constant, with the zero-point fitted using an iterative weighted-least-squares technique. The magnitudes have not been corrected for reddening

been dominated by the shortest period Cepheids, as the period distribution is dominated by these Cepheids. Had the fit not been weighted in this way, the zero-point would have been biased towards fainter magnitudes.

The zero-points in Table 3.7 appear to be discrepant. There are several possible explanations for the difference we observe:

1. Different amounts of dust, and therefore extinction, in the two fields.
2. Blending affecting the magnitudes of Cepheids in the inner field.
3. Differing period distributions of the two samples and a possible slope change at  $P = 10$  days.
4. Differing metallicity in the two fields.

Each of these issues will now be addressed in the following sections.

### 3.6.1 Extinction and reddening effects

The first effect that we must eliminate if we are to assess the metallicity effect is that of interstellar dust. The observational signature of line-of-sight material manifests itself in a similar way to metallicity differences; that is, it will change the observed colour and magnitude of the Cepheid. However, unlike composition effects, the effects of dust can be calculated and removed.

Extinction and reddening are quantified by the terms  $A_X$  and  $E(X - Y)$ , where  $X$  and  $Y$  denote the passbands in question, for example,  $A_V$  and  $E(B - V)$ .  $E(X - Y)$  is also known as the colour excess. The relationship between extinction and reddening at different wavelengths is described by the reddening law:

$$R_V = \frac{A_V}{E(B - V)}. \quad (3.4)$$

The reddening law can be used to determine extinction values at different wavelengths via the parametrisation described by Cardelli et al. (1989), which is shown in Fig-

ure 3.12. The parametrisation is a complicated polynomial, but in the wavelength range considered here ( $BVI_C$ ) the law can be accurately approximated by a linear function, as shown by the solid line in the plot. The equation of fit to the  $BVI_C$  points is

$$\frac{A_\lambda}{A_V} = \frac{0.69}{\lambda(\mu m)} - 0.26 \quad (3.5)$$

where  $A_\lambda$  is the extinction at wavelength  $\lambda$ ,  $A_V$  is used to normalise the extinction to the  $V$  band, and the uncertainties in brackets are from the least-squares fit. Note that the  $R$  band is excluded from this analysis. The bump in the polynomial fit at  $R$  raises  $A_R$  higher than the linear fit and increases the uncertainty. As no  $R$  band data is included in this survey we can safely ignore this point.

The extinction terms and colour excess can both be calculated directly from the Cepheid distance moduli, using the linear approximation described above. Figures 3.13 and 3.14 show the distance moduli from Table 3.7 plotted against the inverse effective wavelength. The solid lines show the weighted least-squares fit to the points, with the dashed lines representing the uncertainty on the fit. The uncertainty on the fit to the outer field data is much larger than that of the inner field. This is because the  $\sigma_\mu$  for the outer field are larger as a smaller sample of Cepheids was used.

The best-fit lines take the form

$$\mu_{inner} = \frac{0.30(\pm 0.01)}{\lambda(\mu m)} + 24.27(\pm 0.03) \quad (3.6)$$

$$\mu_{outer} = \frac{0.22(\pm 0.07)}{\lambda(\mu m)} + 24.43(\pm 0.11) \quad (3.7)$$

where  $\mu_{region}$  represents the distance modulus for the appropriate region and  $\lambda$  is the effective wavelength. That the gradients of the fits are not the same as each other, or for that matter, the same as the theoretical fit, is unsurprising. Firstly, the theoretical model is fitting a function for  $A_\lambda/A_V$ , whereas the Equations 3.6 and 3.7 are both fitting for  $\mu$ . Secondly, the slope of the two observational fits depends not only on  $R_V$ , but also on  $A_V$ . Although it may be reasonable to expect that the physical properties of the interstellar medium to be the same in the two fields, it would be naive to expect

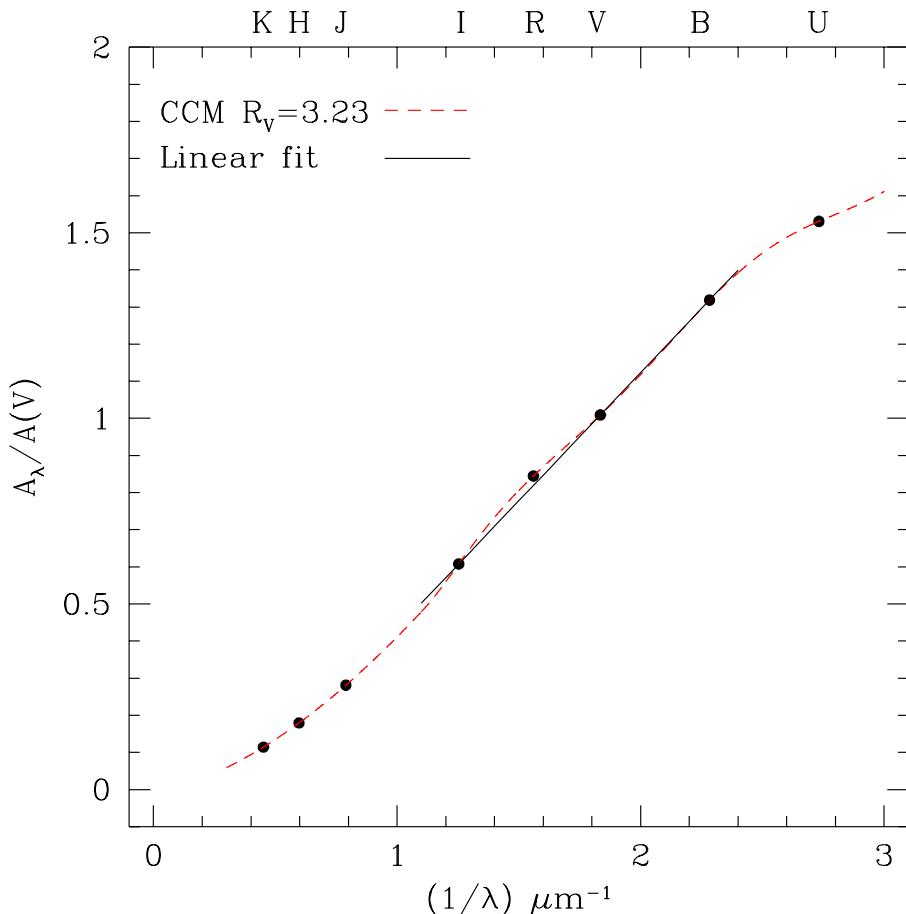


Figure 3.12: Comparison of the reddening law from Cardelli et al. (1989) and a linear fit to the  $B,V$  and  $I_C$  points. The linear model takes the form  $\frac{A_\lambda}{A(V)} = \frac{0.69}{\lambda(\mu\text{m})} - 0.26$ , and is found to be an excellent fit to the range considered. Effective wavelengths ( $\lambda$ ) taken from table A2 of Bessell et al. (1998) ( $UBVRI_C$ ) and table 6 of Schlegel et al. (1998) ( $JHK$ ).

Field	$E(B - V)$	$E(V - I)$
Inner	$0.135 \pm 0.005$	$0.175 \pm 0.007$
Outer	$0.098 \pm 0.030$	$0.127 \pm 0.039$

Table 3.8: Colour excesses derived from fits to Cepheid distance moduli, using Equation 3.9

the *amount* of material to remain unchanged.

Using Equations 3.6 and 3.7 we can calculate the values for  $E(B - V)$  and  $E(V - I)$  for the two samples. If it is assumed that the zero-point term in Equations 3.6 and 3.7 represent the true, reddening-free distance modulus  $\mu_0$ <sup>3</sup>, then we can derive the colour excesses from the individual  $\mu$ s. For example, to derive  $E(B - V)$ , we use  $\mu_0$ ,  $\mu_B$  and  $\mu_V$ :

$$\mu_0 = \mu_B - A_B = \mu_V - A_V, \quad (3.8)$$

As  $\mu_0$  should be the same no matter which passband is used to calculate it, it can be removed and the colour excess term constructed using the fitted values of  $\mu_B$  and  $\mu_V$ :

$$E(B - V) = A_B - A_V = \mu_B - \mu_V \quad (3.9)$$

The same construction follows for  $E(V - I)$ . The colour excesses found using this method are shown in Table 3.8. Note that the raw values are not used as the uncertainty on the fit is much smaller than the uncertainties on the individual  $\mu$ s.

The values found for  $E(B - V)$  and  $E(V - I)$  in this rough calculation are similar to those found by Chandar et al. (1999). However, before reddening can be eliminated from the problem, it must be ensured that the reddening law itself is appropriate for *both* fields. This is done by taking the analysis in Equation 3.8 a step further.

The first step is to calculate  $A_X$  values for each pass-band, using  $R_V = 3.23$  and the  $E(B - V)$  terms shown in Table 3.8. From these we can then obtain  $E(V - I)$ . If the

---

<sup>3</sup>This is an incorrect assumption. It is clear from Figure 3.12 that the true reddening curve flattens off at the infra-red end, and in the theoretical case the linear fit would underestimate the true distance modulus by 0.257 mag. However, this does not affect the current calculation.

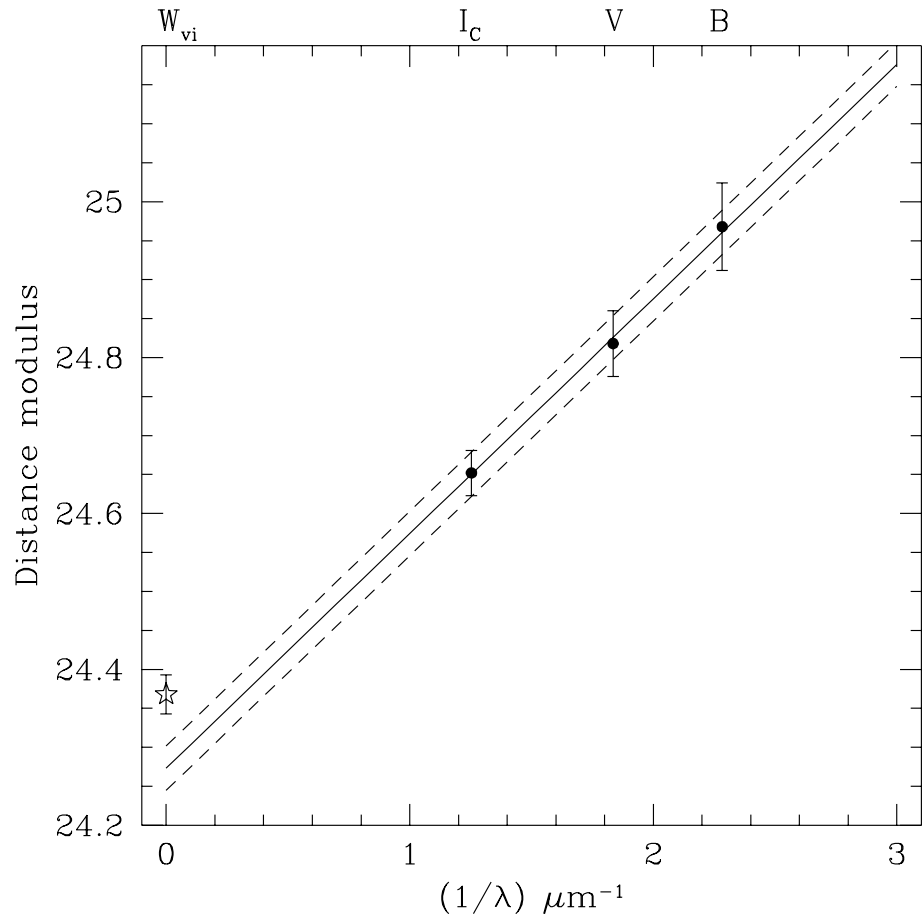


Figure 3.13: Determination of the reddening terms for the inner field using Cepheid distance moduli. Filled circles represent the  $BVI_C$  distances, the empty star shows the reddening-free  $W_{vi}$  distance modulus. The solid line shows the weighted least-squares fit to the  $BVI_C$  points; the two dashed lines represent the uncertainty on the zero-point.

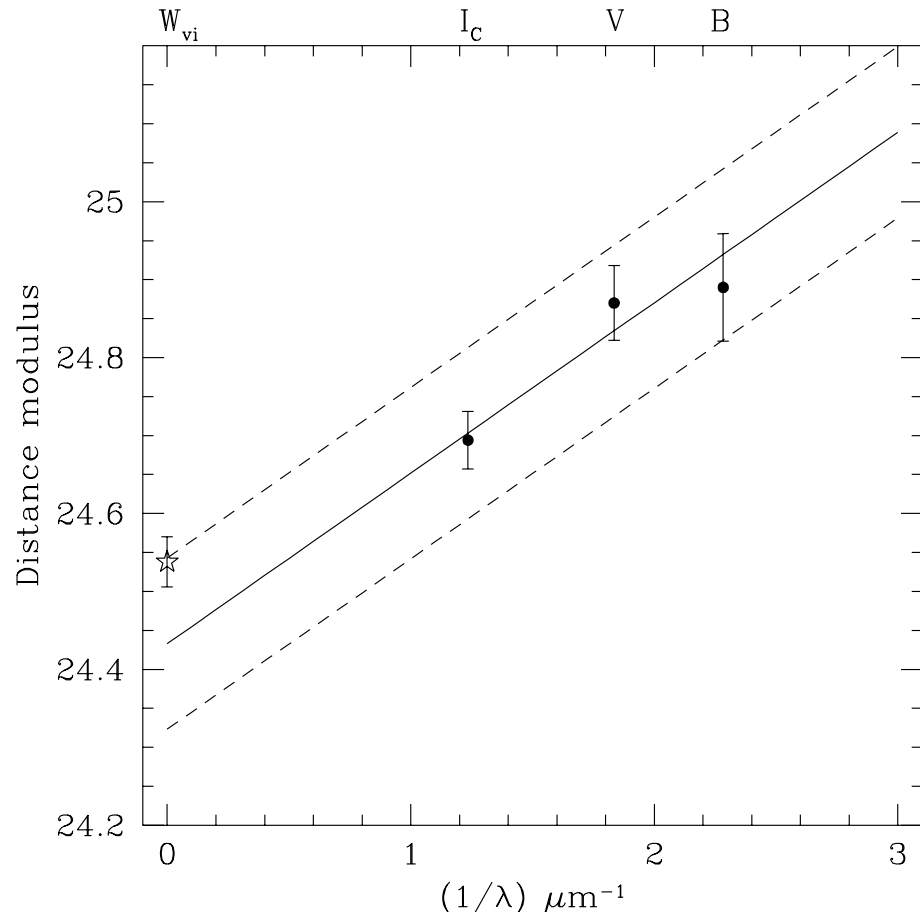


Figure 3.14: Determination of the reddening terms for the outer field using Cepheid distance moduli. Filled circles represent the  $BV I_C$  distances, the empty star shows the reddening-free  $W_{vi}$  distance modulus. The solid line shows the weighted least-squares fit to the  $BV I_C$  points; the two dashed lines represent the uncertainty on the zero-point.

Field	$A_B$	$A_V$	$AI$	$E(V - I)$
Inner	$0.571 \pm 0.021$	$0.436 \pm 0.021$	$0.265 \pm 0.010$	$0.171 \pm 0.006$
Outer	$0.415 \pm 0.127$	$0.317 \pm 0.097$	$0.193 \pm 0.059$	$0.124 \pm 0.038$

Table 3.9: Derived values for extinction terms and colour excesses using the  $R_V = 3.23$  reddening law. The  $E(V - I)$  terms are compatible with those derived from Figures 3.13 and 3.14. This shows that the selected reddening law is appropriate for both fields.

reddening law changed between the two regions, the  $E(V - I)$  values found using the two methods would not match for both regions, although it is plausible that they would be the same for one or the other region. The derived extinction and colour excesses are shown in Table 3.9. The  $E(V - I)$  values in the final column are compatible with those in Table 3.8. Note that throughout the analysis no assumption about the value of the true distance modulus has been made.

This means that, not only are the two linear approximations appropriate, but that the same reddening law applies to both fields. This allows extinction to be eliminated from the problem, via the reddening–free Wesenheit index.

### 3.6.2 Reddening–Free Wesenheit Index

The reddening–free Wesenheit index  $W_{vi}$  was first described by Madore (1976). It uses the nature of the reddening law itself to construct a pseudo–magnitude that is independent of any effects from line–of–sight material. The index is constructed using two colours (in this case  $V$  and  $I_C$ ), following the method outlined in Madore & Freedman (2009), defining  $W_{vi}$  as

$$W_{vi} = V - R_V \times (V - I) \quad (3.10)$$

where  $W_{vi}$  is the reddening–free index and  $R_V$  is the ratio of visual extinction to colour excess, defined in Equation 3.4, but this time using the  $(V - I)$  colour excess. By substituting in the extinction and colour excess terms, Equation 3.11 is obtained:

$$W_{vi} = V_0 + A_V - R_{vi} \times ((V - I)_0 + E(V - I)) \quad (3.11)$$

Field	$a_{LMC}$	$b$	$\mu$
Inner	$-3.320 \pm 0.011$	$21.85 \pm 0.02$	$24.37 \pm 0.02$
Outer	$-3.320 \pm 0.011$	$22.01 \pm 0.03$	$24.54 \pm 0.03$

Table 3.10: Coefficients of the reddening-free  $W_{vi}$  PL relations. The slope values ( $a$ ) are taken directly from F07, the zero-points ( $b$ ) are derived from a iterative least-squares fit. The distance moduli assume  $\mu_{LMC} = 18.4$  mag.

Expanding the second term out shows that the  $A_V$  and  $E(V - I)$  terms cancel, leaving only the reddening-free terms, such that the uncorrected  $W_{vi}$  index is equal to the reddening free index:

$$W_{vi} = V_0 - R_V \times (V - I)_0. \quad (3.12)$$

To complete the definition of  $W_{vi}$ , the correct ratio of total-to-selective absorption must be substituted into Equation 3.10, using the  $A_V$  and  $E(V - I)$  values, such that

$$W_{vi} = V - 2.55(V - I_C). \quad (3.13)$$

Figure 3.15 shows the  $W_{vi}$  PL relations for both fields. The zero-points of the PL relations for  $W_{vi}$  can be used to directly infer the distance modulus of M33, without the need to correct for extinction. These values are shown in Table 3.10, and plotted as empty stars in Figures 3.13 and 3.14. In both cases, the  $W_{vi}$  distances sit higher than the linear fit, but this is expected. As was shown in Figure 3.12, the extinction curve flattens out as the wavelength is increased. Hence the reddening free  $\mu$ , which is essentially at infinite wavelength, will sit higher than predicted by the linear fit.

As a final check, the de-reddened distance moduli are compared with those from the Wesenheit relations in Table 3.11. This clearly shows that both methods are in agreement and the measured distances of the two fields are not the same. This implies that a factor other than extinction is coming in to play in the distance measurements.

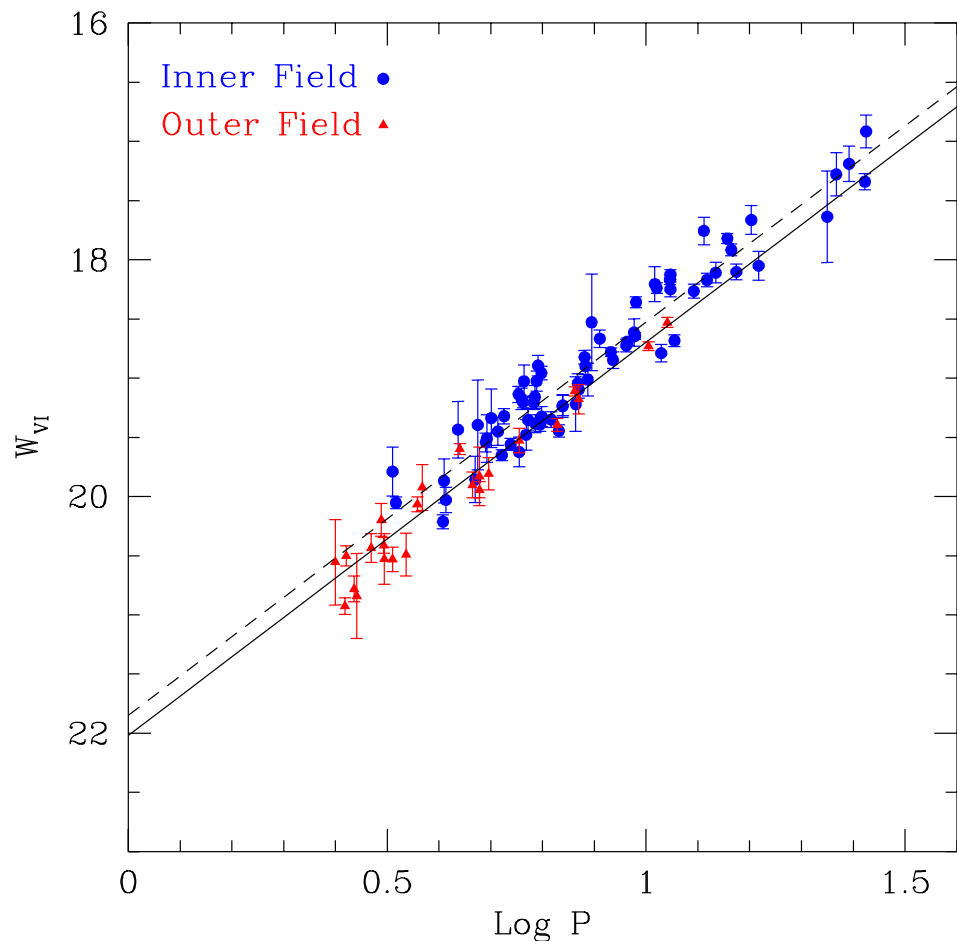


Figure 3.15: Reddening–free Wesenheit  $W_{vi}$  PL relations for the inner field (blue circles) and the outer field (red triangles).

Filter	$\mu_{inner}$	$\mu_{outer}$	$\Delta\mu$
$B$	$24.40 \pm 0.06$	$24.48 \pm 0.15$	0.08
$V$	$24.38 \pm 0.05$	$24.55 \pm 0.11$	0.17
$I$	$24.42 \pm 0.03$	$24.50 \pm 0.07$	0.08
$W_{vi}$	$24.37 \pm 0.02$	$24.54 \pm 0.03$	0.17

Table 3.11: Comparison of  $W_{vi}$   $\mu$ s with de–reddened  $B, V, I_C$   $\mu$ s.

### 3.6.3 Blending

The most obvious suggestion to explain the discrepant distance moduli is the fact the the inner field is extremely crowded, and there may be Cepheids with undetected companions in the sample which will affect any PL relation zero-point that we try to fit. However, this is not believed to be the cause of the observed deviation.

Firstly, the photometry procedure is based on ALLFRAME which uses a deep image, made by stacking many individual exposures, to do the photometry on each individual frame. When the photometry is done on this deep reference frame, the signal-to-noise ratio for each object is much higher than on individual images, making it easier to recognise, and classify as such, stars that may be blended.

Secondly, the comparison of the photometry with Massey et al. (2006) shows excellent agreement. Massey et al. use images with individual exposure times of 60 sec in *BV* and 150 sec in *I*; in other words they are up to 5 times less deep than this data. This means that the level of crowding and blending will be less severe than our this work. Yet, our photometry is found to be in excellent agreement with theirs, for both fields, over the whole magnitude range covered by both surveys. If this study was sensitive to blending levels that Massey et al. do not see, there should be a systematic offset between the two catalogues. However, as there is not a quantifiable offset in either Figure 3.8, 3.9 or Table 3.6 blending can safely be ruled out as the cause of the difference in distance modulus for the two fields.

Blending can also be ruled out as the cause on a theoretical level. Ferrarese et al. (2000) addressed this issue, in the context of the HST Key–Project, with artificial star tests. They did this for 2 galaxies with fairly different levels of crowding. Their main conclusion was that blending has little impact on distance moduli, provided the Cepheids used to derive the distance are carefully selected. Our sample was selected using amplitude ratios, as well as visual inspection of each of the light curves, so we are confident that the sample is clean.

It is useful to note however, the same  $\Delta\mu$  was found between the outer and inner fields

using both the raw and selected Cepheid samples, although the PL relation constructed from the selected sample has a much lower dispersion than that of the raw sample. This reduces the uncertainty on the fit, but also provides indirect evidence that blending is not an issue.

A final comparison is made with the study of NGC 4258 by Macri et al. (2006), who also find that observed Cepheid distance modulus depends on metallicity. To ease the comparison with this survey, the numbers are converted into stars per square of 10x10 pixels. In their  $V$  band catalogues there are 1.8 and 0.6 star per 10x10 square for the inner and outer fields respectively. In M33 (considering only the Imager fields — stars included *only* in the Mini Mosaic fields were excluded from the Cepheid analysis as they had very few observations), we have of order 80000 stars in the inner field, 40000 in the outer field. For the inner field this is about 1 star per 100 square pixels, for the outer field this corresponds to 0.5 star per 100 square pixels. Our numbers of stellar density are smaller than those of NGC 4258 observed with ACS. The scale of these images in parsec pixel $^{-1}$  is much better than HST even with ACS, as the PSF is oversampled. This means that even though the number of stars per pixel in both data sets are not so different, the WIYN data *resolve* stars in M33 better than ACS in NGC 4258.

One may argue that because the stellar densities are similar in M33 and NGC 4258, both results are equally affected by blending. This is not so. Macri et al. found a Cepheid distance modulus 10.88 mag larger than the modulus of the LMC. Adopting  $\mu = 18.4$  for the LMC gives  $\mu = 29.28 \pm 0.04$ . This compares very well with the maser distance to NGC 4258 ( $\mu = 29.29 \pm 0.09$ , Herrnstein et al. (1999)). Given the agreement between Cepheid and maser distances, blending has little effect on the Cepheid distance, hence it has little or no effect on the differing values of  $\mu$  for the two fields.

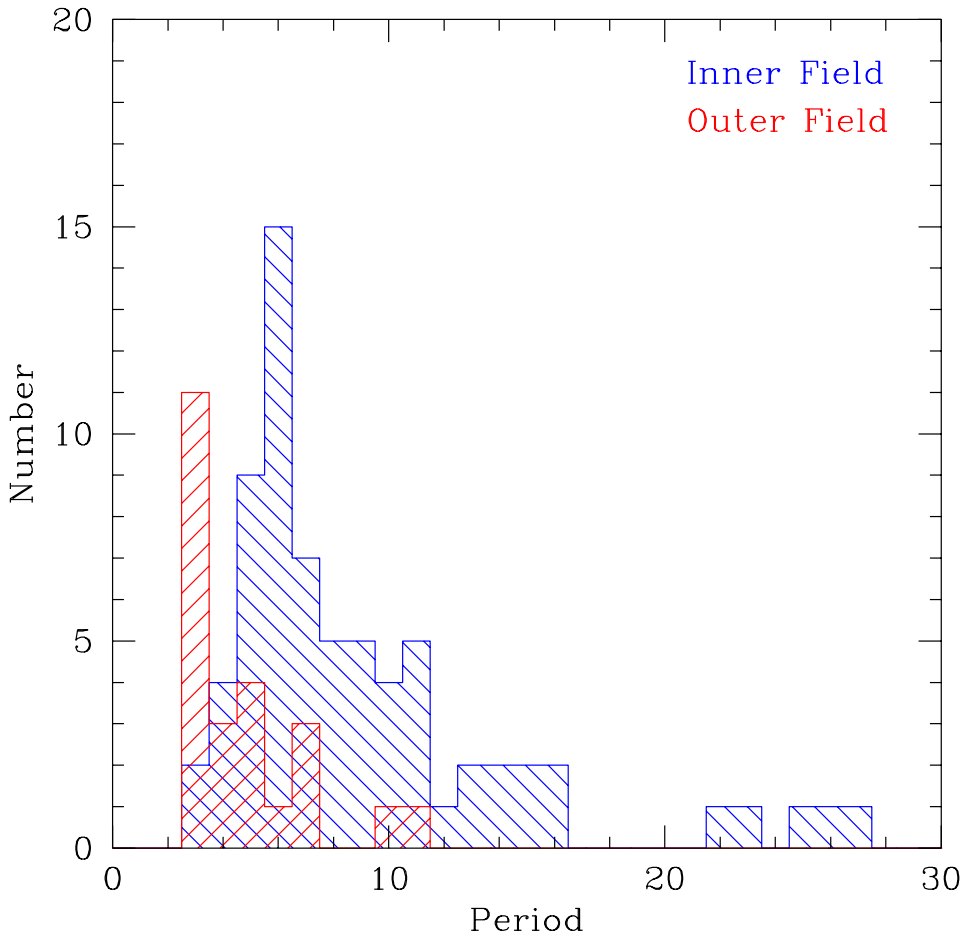


Figure 3.16: Period distribution of the two Cepheid samples used to fit the  $W_{vi}$  PL relations

### 3.6.4 Period Distribution and Slope Changes

The third possibility for the differing values for the distance modulus of M33 is the period range of the two samples. The distribution of periods in the final sample is shown in Figure 3.16. It is quite clear that the period distribution of the two regions is not the same. This is for two reasons. Firstly, the short period Cepheids are fainter so we detect more of them in the outer field where the detection limit is lower. Secondly, long period Cepheids are rarer than their short period counterparts. Therefore, we expect the ratio of long period Cepheids to total number of stars detected to be quite low, hence they will be preferentially detected in the region with a higher number of stars; in this case the inner region.

There is some observational evidence that the slope of the  $B$ ,  $V$  and  $I_C$  PL relations change around 10 days (e.g. Ngeow et al. (2009)). However, there is still debate about whether this effect is real, and if the same non-linearity will appear in the  $W_{vi}$  relation. To rule out any possible slope change as the cause of the discrepant distance moduli the samples were both cut to  $P < 10$  days and the PL relations refitted. Note that no attempt is made to determine if any non-linearity is present or to quantify the effect, just to eliminate the possibility; such tests would require a much larger Cepheid sample than is used in this work. As a first test both the slope and zero-point of the fits were allowed to vary. The two slopes had the same value as each other, as expected, but again the two zero-points were different. To bring the uncertainty on the zero-points down the slope was fixed and the zero-points refitted. The resulting fit is shown in Figure 3.17. Using the fixed slopes gives zero-points of  $21.90 \pm 0.02$  and  $22.03 \pm 0.04$  for the inner and outer fields respectively, very similar to the original values.

The fact that the zero-points are still discrepant when a fixed period range is used demonstrates that this effect, whatever the cause, is universal over the period range and is not due to the possible non-linearity of the PL relation.

## 3.7 Metallicity effects

As we have successfully ruled out blending and the period distribution as causes of the discrepant distance modulus the only remaining explanation is the differing chemical abundances in the two environments. Many attempts have been made to assess the extent of the metallicity effect, with some analysing the effect of  $Z$  on  $\mu$ , and hence the PL zero-point, such as Bono et al. (2008) and Sakai et al. (2004), whilst others focus on the effect that  $Z$  has on the slope of the PL relation (e.g. Alibert et al. (1999)). In this work, the effect of  $Z$  on the measured distance modulus is quantified by the parameter  $\gamma$ :

$$\gamma = \frac{\delta(m - M)_0}{\delta \log Z} \quad (3.14)$$

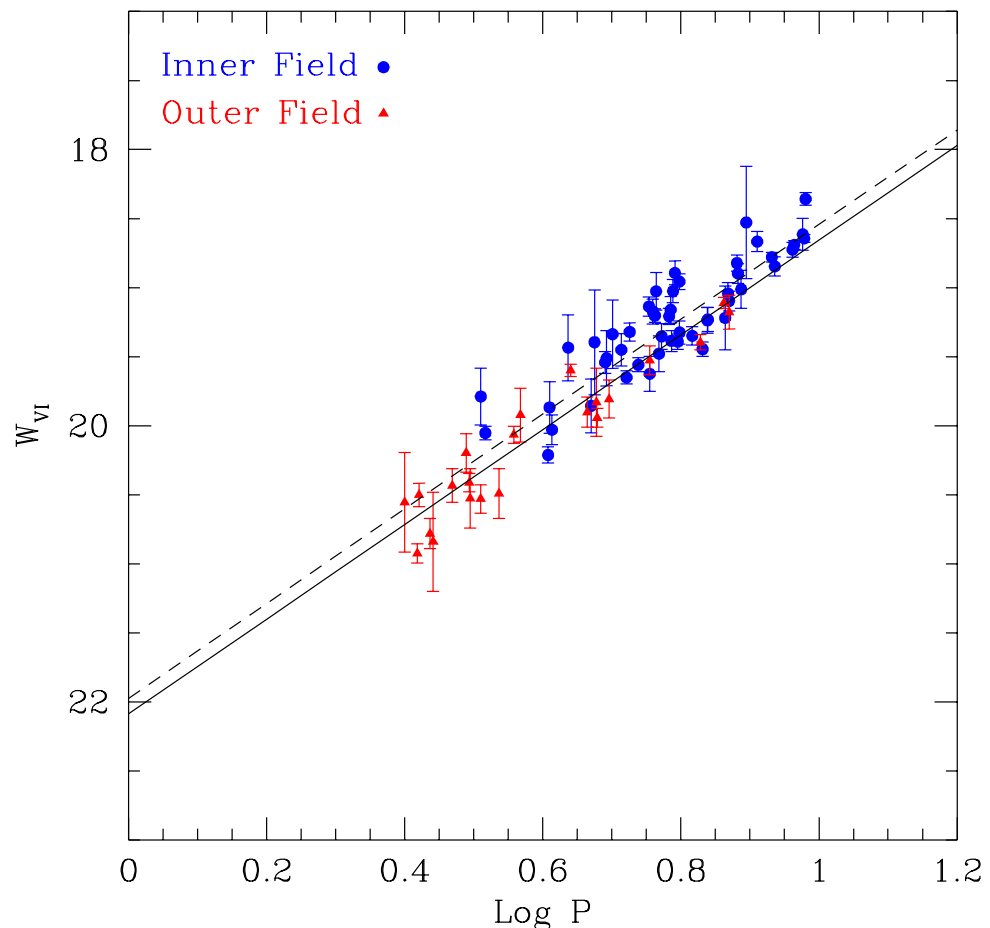


Figure 3.17:  $W_{vi}$  PL relation fit using  $\log P < 1$  criteria. The two slopes were found to be identical, however the zero-points still differ at the  $3\sigma$  level.

where  $\delta(m - M)_0$  is the difference between distance modulus corrected for the metallicity effect and without correction, in the sense corrected – apparent, and  $\delta \log Z$  is the difference between a reference metallicity and the region being studied (Kennicutt et al., 1998). Recent measurements of  $\gamma$  have produced negative values as large as  $\gamma = -0.4 \text{ mag dex}^{-1}$ , with the average being around  $\gamma = -0.25 \text{ mag dex}^{-1}$ . Following the methodology of Kennicutt et al. (1998) and Sakai et al. (2004) the value of  $\gamma$  can be calculated using the two distance moduli,  $\mu_{inner}$  and  $\mu_{outer}$ , and the oxygen abundance gradient of M33. We adopt the recent [O/H] gradient from Magrini et al. (2007):

$$[O/H] = -0.19(\pm 0.08)R + 8.95(\pm 0.13) \quad (R < 3 \text{ kpc}) \quad (3.15)$$

$$[O/H] = -0.038(\pm 0.015)R + 8.49(\pm 0.08) \quad (R \geq 3 \text{ kpc}). \quad (3.16)$$

It is also assumed that the metal *mixture* does not vary across the galaxy, therefore [O/H] can be taken as a proxy for  $Z$ .

The mean deprojected radial distances of the Cepheid samples are 1.2 kpc and 5.3 kpc, leading to  $12 + \log(O/H) = 8.722$  and 8.289 for the inner and outer fields respectively, giving a value of  $\Delta[O/H] = -0.433$ . To realise the full extent of the correction, we must initially treat the fields as if they had the same metallicity. This is done by using the same model PL relations for both regions.

We can substitute  $\delta(m - M)_0$  for  $\Delta\mu$ , which is equal to the offset in zero-points of the two PL relations, i.e.  $0.16 \pm 0.04$  mag, using the full sample distance moduli, and  $\delta Z = -0.433 \pm 0.101$  dex. This leads to a metallicity correction of  $\gamma = -0.37 \pm 0.09 \text{ mag dex}^{-1}$ . This is compatible with recent measurements, such as that of Sakai et al. (2004). Our final distance measurement for M33 is calculated by assuming an LMC metallicity of 8.34 (Sakai et al., 2004). Using  $\gamma = -0.37 \pm 0.09$  we find that the metallicity corrected distance modulus to M33 is  $\mu_\gamma = 24.52 \pm 0.09$ .

At the present time, there is still some debate over the true distance modulus of M33, with the value measured appearing to depend on the distance indicator used; obviously a far from ideal situation. Cepheid measurements tend to sit at the low end of the range, such as  $\mu = 24.52 \pm 0.14_{rand} \pm 0.13_{sys}$  (Lee et al., 2002). A larger distance was found

using a detached eclipsing binary, Bonanos et al. (2006) measured a distance modulus of  $24.92 \pm 0.12$  mag. Tip of the red giant branch measurements tend to sit between the two, the most recent example being U et al. (2009), who found the distance modulus of their outer disk field to be  $24.82^{+0.10}_{-0.06}$  mag.

The result presented here agrees with other Cepheid measurements, as well as the maser distance of  $800 \pm 180$  kpc (Argon et al., 2004), which corresponds to a distance modulus of 24.52 mag<sup>4</sup>. In their recent work, U et al. (2009) discussed how different reddening values (as well as different assumed LMC distance moduli) may affect the distance scale. They noted that Cepheid measurements tend to adopt higher reddening values than other methods, such as the tip of the red giant branch technique, which could lead to the shortening of Cepheid distances. However, in this work, this is not believed to be the case. The reddening values adopted in this work are compatible with those derived by U et al.. Additionally, the Wesenheit index was used to derive the final distance moduli. The Wesenheit index only makes assumptions about the reddening *law*, not the amount of material. Although different reddening laws are adopted in this work and U et al. ( $R = 3.23$  vs.  $R = 3.1$ ), the difference in the Wesenheit index is not large enough to explain the 0.3 mag difference in  $\mu$ .

The metallicity gradient contributes a large amount to the error budget for  $\gamma$ . The uncertainty on the gradient from Magrini et al. is particularly large as a two component fit is used. It is therefore useful to compare the value of  $\gamma$  arising from different metallicity gradients.

### 3.7.1 Effect of chosen metallicity gradient on $\gamma$

In recent years there has been some debate over whether M33 displays a steep or shallow metallicity gradient. The two-component gradient from Magrini et al. goes

---

<sup>4</sup>It should be noted that the maser distance has a much larger uncertainty than other measurements, and is therefore not an ideal reference measurement. However, measurements based on masers are purely geometrical, and, provided that the uncertainties can be contained, should provide a highly accurate distance measurement independent of the reddening and metallicity effects that Cepheids are subject to.

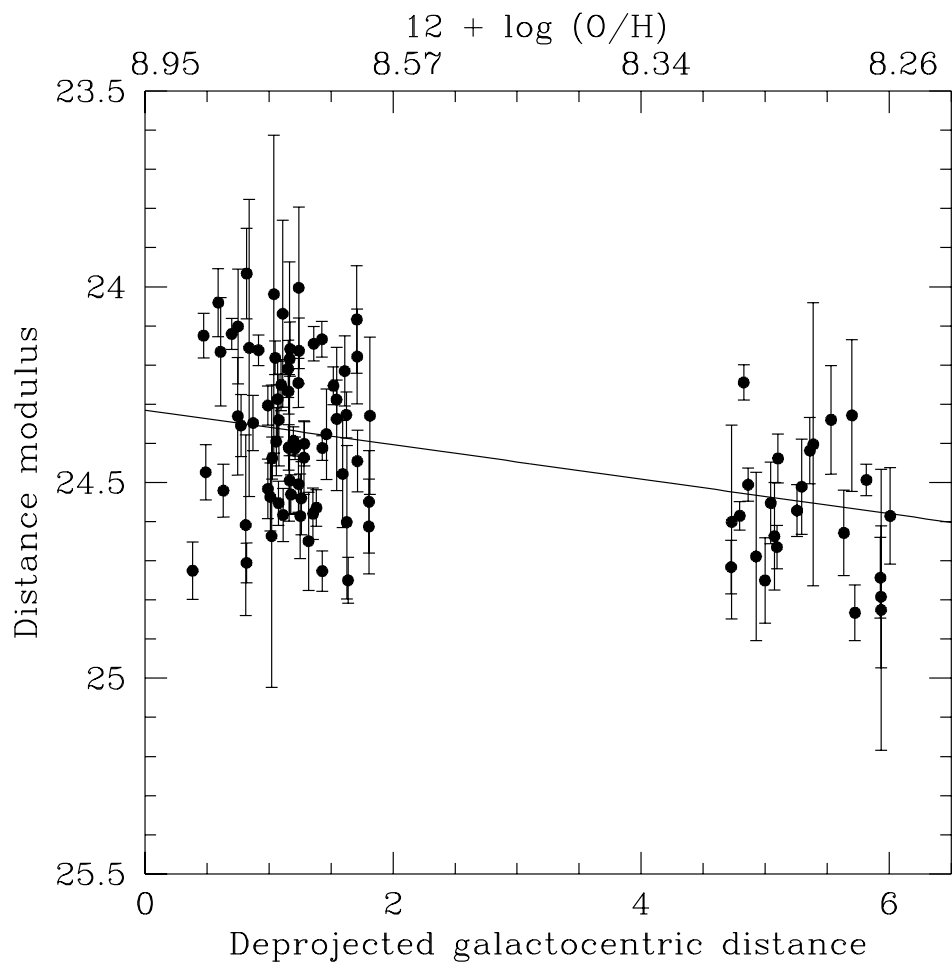


Figure 3.18: Measured distance moduli for each Cepheid as a function of deprojected galactocentric distance and metallicity. The line is a weighted least squares fit to the individual data points.

some way to solving the issue; it demonstrates that a shallow gradient will be found if the central region of M33 is excluded from the analysis. However, including the innermost regions, in their case from a compilation of metallicity measurements from young stars, in addition to HII regions, will produce a steeper gradient. The issue with this result is its uncertainty. Using a two component fit means that the uncertainty on  $\Delta \log Z$  for two fields taken from different fits is larger than if they are both taken from the same part. To investigate this, the effect of different metallicity gradients on  $\gamma$  is examined.

To assess the suitability of a steep metallicity gradient in M33, the result from Zaritsky et al. (1994) is used. They found  $\frac{d \log Z}{dR} = -0.127 \pm 0.011 \text{ dex kpc}^{-1}$  using 29 HII regions. This result is comparable to the average of the two gradients found in Magrini et al.. Using this gradient gives  $\Delta Z = -0.52 \pm 0.05 \text{ dex}$ , and  $\gamma = -0.31 \pm 0.07 \text{ mag dex}^{-1}$ , which is compatible with the original result.

Other recent measurements M33's metallicity imply a much shallower change. Crockett et al. (2006), for example, find  $\frac{d \log Z}{dR} = -0.012 \pm 0.011 \text{ dex kpc}^{-1}$ , this time from spectroscopic observations of 13 HII regions. Using this gradient,  $\Delta \log Z = -0.049 \pm 0.045 \text{ dex}$ , and  $\gamma = -3.25 \pm 3.09 \text{ dex kpc}^{-1}$ . In this case  $\gamma$  is much higher than in previous studies; such a large value of  $\gamma$  would have dramatic effects on the distance scale. In particular, it would change the distance to the LMC by so much that the Cepheid distances would become incompatible with all other measurements.

Although this could be taken to imply that the shallow metallicity gradient is incorrect, this is most certainly not the case. Firstly, recent measurements of 61 HII regions by Rosolowsky & Simon (2008) also give a shallow gradient, as do the planetary nebular abundance measurements by Magrini et al. (2009). Perhaps the most significant result from Rosolowsky & Simon (2008) was not that the metallicity gradient was shallow, but that the average scatter at any given radius was 0.11 dex, which is much larger than the measured gradient.

Figure 3.19 compares the [O/H] gradients of Zaritsky et al., and Crockett et al. with the data from Magrini et al. It is clear from this plot, that any one of the gradients can be

offset to match with certain parts of the data, and with the large scatter in individual HII region [O/H] values, as reported by Rosolowsky & Simon, this is no surprise. To quote Kudritzki et al. (2008), “...the expectation of homogeneous azimuthal metallicity in patchy star-forming spiral galaxies seems naive...”. One way to account this problem is to use the measurements of the HII regions nearest to the fields. Using the six closest regions to the inner field, the weighted average [O/H] is found to be  $8.35 \pm 0.08$ , with an rms scatter of 0.19, with the five closest regions to the outer field giving [O/H] =  $8.30 \pm 0.06$ , with an rms scatter of 0.13. Using these values gives a metallicity difference of  $0.05 \pm 0.10$ , corresponding to an unmeasurable difference.

A possible flaw in this analysis is that the metallicity gradients described above measure abundances from HII regions, hence are measures of the gas-phase metallicity. An improvement would be to use a metallicity gradient found from stars; after all,  $\gamma$  is measuring the effect of changing [O/H] on a *star’s* magnitude. This issue was addressed recently by U et al. (2009), who measured  $Z$  for a sample of 22 blue supergiants. In their figure 15, metallicity is plotted as a function of angular galactocentric distance for both the supergiant sample and the HII regions in Rosolowsky & Simon (2008). At large radii the two samples coincide, but towards the centre of the galaxy the stars are found to have significantly higher  $Z$  than the gas-phase measurements. It is possible that it is the different nature of the objects that causes the metallicity difference to be apparent in stars (showing up as a difference in  $\mu$  in Cepheids), but not in the HII regions.

Considering the uncertainties currently present in the abundance gradient of M33, it may seem incorrect to interpret the change in measured distance modulus as a metallicity effect. However, the difference in  $\mu$  between the two fields is significant, and a metallicity difference currently seems to be the only plausible argument to explain the change. Until direct measurements of [O/H] of the Cepheids that we are observing are available, the value of  $\gamma$  will remain somewhat uncertain.

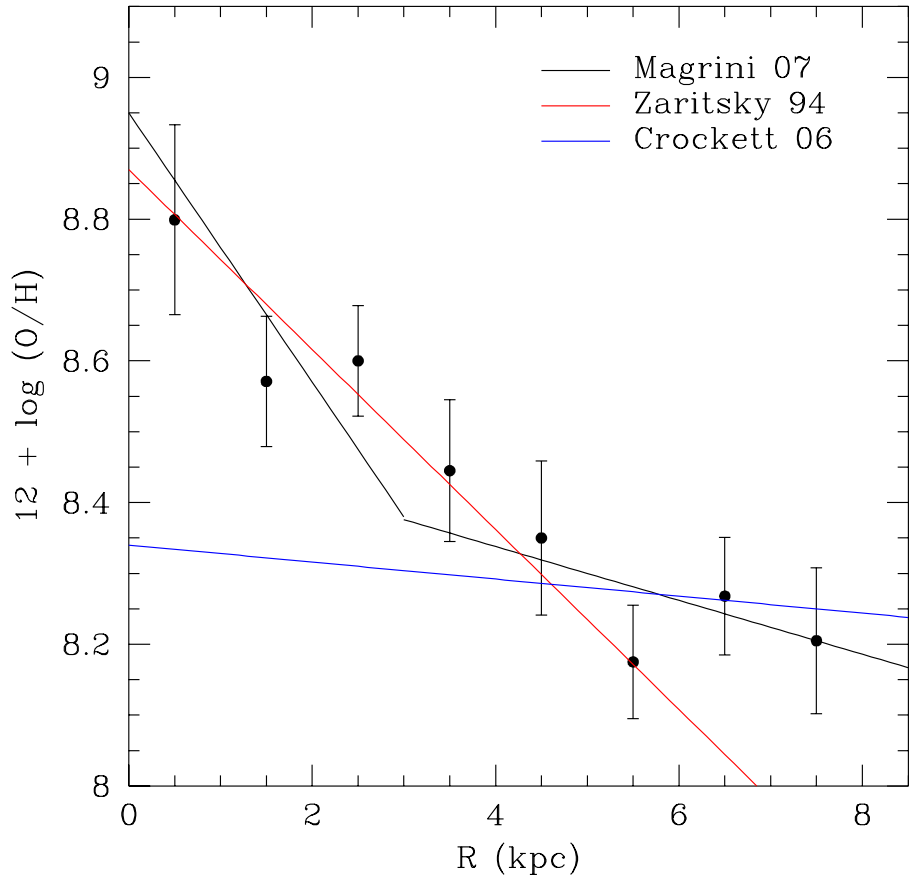


Figure 3.19: Comparison of metallicity gradients from Zaritsky et al., and Crockett et al. with the data from Magrini et al. The steep gradient is seen to match to the inner region of the galaxy, whilst the shallow gradient is consistent with the outer region. Both of the single-component fits have been offset to match with the Magrini et al. data points. This does not affect the result, as any zero-point terms will cancel out when determining the metallicity difference.

## 3.8 Conclusions

Using the reddening free Wesenheit LMC PL relation, distance moduli of the two regions have been calculated as  $\mu_{inner} = 24.37 \pm 0.02$  and  $\mu_{outer} = 24.54 \pm 0.03$ . The difference in these two distance moduli is interpreted as the effect of metallicity on the zero-point of the PL relation, and hence its effect on Cepheid distances. This effect is quantified by the parameter  $\gamma = \frac{\delta(m - M)_0}{\delta \log(O/H)} = -0.37 \pm 0.09 \text{ mag dex}^{-1}$ , consistent with other recent estimates. For the range of metallicities discussed here it is appropriate to include  $\gamma$  in the PL relation. This leads to the numerical PL shown in Equation 3.17, assuming an LMC distance modulus of 18.4 mag. The metallicity of the LMC is shown by  $\log(O/H)_{LMC}$ , the region in question is denoted by  $\log(O/H)$ .

$$\begin{aligned} W_{vi} = & -3.32(\pm 0.01) \log P + 22.01(\pm 0.03) \\ & + 0.37(\pm 0.09)(\log(O/H)_{LMC} - \log(O/H)) \quad (3.17) \end{aligned}$$

The analysis presented here assumes that *only* the zero-point of the PL relation changes with metallicity; the slope does not significantly change between the MW and LMC metallicities. Repeating the analysis using the MW slope of the  $W_{vi}$  PL relation from F07 ( $\frac{dW_{vi}}{d\log P} = -3.477$ ), compatible results are found, as shown in Table 3.12. Using the MW results,  $\gamma = -0.42 \pm 0.12 \text{ mag dex}^{-1}$ . This is an important result as it means that we can find reddening- and metallicity-corrected Cepheid distances for any population from two-colour ( $V$  and  $I_C$ ) photometry without calculating internal  $A_V$  values for other galaxies. It is also important to note the agreement between this work and the Hubble Key Project (Freedman et al., 2001); although the M33 Cepheids have shorter periods than the average in the HST project, the value of  $\gamma$  found here is consistent with their work.

As discussed in Section 3.7.1, a large contribution to the uncertainty in the result comes from the metallicity gradient. It is clear that more measurements are needed to confidently determine whether M33 exhibits a shallow or steep gradient, and there are two

Field	$z_{pLMC}$	$z_{pMW}$	$\mu_{LMC}$	$\mu_{MW}$
Inner	$21.85 \pm 0.02$	$21.91 \pm 0.03$	$24.37 \pm 0.02$	$24.32 \pm 0.08$
Outer	$22.01 \pm 0.03$	$22.09 \pm 0.06$	$24.53 \pm 0.03$	$24.51 \pm 0.10$

Table 3.12: Comparison of distances obtained using slopes from LMC and MW PL relations. An almost identical of  $\Delta\mu$  is found using the different slopes. The uncertainty on the MW slopes and zero-points are larger than for the LMC relations, hence the final uncertainty on  $\mu$  is increased.

main directions for this. The first is to follow the methodology of Magrini et al., compiling metallicity measurements from HII regions and stars to get a complete picture of the galaxy. The second is a more novel approach, first described by Beaulieu et al. (2006). By using the two periods of double-mode Cepheids, in combination with pulsation models, the metallicity of the Cepheid can be calculated. Their work used five double-mode Cepheids to calculate  $\frac{d\log Z}{dR} = -0.16 \text{ mag dex}^{-1}$ , consistent with the steep gradients. This work is currently being extended, using the INT to obtain periods for *every* double-mode Cepheid in the galaxy. This will allow the gradient to be measured from around 40 points, in a completely independent way from the HII regions method, providing a check on previous measurements. This is described in more detail in Chapter 6.

# Chapter 4

## CFHT MegaCam Survey

### 4.1 Introduction

This chapter describes the reduction and analysis of the data from the CFHT MegaCam survey of M33. It is similar to the WIYN survey described in Chapter 3, but on a much larger scale. Utilising the one square degree field of view of MegaCam, the survey covers the whole of the galaxy, as opposed to the two regions in the previous study. By covering such a large area, a much larger sample of Cepheids is obtained, allowing the analysis of the metallicity effect to be undertaken in much more detail. Figure 4.1 is a composite of three images (one each of  $g'$ ,  $r'$ ,  $i''$ ), demonstrating the enormous field of view of MegaCam. Compare this to Figure 3.1; the improvement on the WIYN survey is obvious.

The observations, reduction of the data and image subtraction were not performed as part of this work, but were published in Hartman et al. (2006) (hereafter known as H06). A summary of their work is given in Sections 4.2 to 4.5.

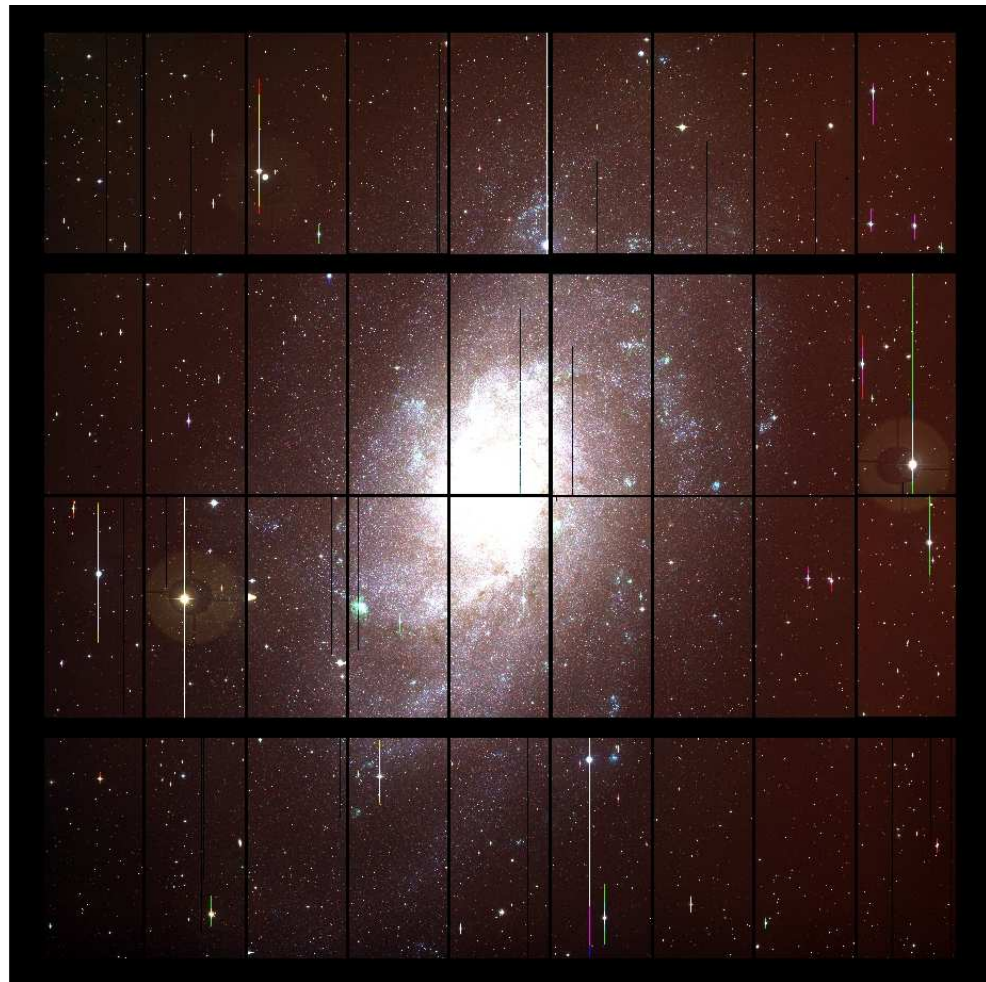


Figure 4.1: M33 image taken with MegaCam on CFHT. The image is a composite of three frames (one each of  $g'$ ,  $r'$ ,  $i'$ ). MegaCam has a field of view of one square degree, enabling the whole of M33 to be covered with one pointing.

Season	Filter	Exposure time
1	$g'$	530s
	$r'$	660s
	$i'$	660s
2	$g'$	480s
	$r'$	600s
	$i'$	600s

Table 4.1: Exposure times for CFHT observations. Season 1 covers 2003, season 2 covers 2004–2005.

### 4.1.1 Canada-France-Hawaii Telescope and MegaCam

The Canada-France-Hawaii telescope is a 3.6-m telescope situated on Mauna Kea in Hawaii. This study uses the one square degree imager, MegaCam, which is made of 36 CCDs, each with  $2048 \times 4162$  0.187 arcsec pixels. The observations were made in the Sloan-like  $g'$ ,  $r'$  and  $i'$  bands. These are optical filters, with central wavelengths of 4872, 6282 and 7776Å respectively.

## 4.2 Observations

Observations of M33 were taken in Queue Service Observing mode on 17 nights between August 2003 and January 2005. A total of 34  $g'$ , 33  $r'$  and 36  $i'$  band images were obtained over this time. A log of the observations can be found in table 1 of H06. The spacing of the observations was optimised to the detection of Cepheids with periods of 2 to 100 days. The exposure times for each filter and season are shown in Table 4.1.

## 4.3 Preliminary data reduction

The initial processing was performed as part of the Queue Service Observing mode, using the ELIXIR pipeline. This pipeline performs bias, dark, flat-field and fringe corrections, merges the amplifiers and provides an estimate of the photometric calibration.

Although the photometric calibration is provided in the image headers, it was decided that it may not be accurate enough for this work. MegaCam is thought to exhibit colour terms that change across the different CCDs, and these may not be adequately quantified by the pipeline. As a result, all magnitudes described in H06 are purely instrumental.

## 4.4 Image subtraction

Image subtraction is an extremely powerful technique for work in crowded fields, and is an excellent way of detecting and measuring variable objects. By matching an image and subtracting a reference image, any objects that have varied in brightness between the two epochs will show up clearly, with all constant objects removed. Light curves of the variable objects can be produced by performing PSF photometry on the subtracted images. Although this method will only produce photometry for the variable objects, using regular PSF photometry on such crowded images would not provide the high level of accuracy that is required for this project.

The first image subtraction work was performed by Tomaney & Crotts (1996), who applied the technique to microlensing surveys. Their method was to select the frame with the worst seeing as the reference image, and degrade other images to the same quality as this reference. Once the PSFs are matched, the reference can be subtracted from each image, with any changes showing up as positive or negative signals, depending on the direction of the flux change.

There are several reasons why this method is not ideal. Most obviously, all the images are degraded to the seeing of the worst. One might ask then, why bother taking images in good seeing if you intend to bring them down to the quality level of the poorest?

Secondly, the method derives the convolution kernel (the function that is used to degrade the images) from the ratio of the Fourier transform of a bright star on each image. The transforms contained high order terms that were dominated by noise, meaning that it could not be applied to the wings of the PSF. A Gaussian extrapolation had to be used

to model this region, and as was discussed in Chapter 2, a Gaussian is not always the best model for a star. Using this technique gives no guarantees about the quality of the subtracted image.

Alard & Lupton (1998) solved the problems with the development of the ISIS software. Rather than using the information from a single star to create the kernel, their technique used a least-squares technique, involving all the pixels in the images. This produced a kernel solution that could handle both PSF and sky variations across the image. The method was improved in Alard (2000), where the use of a spatially varying kernel was included.

#### 4.4.1 Image subtraction on the CFHT data

Image subtraction was performed on the CFHT data, treating each chip and filter separately. It is important that the data are split in this way; the individual CCDs have different properties, such as QE, read-noise and gain. A reference image was created using, on average, six of the best seeing images for each filter-chip combination. A transformation of the PSF, flux and background between the reference and the individual images was found using ISIS, and residual images are produced.

To detect variable objects, the residual images are divided by the square root of the original, then the absolute values of the pixels are co-added. This gives an image clearly showing the variables, with the flux of the point-sources proportional to the significance of the variability. Light curves were obtained by performing PSF photometry on the residual images.

The light curves produced using this method are not in standard magnitudes, but show differential flux variations. The conversion to magnitudes was done using DAOPHOT and ALLSTAR on the reference image, in much the same way as described in Chapter 2, followed by two aperture corrections. The first was done in the standard manner (see Section 2.8.1) to account for the flux in the wings of the profile missed by the PSF model; here the aperture size varied between images. The second correction was

determined from a fixed aperture of 13 pixels, to allow objects on different chips to be reasonably compared. Although the size of the PSF changes over the field of view, it typically varied by less than 2 pixels between the best and worst value for one exposure, and was much less than the 13 pixel aperture used here. Finally, the light curves were converted to magnitudes by matching the objects to the DAOPHOT PSF magnitude catalogue. The final variable source catalogue contains light curves for 26432, 30386 and 34320 objects in  $g'$ ,  $r'$  and  $i'$  respectively.

## 4.5 Cepheid Identification

The Cepheid variables were identified using their position in colour–magnitude diagrams. The location of the instability strip was found by plotting the fraction of stars with root–mean–square variations larger than 0.1 mag as a function of colour, for magnitudes ranging from 22.25 to 19.25. The strip was found at  $0 < (g' - r') < 1$  and  $0 < (r' - i') < 0.5$ . Of the 3580 objects in the Cepheid IS, 2327 were identified as true Cepheids. The periods were obtained by Fourier transforms of the light curves.

## 4.6 Calibration

As has already been mentioned, we decided against using the ELIXIR photometric solution to calibrate the data. Instead, an independent calibration solution has been produced, combining the CFHT data with observations taken with the Isaac Newton Telescope<sup>1</sup> (INT) Wide Field Camera (WFC) in October 2008. The calibration method is similar to that used for the WIYN Mini-Mosaic data.

---

<sup>1</sup>Based on observations made with the Isaac Newton Telescope operated on the island of La Palma by the Isaac Newton Group in the Spanish Observatorio del Roque de los Muchachos of the Instituto de Astrofísica de Canarias

Chip	Read Noise (ADU)	Gain ( $e^- \text{ADU}^{-1}$ )
1	6.4	2.8
2	6.9	3.0
3	5.5	2.5
4	5.8	2.9

Table 4.2: Read noise and gain of INT WFC chips

### 4.6.1 Isaac Newton Telescope and WFC

The Isaac Newton Telescope is a 2.5-m telescope at the Observatorio del Roque de los Muchachos, La Palma. The wide field camera consists of four  $2048 \times 4100$  pixel CCDs with a scale of  $0.333 \text{ arcsec pixel}^{-1}$ . Figure 4.2 shows the orientation of the chips. The read noise and gain of each chip are shown in Table 4.2.

### 4.6.2 INT observations

During the eight-night observing run, observations were taken of several Sloan Digital Sky Survey (SDSS) fields in the  $g'$ ,  $r'$ ,  $i'$  bands. Eight fields were chosen as targets, spaced by roughly 10 to 15 degrees in right ascension. Using the information from CMT<sup>2</sup>, four nights were found to be photometric. The night chosen to be the reference was 2008 October 7 as it had the best average seeing and the most complete sample of SDSS fields. A summary of the observations is given in Table 4.3. The pointings were randomly offset by multiples of 5 arcsec in RA and Dec to ensure that bad pixels would not affect any star disproportionately.

### 4.6.3 INT Data Reduction

Initial processing was performed by D. Bersier using the IRAF CCDPROC package. Bias and flat-field frames were created using stacks of 10 images. A master fringe frame was created using the  $i'$  band flat-field frames. Individual images were corrected by scaling the master frame to match the amplitude of the fringing.

---

<sup>2</sup>[www.ast.cam.ac.uk/~dwe/SRF/camc\\_extinction.html](http://www.ast.cam.ac.uk/~dwe/SRF/camc_extinction.html)

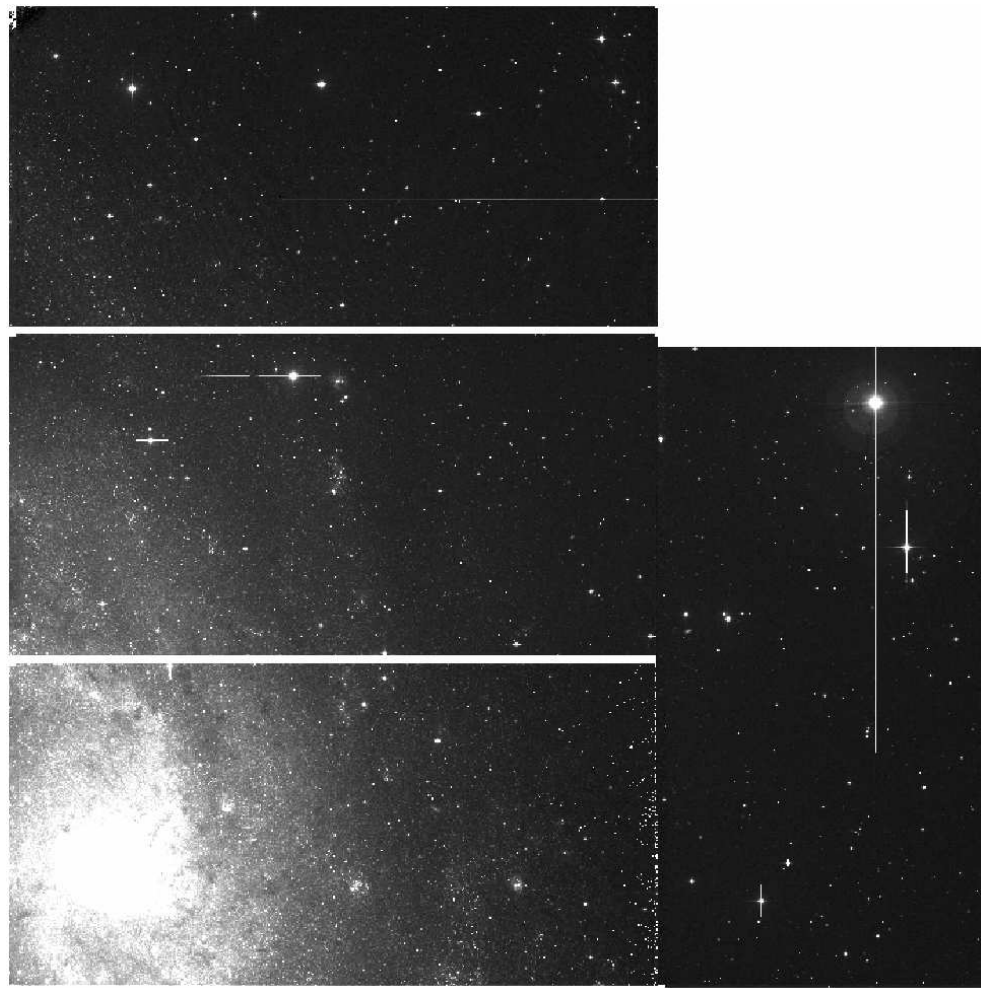


Figure 4.2: Orientation of the INT WFC chips. The image is made from single  $g'$ ,  $r'$ ,  $i''$  M33 NW frames. Chip numbers (Clockwise from right): 2,1,4,3.

Field	$\alpha$	$\delta$	$N_{g'}$	$N_{r'}$	$N_{i'}$	Average seeing
SDSS 10	$0^h40^m00^s$	$+01^\circ00'00''$	2	2	2	1.0''
SDSS 56	$3^h44^m00^s$	$00^\circ00'00''$	3	3	4	1.0''
SDSS 310	$20^h40^m00^s$	$00^\circ00'00''$	3	3	3	1.2''
SDSS 325	$21^h40^m00^s$	$-01^\circ00'00''$	1	1	1	1.3''
SDSS 340	$22^h20^m00^s$	$00^\circ00'00''$	1	1	1	1.3''
SDSS 350	$23^h20^m00^s$	$00^\circ00'00''$	4	5	4	1.2''
M33 NE	$1^h35^m17^s$	$30^\circ52'37''$	3	3	3	1.1''
M33 NW	$1^h33^m17^s$	$30^\circ52'37''$	2	2	2	1.0''
M33 SE	$1^h35^m17^s$	$30^\circ26'37''$	2	2	2	1.0''
M33 SW	$1^h33^m17^s$	$30^\circ26'37''$	2	2	2	0.9''

Table 4.3: INT observations on 2008 October 7. SDSS fields were observed approximately every hour. SDSS fields were observed with 60s exposures, M33 with 600s exposures.

PSF photometry was performed on the images using a modified version of the pipeline described in Chapter 2. Although the pipeline produced good results for the WIYN data, the changes produced slightly better PSF models. The modifications can be summarised as follows:

1. Two PSF star lists are made using PICK; one with 20 bright stars, the other with 180 fainter stars. The brighter stars are given higher weights by PSF. Combining these two lists ensures a better representation of the luminosity function of the image, producing a more accurate model.
2. Neighbour stars are removed from the image between every iteration of the PSF model.
3. The order of variability of the model is increased after every convergence. The initial value is set to  $-1$ , which corresponds to a purely analytical model. Once this model has converged, the order is increased to 0; a spatially constant model. This is iterated again to linearly and quadratically varying models once a good fit is obtained.

The DAOPHOT, PHOT and ALLSTAR parameters were also changed; their new values are shown in Table 4.4. Aperture corrections were obtained using the methods described in Section 2.8.1; in this case the aperture sizes ranged from 4 to 40 pixels, with the sky measured from the 40 to 50 pixel annulus. The final instrumental step was to correct the magnitudes for exposure time.

#### 4.6.4 SDSS Calibration

Catalogues of the objects in the observed SDSS fields were downloaded from the SDSS website<sup>3</sup> (Abazajian et al., 2009). A rough astrometric transformation was created using CCTRAN in IRAF to convert the RA and Dec values into pixel coordinates. The catalogue was matched to the INT photometry using DAOMATCH and DAOMASTER.

---

<sup>3</sup><http://www.sdss.org/dr7/>

Package	Parameter	Value
DAOPHOT	FWHM	4 pixels
	PSF radius	15 pixels
	Fitting radius	5 pixels
	High good data threshold	60000 counts
	Low good data threshold	$20\sigma$
	Detection threshold	$4\text{--}6\sigma$
	Order of PSF variability	-1, 0, 1, 2
PHOT	Analytic PSF model	-6
	Aperture	4 pixels
	Inner sky	16 pixels
ALLSTAR	Outer sky	32 pixels
	Fitting radius	4 pixels
	Inner sky	16 pixels
	Outer sky	32 pixels

Table 4.4: Parameters for the INT photometry. The detection threshold was changed for particularly crowded frames. The order of variability was increased throughout the process. Parameters not shown were left at their default values.

Each INT chip was treated separately, resulting in four standard solutions. The solutions take the form

$$m_{inst} = m_{cal} + a + b \times X_M + c \times Colour + d \times UT \quad (4.1)$$

which is the same form as the WIYN solution in Section 3.3.1. The solutions, found using FITPARAMS, are given in Table 4.5.

Once again, a  $UT$  term has been included in the solution, and it is extremely small. This was done mainly to check that the extinction did not change significantly through the night. Also, the airmass coefficients ( $b$ ) change slightly between the chips. In theory these should be constant for each chip, but there is no way to do this simply in IRAF. The effect on the result was tested by fitting the solution with a fixed airmass term for each chip, and the results were consistent with the original method. Therefore, the values were left at those shown in Table 4.5.

The RMS values are slightly higher than the WIYN Landolt fit (see Table 3.2). In the Landolt case the fields were sparse; as there was no chance of crowding affecting the photometry, aperture photometry was used to construct the solution. The SDSS fields,

Filter	<i>a</i>	<i>b</i>	<i>c</i>	<i>d</i>	RMS
<b>Chip 1</b>					
<i>g'</i>	-0.9968	0.1781	-0.1391	0.0002	0.0213
<i>r'</i>	-0.6327	0.0993	-0.0005	-0.0003	0.0259
<i>i'</i>	-0.1889	0.0696	-0.0579	-0.0003	0.0255
<b>Chip 2</b>					
<i>g'</i>	-0.6724	0.1618	-0.1299	0.0005	0.0224
<i>r'</i>	-0.3393	0.1159	0.0026	0.0000	0.0220
<i>i'</i>	0.1512	0.0522	-0.0611	0.0002	0.0212
<b>Chip 3</b>					
<i>g'</i>	-0.9183	0.1760	-0.1353	-0.0005	0.0408
<i>r'</i>	-0.6797	0.1137	0.0000	-0.0004	0.0210
<i>i'</i>	-0.2312	0.0442	-0.0825	0.0009	0.0190
<b>Chip 4</b>					
<i>g'</i>	-0.7713	0.1684	-0.1361	0.0002	0.0207
<i>r'</i>	-0.4645	0.0972	0.0046	0.0002	0.0236
<i>i'</i>	-0.0544	0.0488	-0.0627	0.0007	0.0238

Table 4.5: Standard solution for INT SDSS observations.

whilst not as crowded as some of the regions in M33, contain a much larger number of stars. Whilst the photometry itself is sound, there will be some scatter introduced into the solution from the intrinsic limit on the accuracy of the PSF model.

The standard calibration was then applied to the best seeing M33 frames taken on that night.

#### 4.6.5 Standard Calibration of the CFHT data

To apply the standard solution to the CFHT catalogues, the master photometry catalogue was used (Bersier, private communication)<sup>4</sup> The catalogue contains instrumental magnitudes for over 4 million objects, as measured on the reference frame. This was used to produce a standard solution by taking advantage of the fact that the vast majority of the objects *do not* vary in brightness.

Using the same method as for the Mini-Mosaic calibration, (see Section 3.3.1), the

---

<sup>4</sup>The master catalogue, produced by J. Hartmann, is not available as part of the on-line data, but was kindly provided for use in this project.

catalogue was matched to the INT M33 data. Each CFHT chip was treated separately, and in the case that two or more INT frames overlapped with the chip, the one that covered the largest area was chosen.

In this case the form of the standard solution was changed, absorbing the airmass and UT terms into the zero-point, and bringing in a quadratic colour term:

$$m_{CFHT} = m_{INT} + a + b \times \text{Colour} + c \times (\text{Colour})^2 \quad (4.2)$$

where  $m_{CFHT}$  is the CFHT instrumental magnitude and  $m_{INT}$  is the calibrated INT magnitude. Note that not all of the CFHT chips were calibrated. Some chips near the edges of the field of view did not contain Cepheids so have not been calibrated at this time. Due to the large number of chips, the coefficients are given in Appendix A.

The Cepheids were calibrated by applying the corresponding chip solution to the flux averaged magnitudes given in the H06 variable catalogue. These magnitudes are on the same system as the reference magnitudes used to create the solutions, but are flux-averaged over the whole light curve, rather than single-epoch reference frame magnitudes. The reference frame magnitudes would be inappropriate; although each object is measured at the same time, they are not taken at the same *phase*, and the dispersion in the resulting PL relation would be increased.

## 4.7 Cepheid PL relations in Sloan bands

In the previous Chapter, the fact that the PL relations had already been calibrated in  $B, V, I$  and  $W_{vi}$  made life much simpler. By using the well-calibrated slopes and zero-points of Fouqué et al. (2007), we could be sure that any difference in the PL zero-point was not due to an erroneous calibration of the PL relation itself.

Until now, a purely observational calibration of the PL relation in the Sloan bands was yet to be completed. Ngeow & Kanbur (2007) started to tackle the issue using a semi-empirical approach. Using the OGLE  $B, V, I$  observational PL relations, in

Filter	$a$	$b$	$\sigma$
$g'$	$-2.518 \pm 0.036$	$17.165 \pm 0.027$	0.262
$r'$	$-2.819 \pm 0.027$	$17.027 \pm 0.020$	0.193
$i'$	$-2.928 \pm 0.023$	$17.032 \pm 0.018$	0.171

Table 4.6: Semi-empirical Sloan PL relations from Ngeow & Kanbur (2007). Column 4 ( $\sigma$ ) is the dispersion of the relation.

combination with theoretical bolometric corrections from the Padova group (Girardi et al., 2002, 2004), they converted the calibrated Johnson–Cousins PL relations to the Sloan system. The relations take the form

$$M = a \log P + b, \quad (4.3)$$

and the coefficients for each band are given in Table 4.6.

As Ngeow & Kanbur themselves state, there may be issues with the transformations, leading to systematic errors in the PL relations. To assess the robustness of their work they compare the PL relations with those obtained using photometric transformations to the Sloan system (Jester et al., 2005). Although they obtain compatible results, both Ngeow & Kanbur and Jester et al. note that the transformations may not be applicable to all stars, and separate transformations may be necessary for different spectral types. This implies that they may not be entirely suitable for Cepheids, although they appear to at least give a reasonable estimate.

To resolve this problem, rather than use the published PL relations, both the slope and zero-points of the M33 PL relations will be derived, providing an observational calibration that can be applied to any galaxy.

### 4.7.1 Cepheid Selection

Although the Cepheids had already been identified in the original H06 study, some selection is still required to ensure clean PL relations.

1. Amplitude relation:  $A_g > A_r > A_i$ .

2. Flux averaged magnitudes must be available.
3. Must be flagged as variables in all filters.
4. Must have Fourier analysis<sup>5</sup> available.

The amplitude selection removes possible blends from the sample. The flux–average requirement makes sure that the magnitudes are comparable. Some objects do not have flux averaged magnitudes — only reference magnitudes. This would increase the dispersion in the PL relation and could bias any fits. Unfortunately these values were not available for chip 23. It is believed that the crowding made the PSF photometry very difficult here as it covers the very center of the galaxy. The Fourier analysis requirement ensures that only fundamental Cepheids are used, as these were identified using the Fourier parameters.

### 4.7.2 Reddening Corrections

Before the PL relations can be calibrated we must correct for extinction effects. Estimates of the extinction coefficients  $A_{g'}$ ,  $A_{r'}$  and  $A_{i'}$  can be found using the reddening law of Cardelli et al. (1989). Assuming  $R = 3.23$ , the ratios of the coefficients with  $A_V$  are found to be

$$\frac{A_{g'}}{A_V} = 1.18640, \quad (4.4)$$

$$\frac{A_{r'}}{A_V} = 0.87364, \quad (4.5)$$

$$\frac{A_{i'}}{A_V} = 0.65864. \quad (4.6)$$

Using these ratios in combination with the outer field  $E(B - V)$  value in Table 3.8, the extinction terms in the Sloan bands are found to be  $A_{g'} = 0.376$ ,  $A_{r'} = 0.277$  and  $A_{i'} = 0.209$ , with an uncertainty of 0.030 on each value coming from the fit in Figure 3.14.

---

<sup>5</sup>The Fourier analysis of the light curves was performed by J.-B. Marquette separately to this work.

Filter	$a$	$b$	$\sigma$
$g'$	$-2.410 \pm 0.080$	$23.294 \pm 0.063$	0.267
$r'$	$-2.724 \pm 0.067$	$23.108 \pm 0.053$	0.225
$i'$	$-2.841 \pm 0.056$	$23.010 \pm 0.044$	0.185

Table 4.7: Sloan band PL relations for the  $Z_{LMC}$  sample. The form of the PL relation is given in Equation 4.3,  $\sigma$  is the dispersion.

These values will only applicable to the area corresponding with the outer field of the WIYN survey as the amount of dust is already known to vary across the galaxy (see Tables 3.8 and 3.9 — both  $E(B - V)$  and  $E(V - I)$  change between the two fields.).

The main result from the WIYN survey was that the zero-point of the standard  $B, V, I$  and the Wesenheit PL relations changes with metallicity, but the slope for each is believed to be constant. Ideally, the slope would be measured using the entire sample; in practice however, things are not as simple. Figure 4.3 shows the how the distribution of periods changes with metallicity. A trend of increasing period with increasing metallicity is clear, meaning that if the population was considered as a whole, the PL relation would not have a homogeneous metallicity sampling. The short period end would be dominated by metal-poor Cepheids, with the long period Cepheids being mainly high metallicity. The signature of the mixed sample would not be immediately obvious. As the metallicity change is continuous, the change would not present as several offset PL relations, but instead as a steeper measured slope.

To counteract this effect, only the Cepheids with  $Z = Z_{LMC}$  are used.  $Z_{LMC}$  is taken as 8.34 (Sakai et al., 2004), with a range of  $\pm 0.05$ , leaving a sample of 243 stars. The slope and zero-point of the sample are found using the weighted-least-squares algorithm developed by Akritas & Bershady (1996). Their method takes into account the intrinsic scatter of the PL relation, which was deemed to be a more robust method than an ordinary least-squares fit. The fits are shown in Figure 4.4, and summarised in Table 4.7.

The slopes of the PL relation can now be used to correct for reddening and calibrate the PL relations. By pulling out Cepheids with  $4.7 \leq R \text{ kpc} \leq 5.3$ , corresponding to the WIYN outer field, the zero-point can be found using the  $Z_{LMC}$  slope. In this process

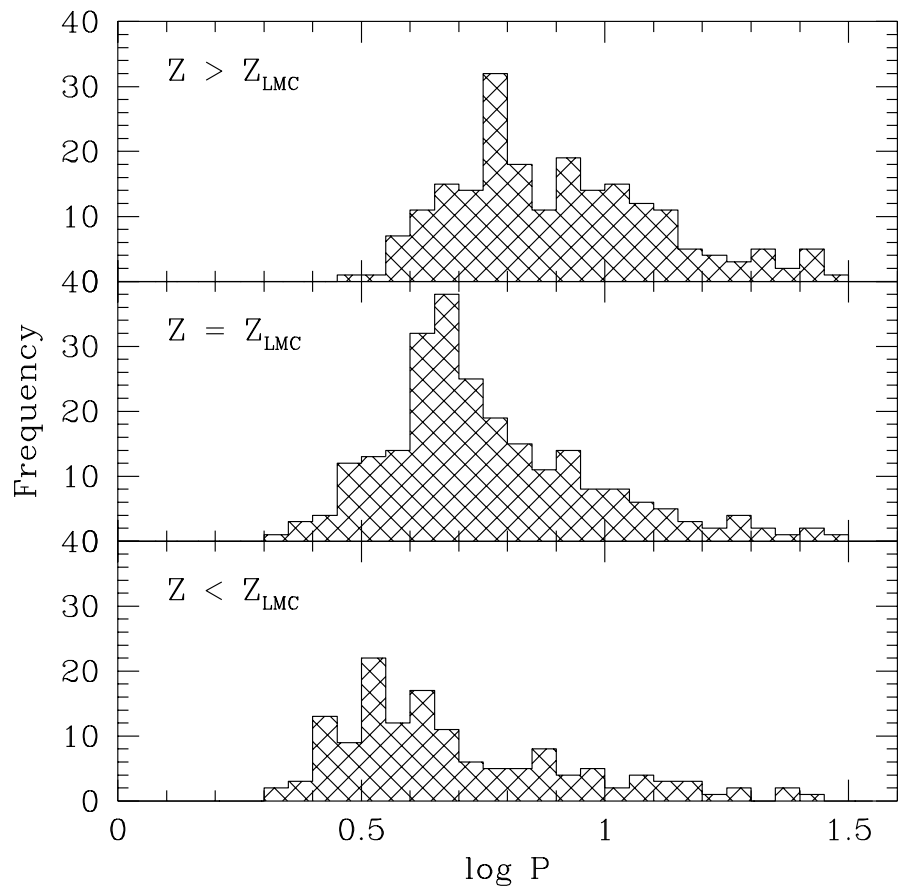


Figure 4.3: Period distributions of CFHT Cepheids at different metallicities. The three panels represent high metallicity ( $Z > 8.39$ , top), LMC metallicity ( $8.29 \leq Z \leq 8.39$ , middle) and low metallicity ( $Z < 8.29$ , bottom) samples. The peak of the distribution shifts to higher periods as metallicity is increased.

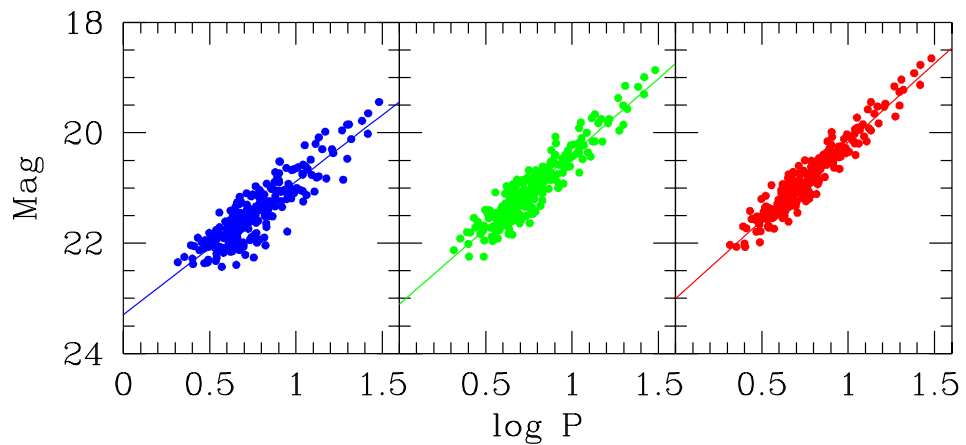


Figure 4.4: Sloan band PL relations for the  $Z_{LMC}$  sample.  $g', r', i'$  go from left to right.

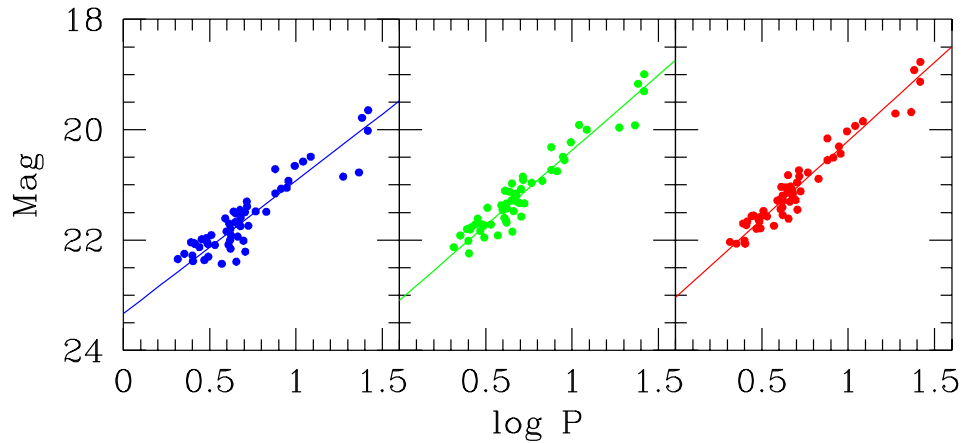


Figure 4.5: Outer field PL relations.  $g'r'i'$  go from left to right. The lines are weighted least-squares fits, with the slopes fixed to the values in Table 4.7. The magnitudes have not been corrected for reddening.

the assumption is made that the dust in M33 exhibits a symmetric radial profile, hence so do  $E(g' - r')$  and  $E(r' - i')$ . This may not be the case, but it is the most reasonable conclusion from the information that is available. Using this range in radius gives a sample of 56, with a metallicity spread of  $0.0228 \text{ dex}^6$  — a sufficiently small range to ensure that the fit will be unaffected by changes in  $Z$ .

The final calibrated relation takes the form

$$M = a \log P + b - A_X = a \log P + b_{\text{dered}} \quad (4.7)$$

where  $A_X$  is the extinction for the band in question, and  $b_{\text{dered}}$  is the dereddened zero-points. The uncorrected fits are shown in Figure 4.5, with the coefficients of Equation 4.7 given in Table 4.8. The absolute zero-points of the relations can be found by assuming a distance modulus of M33 of  $24.54 \pm 0.03$  — the value that was found in the WIYN survey for the outer field.

---

<sup>6</sup>Assuming the two-component metallicity gradient of Magrini et al. (2007).

Filter	$a$	$b$	$A_X$	$b_{dered}$	$b_{abs}$
$g'$	$-2.41 \pm 0.08$	$23.33 \pm 0.04$	$0.38 \pm 0.03$	$22.96 \pm 0.05$	$-1.58 \pm 0.06$
$r'$	$-2.72 \pm 0.07$	$23.10 \pm 0.03$	$0.28 \pm 0.03$	$22.82 \pm 0.04$	$-1.72 \pm 0.05$
$i'$	$-2.84 \pm 0.06$	$23.04 \pm 0.03$	$0.21 \pm 0.03$	$22.83 \pm 0.04$	$-1.71 \pm 0.05$

Table 4.8: Dereddened PL relations from the outer field. The slopes were fixed to the  $a$  values, and  $b$  was found from a weighted least squares fit. The dereddened zero-points ( $b_{dered}$ ) were found using the extinction values ( $A_X$ ).

## 4.8 Sloan Wesenheit Indices

The relations in Table 4.8 are calibrated to a metallicity of  $12 + \log(O/H) = 8.30 \pm 0.023$  dex. They can be extended to any metallicity using the  $\gamma$  parameter. The value of  $\gamma$  found in the previous chapter is only applicable to the  $VI$  Wesenheit PL relation; it has different values for different wavebands. With the recent shift towards the Sloan photometric system, it seems a worthwhile exercise to determine  $\gamma$  for this regime.

The most robust way to find  $\gamma$ , and to measure Cepheid distances in general, is to use the Wesenheit index. Although the previous section provides a reddening correction, it is only appropriate for the radial distance range from which it was derived. The same method could be applied to the inner field but there is not enough information to cover the region between the two.

The Sloan-band Wesenheit indices are constructed in the standard way using the  $R = 3.23$  reddening law, but this time substituting in the relations between  $A_{g'}$ ,  $A_{r'}$  and  $A_{i'}$ , such that

$$W_{gi} = g' - 2.248(g' - i'), \quad (4.8)$$

$$W_{ri} = r' - 4.064(r' - i'). \quad (4.9)$$

The PL relations for the  $Z_{LMC}$  sample are fitted using the Akritas & Bershadsky weighted least-squares algorithm, giving the results

$$W_{gi} = -3.377(\pm 0.058) \log P + 22.655(\pm 0.046) \quad (4.10)$$

and

$$W_{ri} = -3.323(\pm 0.083) \log P + 22.672(\pm 0.065), \quad (4.11)$$

with the relations shown in Figure 4.6. In the same manner as before, the slopes are considered constant for all metallicities but the zero-points are expected to change.

At this point it is appropriate to make a comparison between the observational result and the semi-empirical models. Although Ngeow & Kanbur (2007) do not explicitly give the Wesenheit PL relations, they can be predicted by combining the coefficients in Table 4.6 with Equations 4.8 and 4.9:

$$W_{gi} = -3.439(\pm 0.053) \log P + 16.866(\pm 0.040), \quad (4.12)$$

$$W_{ri} = -3.262(\pm 0.066) \log P + 17.047(\pm 0.050). \quad (4.13)$$

Although the slopes derived here are not the same as in the empirical version, they are consistent within the errors. The zero-points are not expected to be the same, as Ngeow & Kanbur are using LMC Cepheids, but it is reassuring to see that the difference between the two is in the same direction.

### 4.8.1 Metallicity effects

Evidence for the zero-point change is shown in Figure 4.7. The black lines represent the  $Z_{LMC}$  PL relations, with the colours representing different radial distances. The Cepheids with higher metallicities (smaller radial distances) tend to lie above the line, with the low metallicity ones falling below the line. The effect is more pronounced in the  $W_{ri}$  panel, as the larger colour coefficient of  $W_{ri}$  produces more scatter. The trends can be seen more clearly by plotting histograms of the deviations from the fit. This is shown in Figure 4.8. The median value shifts from a positive value at  $Z > Z_{LMC}$  to negative at  $Z < Z_{LMC}$ .

The final step is to calculate  $\gamma$ . In Chapter 3,  $\gamma$  was found by taking the difference in distance modulus of the two fields. This sample has a continuous distribution of

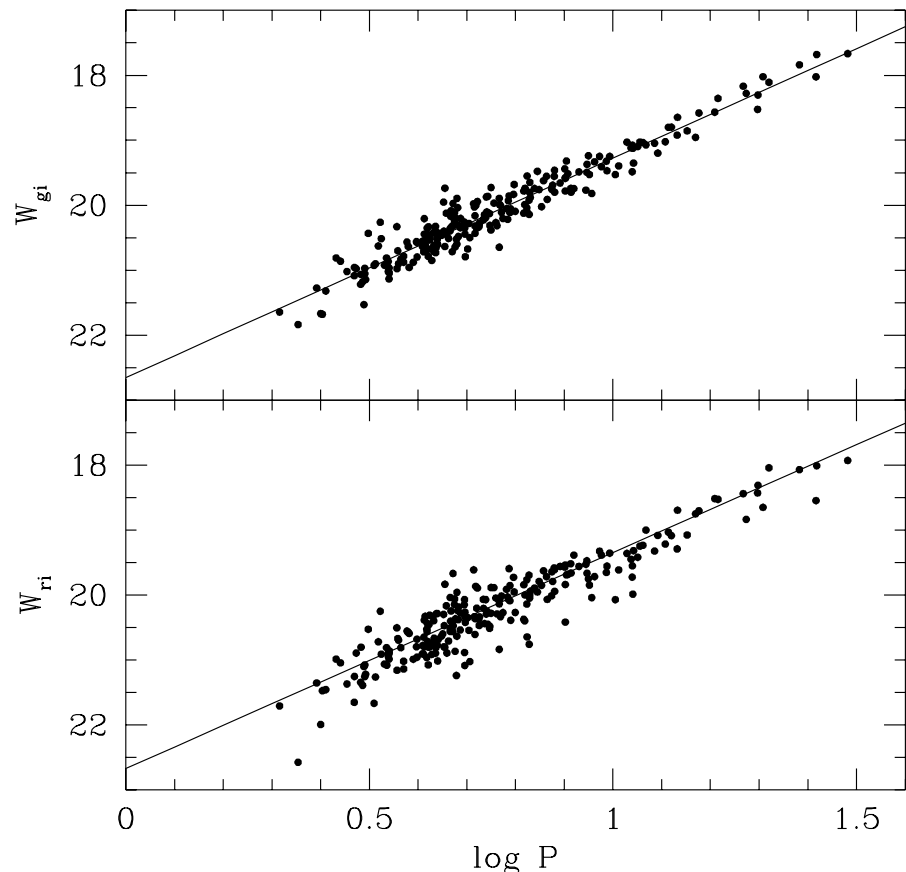


Figure 4.6: Sloan band Wesenheit PL relations for  $Z_{LMC}$  sample. The weighted least squares fit takes the intrinsic scatter into account. The scatter is larger on the  $W_{ri}$  relation as the colour coefficient is larger.

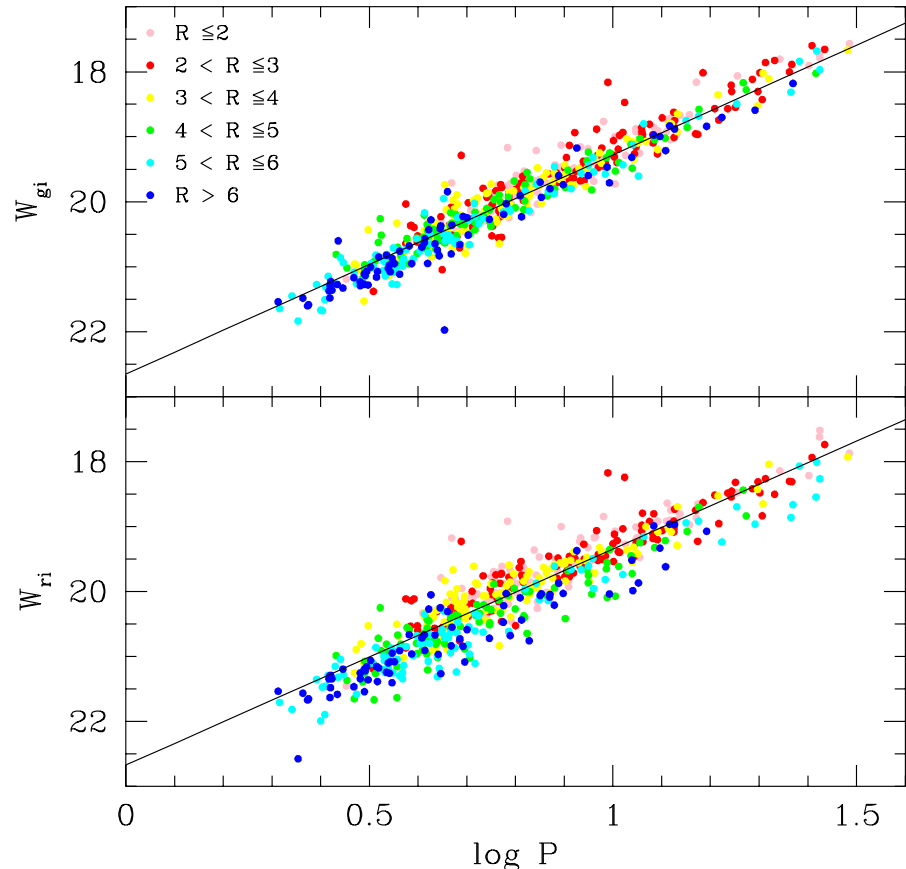


Figure 4.7: Wesenheit PL relations for the entire sample. The black lines show the relations in Equations 4.10 and 4.11, which were fit using the  $Z_{LMC}$  sample only. The colours represent the radial distance of the Cepheid, with pink and red corresponding to  $Z > Z_{LMC}$ , green and yellow as  $Z_{LMC}$  and blue showing  $Z < Z_{LMC}$ . The high metallicity points tend to lie above the relation, with the low metallicity points below the line.

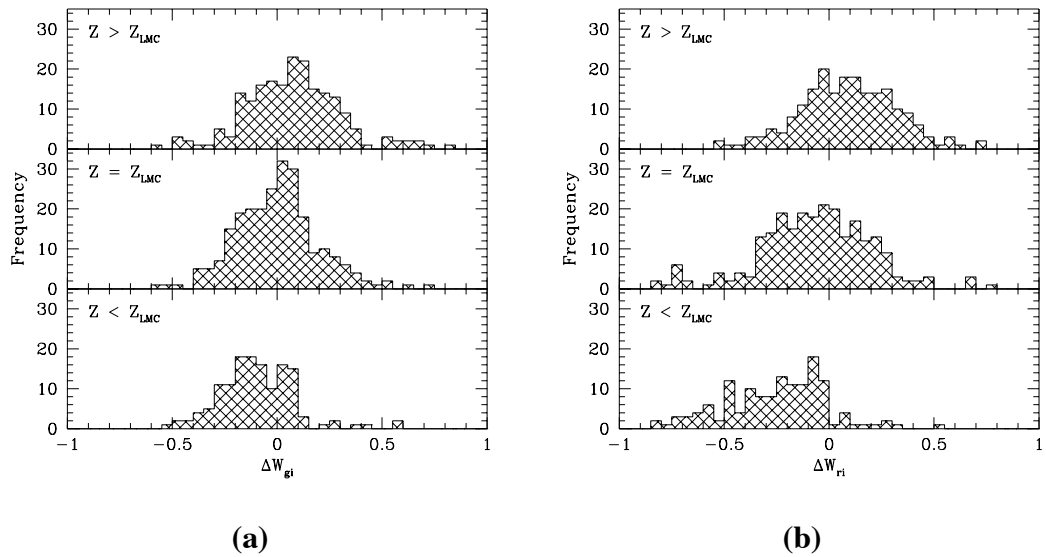


Figure 4.8: Histograms of deviations from Wesenheit PL relations: (a)  $W_{gi}$ , (b)  $W_{ri}$ . Both indices show a clear shift with metallicity

Cepheids throughout the whole galaxy, so  $\gamma$  can be calculated from the gradient of the distance modulus.

Section 3.7.1 explains how the chosen metallicity gradient can affect  $\gamma$ . Rather than find the change in  $\mu$  with metallicity, we will find  $\frac{d\mu}{dR}$ , where  $R$  is the radial distance in kpc. This can then be adapted to  $\frac{d\mu}{dZ}$  for different gradients.

Figure 4.9 shows the distance modulus derived for each Cepheid against the deprojected galactocentric distance, assuming a true distance modulus of 24.53 mag (Section 3.7). The red lines show the weighted least squares fit to the data, with both  $W_{gi}$  and  $W_{ri}$  showing an increase of distance modulus with radial distance. Using radial distance as a proxy for metallicity, this infers an increase of  $\mu$  with decreasing  $Z$ ; put simply, a negative value for  $\gamma$ .

The weighted least squares fits are given by the equations

$$\mu_{qi} = 0.0416R + 24.366 \quad (4.14)$$

and

$$\mu_{ri} = 0.0856R + 24.246. \quad (4.15)$$

An interesting thing to note at this point is that the zero-point of Equation 4.14 is very similar to the inner field  $\mu$  found from  $W_{vi}$  in Chapter 3. This is to be expected, as the effective wavelengths of the  $V$  and  $g'$  bands are similar, as are the definitions of  $W_{vi}$  and  $W_{gi}$ . Given this, the value of  $\gamma$  found from  $W_{gi}$  should be similar to that found in Chapter 3, although the same cannot be said for  $W_{ri}$ .

Equations 4.14 and 4.15 can now be converted to functions of metallicity via the relation

$$\gamma = \frac{d\mu}{d \log Z} = \frac{d\mu}{dR} \times \frac{dR}{d \log Z}. \quad (4.16)$$

This technique is only applicable if a single-component metallicity gradient is used. Using a two component gradient such as that of Magrini et al. (2007) in combination with the single component fits in Equations 4.14 or 4.15 would be mathematically incorrect. To rectify this, a double component fit is performed by  $\chi^2$  minimisation, using the following conditions:

1. The two fits must match at  $R = 3$  kpc — a discontinuity would be unphysical.
2. The ratio of the two gradients must be equal to the ratio of the two metallicity gradients. This ensures that  $\gamma$  is *not* a function of metallicity.

Using a brute-force technique<sup>7</sup>, iterating over a reasonable amount of parameter space, the best fits were found to be

$$\begin{aligned} \mu_{gi} &= 0.0932R + 24.260 \quad (R < 3 \text{ kpc}) \\ \mu_{gi} &= 0.0186R + 24.484 \quad (R \geq 3 \text{ kpc}) \end{aligned} \quad (4.17)$$

and

$$\begin{aligned} \mu_{ri} &= 0.1844R + 24.043 \quad (R < 3 \text{ kpc}) \\ \mu_{ri} &= 0.0369R + 24.485 \quad (R \geq 3 \text{ kpc}) \end{aligned} \quad (4.18)$$

---

<sup>7</sup>A bi-weight fit was also tested. This type of fit is better at ignoring outliers and could produce a more robust result. It produced almost exactly the same result, but with much larger errors.

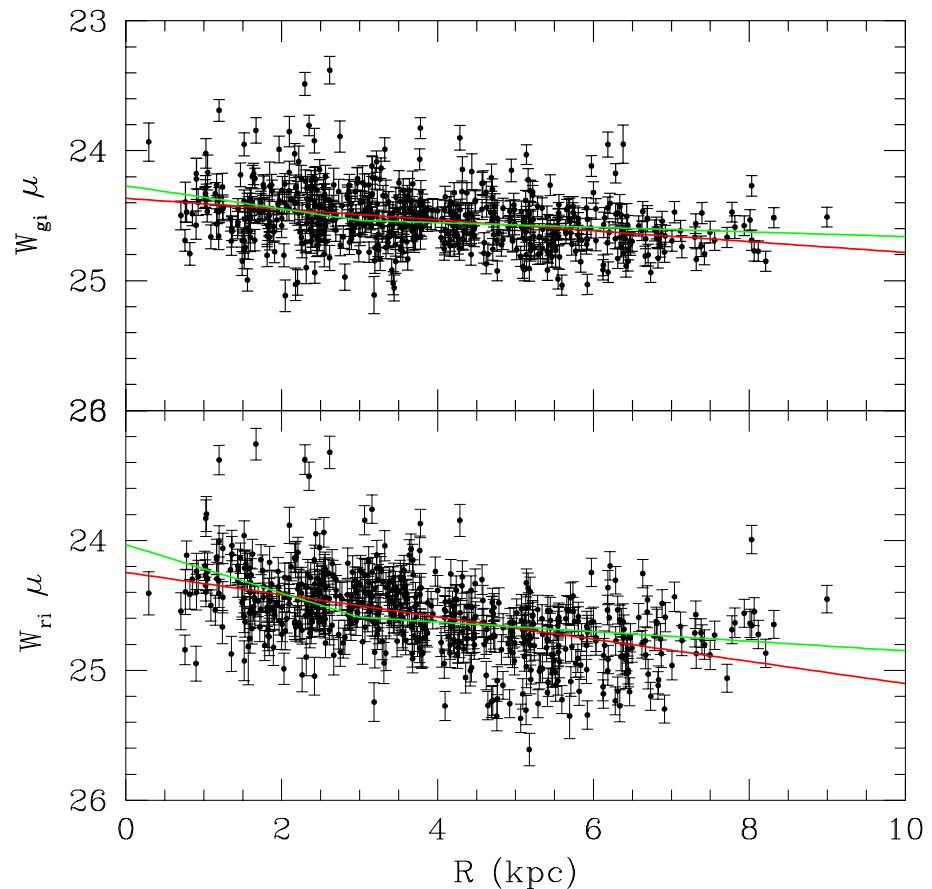


Figure 4.9: Change in measured  $\mu$  with deprojected galactocentric distance. Top panel:  $W_{gi}$ , bottom panel:  $W_{ri}$ . The red lines show the weighted least squares fit to the data. The green lines show the two-component fit found using a  $\chi^2$  minimisation. Both panels show a clear shift to larger distance moduli with increasing radial distance, which infers an increase of  $\mu$  with decreasing metallicity — or a negative value for  $\gamma$ .

Wesenheit index	$\frac{d\mu}{dR}$	$\frac{d\log Z}{dR}$	$\frac{d\log Z}{dR}$ source	$\gamma$ mag dex $^{-1}$
$W_{gi}$	$0.042 \pm 0.005$	$-0.127 \pm 0.011$	Zaritsky et al.	$-0.331 \pm 0.049$
		$-0.012 \pm 0.011$	Crockett et al.	$-3.500 \pm 3.325$
	$0.093 \pm 0.006$	$-0.190 \pm 0.080$	Magrini et al.	$-0.489 \pm 0.208$
$W_{ri}$	$0.086 \pm 0.006$	$-0.127 \pm 0.011$	Zaritsky et al.	$-0.677 \pm 0.075$
		$-0.012 \pm 0.011$	Crockett et al.	$-7.167 \pm 6.588$
	$0.184 \pm 0.007$	$-0.190 \pm 0.080$	Magrini et al.	$-0.968 \pm 0.409$

Table 4.9:  $\gamma$  values from  $W_{gi}$  and  $W_{ri}$  PL relations and different metallicity gradients. The single-gradient  $\frac{d\mu}{dR}$  fits are applied to the single-component metallicity gradients, with the  $R < 3$  kpc segment of the double-component fit applied to the Magrini et al. (2007) gradient. The same values for  $\gamma$  are found when the  $R \geq 3$  segment is used.

which are shown as green lines in Figure 4.9.

Applying the appropriate  $\frac{d\mu}{dR}$  values to the metallicity gradients  $\gamma$  can be derived. The results are shown in Table 4.9.

Three important points can be drawn from Table 4.9:

1. If the difference in distance modulus is interpreted as a metallicity effect, the shallow metallicity gradient found by Crockett et al. (2006) is inappropriate.
2. Although slightly higher than the WIYN  $W_{vi}$   $\gamma$  result, the values derived from  $W_{gi}$  agree with it, within the limits of the uncertainties.
3. The value derived using the Magrini et al. (2007) gradient is limited by the uncertainties on both the metallicity gradient and the double-component fit.

### Unsuitability of a very shallow metallicity gradient

It was implied in Chapter 3 that the shallow metallicity gradient postulated by Crockett et al. (2006) was incorrect. Firstly, it is important to remember that this is only the case if the difference in distance modulus is interpreted as a metallicity effect. It may well be that the  $\Delta\mu$  is present, but is caused by something other than a change in metallicity. However, for the purposes of this analysis, and with the lack of other plausible

explanations for a trend of increasing  $\mu$  with galactocentric radius, the assumption of a metallicity effect will be maintained

Table 4.9 compares the different values of  $\gamma$  found using the different passbands and metallicity gradients. The values found using the shallow gradient are at odds with those from the steep gradients, as well as with independent measurements from other galaxies (Macri et al., 2006, for example, who found  $\gamma = -0.29 \pm 0.09_{rand} \pm 0.05_{sys}$  using NGC 4258). Although Figure 4.9 shows that there is clearly a trend of increasing distance modulus with radius, the magnitude of the effect found with the shallow gradient would imply that serious corrections are required to the Cepheid distance scale. As Cepheid distances are generally in agreement with other measurement techniques, this is certainly not correct.

## 4.9 Conclusions

For the first time, the period–luminosity relations for the Sloan  $g', r', i'$  bands have been found observationally:

$$g' = -2.410(\pm 0.080) \log P - 1.583(\pm 0.057) \quad (4.19)$$

$$r' = -2.724(\pm 0.067) \log P - 1.719(\pm 0.052) \quad (4.20)$$

$$i' = -2.840(\pm 0.056) \log P - 1.706(\pm 0.051) \quad (4.21)$$

The zero–points of these relations are dereddened, assume distance moduli of the LMC and the WIYN M33 outer field of 18.4 and 24.54 mag respectively, and are appropriate for a metallicity of  $12 + \log(O/H) = 8.30$ . The slopes are all shallower than predicted by the empirical relations of Ngeow & Kanbur (2007). Their slopes were tested, but were found to produce a worse fit.

Using the whole–galaxy Cepheid sample from CFHT, the presence of a metallicity effect on the period–luminosity relation zero–point is confirmed. The reddening–free

Wesenheit indices in the Sloan bands are defined as

$$\begin{aligned} W_{gi} = & -3.377(\pm 0.058) \log P + 22.655(\pm 0.046) \\ & + 0.331(\pm 0.049)(\log(O/H)_{LMC} - \log(O/H)) \end{aligned} \quad (4.22)$$

and

$$\begin{aligned} W_{ri} = & -3.323(\pm 0.083) \log P + 22.672(\pm 0.066) \\ & + 0.677(\pm 0.075)(\log(O/H)_{LMC} - \log(O/H)) \end{aligned} \quad (4.23)$$

where the metallicity correction factors are derived using the M33 metallicity gradient of Zaritsky et al. (1994).

Although the metallicity gradient of Magrini et al. (2007) is more recent, and takes into account the possible change in slope at  $R = 3$  kpc, its large uncertainties prove troublesome. As discussed in Section 3.7.1, although it may in fact be a truer representation of chemical composition of M33, the fit presented by Magrini et al. is not easily reproducible. Further investigation into the nature of the gradient would prove invaluable to the calibration of the PL relation.

As this work is the first to calculate observational PL relations for the Sloan bands, there is currently no other work to compare them to. However, that the  $W_{gi}$  metallicity correction agrees so well with the  $W_{vi}$  value adds weight to the result. The technique uses relative distances, so at no point are true distance moduli of the LMC or M33 assumed, which may otherwise have introduced biases into the calculations. The fact that the  $W_{ri}$  correction is larger does not disprove this point; as different wavebands are considered there is no reason to assume that the correction should be the same. Nevertheless,  $\gamma_{ri}$  is found to be broadly similar, leading to the conclusion that the technique is robust. Further discussion into why  $\gamma$  changes for different passbands can be found in Chapter 6.

# Chapter 5

## Conclusions

### 5.1 Overview of results

The three main conclusions of the thesis are as follows:

1. The observed Wesenheit indices ( $W_{vi}$ ,  $W_{gi}$  and  $W_{ri}$ ) of Cepheids decrease (*i.e.*, they appear brighter, and therefore less distant) as  $12 + \log(O/H)$  increases. To correctly measure Cepheid distances using the period–luminosity relation the metallicity effect must be taken into account, via the  $\gamma$  correction.
2. The PL relation for fundamental Cepheids in the Wesenheit indices is linear.
3. Metallicity affects the  $B$ ,  $V$  and  $I_C$  Cepheid magnitudes in the same direction as it does the Wesenheit indices.
4. M33 must have a reasonably steep metallicity gradient, at least in the central region of the galaxy.

In addition, the PL relations for the Sloan  $g'$ ,  $r'$ ,  $i'$  bands, and their corresponding Wesenheit indices have been found observationally for the first time.

## 5.2 Sloan band period–luminosity relations

In recent years, there has been a shift in the observational community towards the Sloan photometric system. As the Sloan Digital Sky Survey has provided such an enormous amount of data, it is to be expected that both old and new instruments will be adapted to use this filter set. Not only does SDSS provide huge amounts of photometry and spectroscopy, one region in particular serves as an ideal calibration region. Stripe 82 has been observed repeatedly during the survey and contains a large number of standard stars that can be used as an alternative to the Landolt system. It is therefore no surprise that Cepheids should join in the move towards Sloan.

Before this study, the only published period–luminosity relations in the  $g'$ ,  $r'$  and  $i'$  bands were the semi–empirical versions produced by Ngeow & Kanbur (2007), which were discussed in Section 4.7. Although they provide a reasonable estimate, it is important that a purely observational version is found.

The dereddened, empirical  $g'$ ,  $r'$ ,  $i'$  PL relations were found as follows:

$$g' = -2.41(\pm 0.08) \log P - 1.58(\pm 0.05), \quad (5.1)$$

$$r' = -2.72(\pm 0.07) \log P - 1.72(\pm 0.05), \quad (5.2)$$

$$i' = -2.84(\pm 0.06) \log P - 1.71(\pm 0.05). \quad (5.3)$$

The zero–point terms assume that the distance moduli of the LMC and M33 outer field are 18.4 and 24.54 mag respectively, the  $R_V = 3.23$  reddening law of Cardelli et al. (1989) holds, and that  $E(B - V) = 0.098 \pm 0.030$  for the WIYN outer field.

The slopes of the relations in Equations 5.1, 5.2 and 5.3 are around 0.1 mag shallower than the semi–empirical versions, although they are consistent within their respective error bars. It is important to note, however, that these relations are only appropriate for samples of Cepheids with the same metallicity as the WIYN outer field, which is just below that of the LMC.

There has been no attempt here to find a metallicity dependence in these relations, as

the reddening cannot be calculated for the entire galaxy at the present time. However, this result is still remarkably important. Not only is it the first experimental calculation of its kind, but it shows that the semi-empirical results are sound.

## 5.3 Metallicity effects on Wesenheit indices

It is fair to say that the use of the Wesenheit index  $W_{vi}$  in Cepheid observations proved to be a great leap forward in the field. The index removes reddening without the need for independent measurements of the extinction, so long as the correct reddening law is assumed.

However, the Wesenheit index is not perfect. This work has shown that metallicity has a significant effect on the observed index of a Cepheid. As the oxygen abundance increases, the Wesenheit index decreases (i.e. the Cepheid appears brighter). This apparent change in brightness will carry through to distance measurements, resulting in smaller distance moduli for more metal-rich samples. The magnitude of the effect is quantified by  $\gamma$ .

In each case the PL relation has been redefined, so that it now takes the form

$$W = a \log P + b - \gamma(\log(O/H)_{LMC} - \log(O/H)) \quad (5.4)$$

where  $\log(O/H)_{LMC}$  and  $\log(O/H)$  are the metallicities of the LMC and the region being observed.

### 5.3.1 The effect on $W_{vi}$

The effect of metallicity on the  $W_{vi}$  index is discussed in Section 3.7. Using the two regions observed in the WIYN survey in the  $B, V, I_C$  bands, the  $W_{vi}$  PL relation was

found to be

$$\begin{aligned} W_{vi} = & -3.32(\pm 0.01) \log P + 22.01(\pm 0.03) \\ & + 0.29(\pm 0.09)(\log(O/H)_{LMC} - \log(O/H)). \end{aligned} \quad (5.5)$$

In this case,  $\gamma$  is found to be  $-0.37 \pm 0.09 \text{ mag dex}^{-1}$ , which is consistent with previous measurements (Sakai et al., 2004, for example). In this case, the two-slope metallicity gradient from Magrini et al. (2007) was used.

Using the redefined PL relation, the distance modulus of M33 is  $24.52 \pm 0.11$ . This is consistent with other results from both Cepheids and other techniques such as tip of the red giant branch measurements.

### 5.3.2 The effect on $W_{gi}$

As with the regular PL relations, the Wesenheit PL relations had not yet been calibrated in the Sloan system. An estimate of the  $W_{gi}$  PL relation was obtained from the semi-empirical models, and is given in Equation 4.12, whilst it was measured observationally as

$$\begin{aligned} W_{gi} = & -3.38(\pm 0.06) \log P + 22.66(\pm 0.05) \\ & + 0.33(\pm 0.05)(\log(O/H)_{LMC} - \log(O/H)), \end{aligned} \quad (5.6)$$

where the slope is found to be consistent with the semi-empirical derivation.

Here,  $\gamma$  is slightly larger than for the  $W_{vi}$  calculation at  $-0.33 \pm 0.05 \text{ mag dex}^{-1}$ . In this case, the single-slope metallicity gradient from Zaritsky et al. (1994) was used. Using the two-component version resulted in a larger value of  $\gamma = -0.49 \pm 0.21$ . Although this is compatible with the single-slope version, the uncertainty introduced by the double-gradient is very large.

As expected from the construction of the  $W_{vi}$  and  $W_{gi}$  indices,  $\gamma$  for  $W_{gi}$  is close to the

value obtained for  $W_{vi}$ . The colour coefficients that come from the extinction terms are similar, as are the effective wavelengths of  $g'$  and  $V$  and  $i'$  and  $I_C$ . The fact that these two independent calculations of  $\gamma$  are so close prove that the metallicity effect is indeed present, and that the size found is correct.

### 5.3.3 The effect on $W_{ri}$

The metallicity correction for the  $W_{ri}$  index is a different problem than the previous two calculations. Like  $W_{gi}$ , the PL relation had not yet been measured observationally. With  $W_{vi}$ , and to an extent  $W_{gi}$ , previous measurements of  $\gamma$  were available as a comparison. Towards the red end of the optical spectrum however, there has been no attempt to quantify the effect in this way.

Using the same method as before, the new PL relation was found to be

$$\begin{aligned} W_{ri} = & -3.32(\pm 0.08) \log P + 22.67(\pm 0.07) \\ & + 0.68(\pm 0.08)(\log(O/H)_{LMC} - \log(O/H)), \end{aligned} \quad (5.7)$$

with  $\gamma$  found to be significantly higher this time at  $0.68 \pm 0.08 \text{ mag dex}^{-1}$ .

What is particularly interesting about this value is that it is 2.1 times higher than the one from  $W_{gi}$ . Although this number may at first appear unremarkable, when you compare it to the definition of the Wesenheit index it suddenly stands out. Firstly, we average the absolute values of the magnitude terms in the two definitions:

$$W_{gi} : \frac{2.248(i') + 1.248(g')}{2} = 1.748 \quad (5.8)$$

$$W_{ri} : \frac{4.064(i') + 3.064(r')}{2} = 3.564 \quad (5.9)$$

The ratio of these two numbers is the same as the ratio of the two  $\gamma$ s, implying that as the coefficient in the Wesenheit definition increases, so does  $\gamma$ . Taking this one step further, one could infer that using a Wesenheit index with a small colour term could reduce the metallicity effect, although the algebra implies that it could not be removed

altogether in this manner. A plan for testing this hypothesis is described in Section 6.1.

As this is the first measurement of  $\gamma$  in this regime no comparisons can be made with other results. Nevertheless, as the photometry is sound and the result for  $W_{gi}$  is as expected, there is no reason to think that the same cannot be said here.

### 5.3.4 The linearity of the PL relation

In recent times there has been some suggestion that the PL relation is not linear, but exhibits a change in slope around 10 days. Not only has this effect only been seen in a few Cepheid populations, but there has not been an adequate explanation as to why this should occur. However, with the large sample available from the CFHT survey, an explanation of the break may have been found.

Figures 5.1 and 5.2 show the Wesenheit PL relations in two ways. The top panels have the points colour-coded by radial distance, and the bottom panels show all the points in black. In the bottom panel of Figure 5.2 it appears as though the slope of the PL relation changes just below  $\log P = 1$ . However, when it is compared with the top panel, it becomes clear that this is not the case.

By splitting the Cepheids into several populations at different metallicities, one can see that the apparent slope change is a result of the superposition of these different populations. The effect is also present in Figure 5.1, but to a much smaller extent. The red and blue lines in the bottom panels show the PL fits when the samples are split at  $\log P = 1$ . Although the difference is very small in  $W_{gi}$ , it suggests that the mixing of the different metallicity samples is having an effect.

However, the fact that the slope change is seen in the LMC PL relations from OGLE suggests that metallicity is not the culprit. The LMC has a small dispersion in metallicity, so the effect described above would not be seen. It may be that the topology of the instability strip is changed at different metallicity, such that the different mixes of stars will affect the slope. However, the M33 data suggest that there is no slope change with  $Z$ .

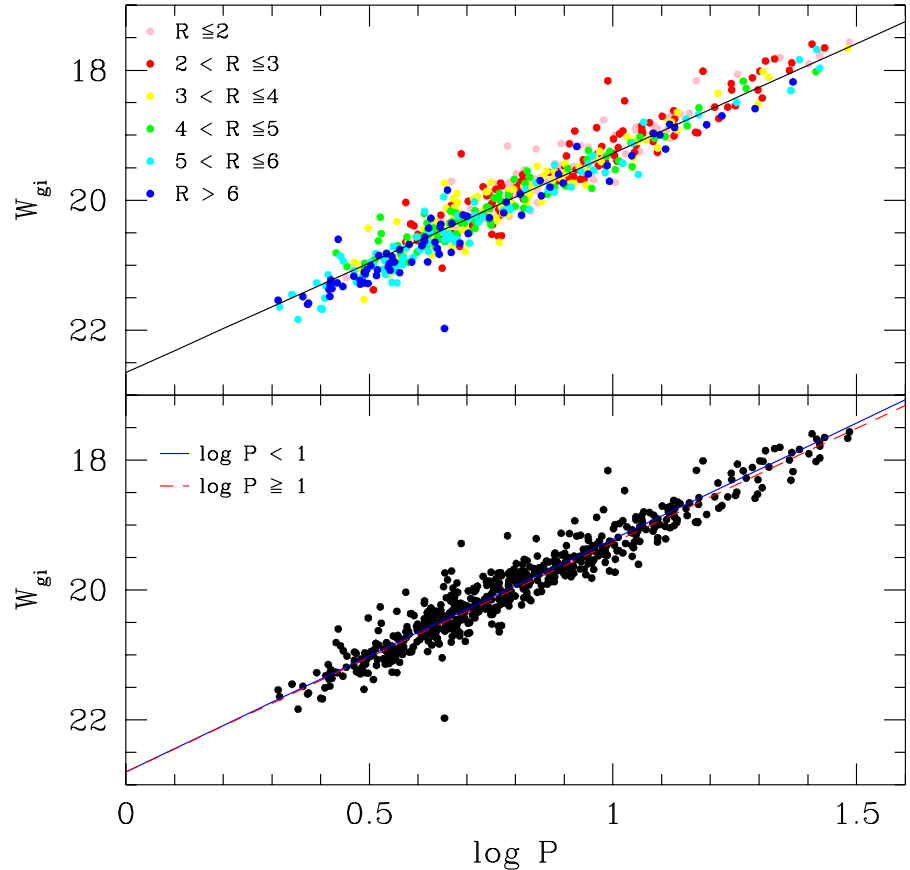


Figure 5.1: Proof that the  $W_{gi}$  PL relation is linear. The top panel shows the Cepheids colour-coded by radial distance (as a proxy for metallicity), with the colours removed for the bottom panel. The best-fit line on the top panel represents the PL relation derived from the  $Z_{LMC}$  Cepheids, with the red and blue lines on the bottom panel showing the two weighted-least-squares fits when the sample is split at  $\log P = 1$ . A small change in slope is found ( $\Delta = -0.05$ ), but this is believed to be due purely to the superposition of the different metallicity samples.

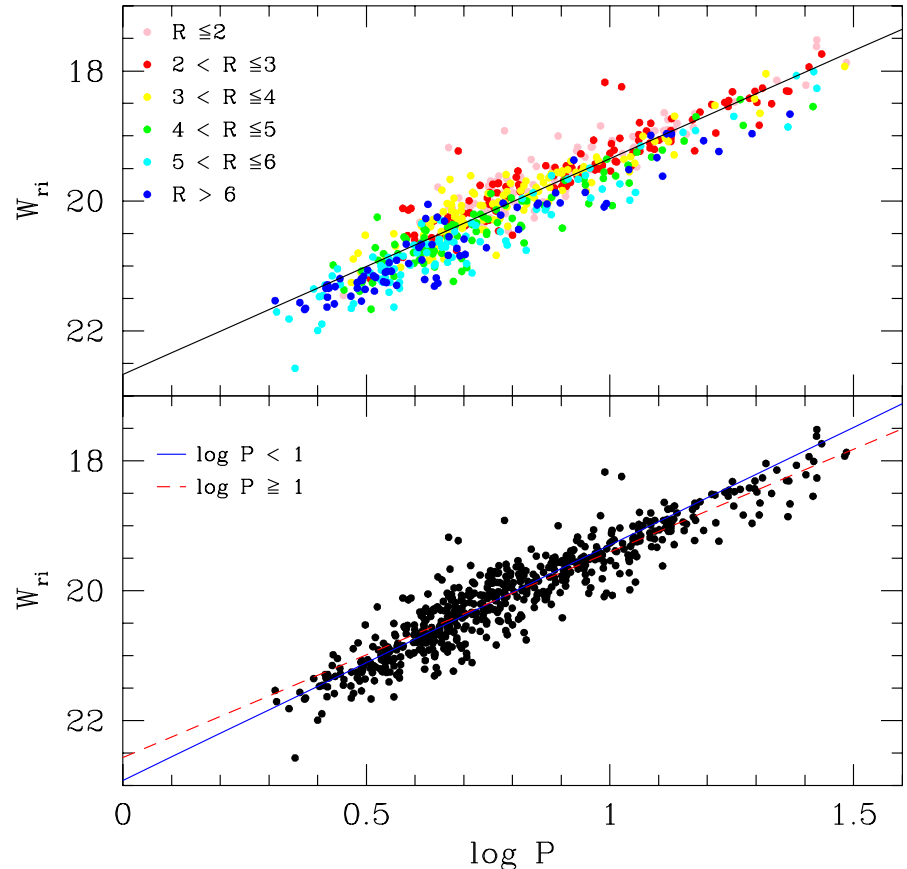


Figure 5.2: Proof that the  $W_{ri}$  PL relation is linear. The top panel shows the Cepheids colour-coded by radial distance (as a proxy for metallicity), with the colours removed for the bottom panel. The best-fit line on the top panel represents the PL relation derived from the  $Z_{LMC}$  Cepheids, with the red and blue lines on the bottom panel showing the two weighted-least-squares fits when the sample is split at  $\log P = 1$ . A larger slope change is found in this case ( $\Delta = -0.46$ ), but this is again believed to be due purely to the superposition of the different metallicity samples. As the metallicity effect is larger in  $W_{ri}$  a larger slope change is to be expected

The evidence presented here leads to the conclusion that the nonlinearities discussed in Section 1.4.1 are not a physical effect, but are due to inhomogeneous metallicity sampling, at least in M33.

## 5.4 Metallicity effects on $B, V, I_C$

Although the  $B, V, I_C$  PL relations were not discussed in detail in Chapter 3, they are still important. After they had been corrected for reddening, the zero-points of the relations were found to differ between the two fields. The magnitude of the difference in  $V$  was found to be the same as  $W_{vi}$ , with  $\Delta B$  and  $\Delta I_C$  around half  $\Delta V$ . The differences were found to be in the same direction in all cases, *i.e.*, a negative value for  $\gamma$ . As was discussed in Section 1.4.3, Sandage et al. (1999) found that a metallicity effect was predicted theoretically. However, they found that the effect on  $B$  would be in the opposite direction to  $V$  and  $I_C$ , and that the effect on  $B$  would be in the same direction as we find observationally. This is an interesting discrepancy, and at the present time there is not an explanation to why this work finds an effect with the same sign as the theoretical prediction in only one passband.

## 5.5 The metallicity gradient of M33

As a by-product of the investigation into the effect of metallicity on Cepheid magnitudes, the nature of the abundance gradient itself has been explored. It is clear from Figure 4.9 that there is a trend of increasing distance modulus with radial distance. The only physical explanation for this is a metallicity effect; there is no other plausible explanation for a positional trend.

Table 5.1 gives a summary of the  $\gamma$  results using the three different PL relations and metallicity gradients. The values found using the Zaritsky et al. (1994) and Magrini et al. (2007) are reasonable in all three bands, whereas the Crockett et al. (2006) values are clearly far too high.

Wesenheit index	$\frac{d \log Z}{d R}$	source	$\gamma$ mag dex $^{-1}$
$W_{vi}$	Zaritsky et al.	$-0.27 \pm 0.07$	
	Crockett et al.	$-2.91 \pm 2.74$	
	Magrini et al.	$-0.29 \pm 0.09$	
$W_{gi}$	Zaritsky et al.	$-0.33 \pm 0.05$	
	Crockett et al.	$-3.50 \pm 3.33$	
	Magrini et al.	$-0.49 \pm 0.21$	
$W_{ri}$	Zaritsky et al.	$-0.68 \pm 0.08$	
	Crockett et al.	$-7.17 \pm 6.59$	
	Magrini et al.	$-0.97 \pm 0.41$	

Table 5.1: Summary of metallicity corrections found using different abundance gradients. The  $\gamma$ s found from Zaritsky et al. (1994) and Magrini et al. (2007) are reasonable in all three bands. The Crockett et al. (2006) gradient gives value for  $\gamma$  that are far too large, and would mean that significant recalibration of the Cepheid distance scale is required.

Assuming  $12 + \log[O/H] = 8.22$  for the SMC (Costa et al., 2000), a metallicity difference of 0.12 dex is found when compared to the LMC. One of the most recent Cepheid distances to the SMC is  $18.93 \pm 0.02$  (Keller & Wood, 2006), giving  $\Delta\mu = \mu_{SMC} - \mu_{LMC} = 0.53$  when  $\mu_{LMC} = 18.4$  is assumed. Using  $\gamma_{vi} = -0.29$  mag dex $^{-1}$  would decrease  $\Delta\mu$  by 0.04 to 0.49 mag, which is still a reasonable value.

However, when  $\gamma_{vi} = -2.91$  mag dex $^{-1}$  is used,  $\Delta\mu$  falls to 0.18 mag, which is incompatible with independent determinations of the SMC distance modulus. This shows that  $\gamma$  must be small, and hence that the oxygen abundance gradient of M33 must be steeper than Crockett et al. (2006) find.

A major source of uncertainty in the results of this thesis is the metallicity gradient. Figure 3.19 shows how the measured gradient can change depending on the galactocentric radii you choose to measure it at. At the present time the best solution would be to use the double-slope gradient, but this introduces new uncertainties by requiring a two-component fit to  $\frac{d\mu}{dR}$ . Until the discrepancies between the different gradients are reconciled, there can be no improvement in the measurement of  $\gamma$  from M33 Cepheids. However, work is currently underway to solve this problem. Section 6.2 discusses a new technique, developed by Beaulieu et al. (2006), which is currently being used to calculate the metallicity gradient using double mode Cepheids.

# Chapter 6

## Future Work

### 6.1 Metallicity corrections to the Wesenheit indices

Section 5.3.3 discussed how the  $\gamma$  parameter changed between the  $W_{gi}$  and  $W_{ri}$  Wesenheit indices. The ratio of the  $\gamma$  values was found to be equal to the ratio of the magnitude terms in the Wesenheit index. If this relationship holds for all wavelengths then it may be possible to construct a Wesenheit index that would only require a very small metallicity correction.

Firstly, we consider just the Sloan system. By using two filters spaced a sufficient distance apart, we can construct an index that will have a small colour coefficient. Taking the  $u'$  and  $z'$  bands gives a Wesenheit index of

$$W_{uz} = u' - 1.450(u' - z') \quad (6.1)$$

Plugging this into Equation 5.8 gives a value of 0.95, which is 0.56 times that of  $W_{gi}$ . Following the same logic as for the comparison of  $W_{gi}$  and  $W_{ri}$ , one would therefore expect that  $\gamma$  would follow the same relation, falling to around  $-0.16 \text{ mag dex}^{-1}$ . This is much better than the correction required before, but would still result in a measurable difference between the inner and outer regions of M33.

To reduce the correction further, we can extend the theory to the infra-red. Wesenheit indices are not used in infra-red observations usually as extinction falls greatly at these wavelengths. Using the Sloan  $u'$  band with the UKIRT  $K$  band gives the following index:

$$W_{uk} = u' - 1.079(u' - K), \quad (6.2)$$

from which the average term from Equation 5.8 becomes 0.58, or 0.34 times the value from  $W_{gi}$ . This implies that the  $\gamma$  parameter in the  $W_{uk}$  PL relation would be  $-0.11 \text{ mag dex}^{-1}$ . This would reduce the correction on the SMC distance modulus to around 0.01 mag, which is well within the uncertainty limits of Cepheid observations.

A possible explanation for this effect is the large wavelength baseline being used in the construction of the index. Metallicity affects the colours of stars via line blanketing. This is when energy from the blue end of the spectrum is redistributed towards the infra-red. In the standard  $W_{vi}$  index, the wavebands in question are sufficiently close that the effects of line blanketing will still be noticeable. By widening the baseline, for example, by combining ultra-violet (or the short wavelength end of optical) and infra-red observations, it may be possible that the effect cancels out (or at least reduces to a negligible level).

One concern about this technique is that the Wesenheit indices are in fact a type of period–luminosity–colour relation. When they are used to correct for reddening, the indices also correct partly for the colour term in the PLC projection; this is why the  $W_{vi}$  PL relation is much tighter than the  $V$  PL relation, for example. The problem arises as the colour terms in the PLC relation are not yet well known, meaning that there is currently no way of measuring how much of the scatter is due to left over colour from the PLC relation, and how much is truly due to metallicity. One way to test this would be using the data available from OGLE–III survey (Soszynski et al., 2008), as it contains enough stars such that the PLC relations can be measured accurately.

### 6.1.1 Addition of infra-red data

It will soon be possible to test this hypothesis. Infra-red observations of M33 have been made using WIRCam on CFHT. These will be combined with the optical data discussed in Chapter 4, allowing the method described above to be tested. If the prediction is correct, the trend seen in Figure 4.9 should be much shallower, possibly not detectable at all.

As well as the opportunity to test the different Wesenheit indices, the addition of the infra-red data will improve the PL relations greatly. The amount of extinction drops greatly in this bandpass, and will enable improvements to the reddening corrections. This will allow us to calibrate the zero-points  $g'$ ,  $r'$  and  $i'$  band PL relations using the whole sample, rather than just those for which we have independent measurements of the reddening, and will bring down the uncertainties on the fits.

## 6.2 Independent metallicity measurements

The complications introduced by the uncertain metallicity gradient of M33 have been a running theme throughout this work. In addition to the problems from differing values found by different groups, the nature of the measurements present their own questions. The gradients used here all come from HII regions (with the exception of the innermost regions of Magrini et al. (2007)), which examines the composition of the gas in the galaxy. Perhaps a better way to find  $\gamma$  would be to use stars to measure the metallicity gradient; after all, Cepheids are stars.

In theory, this is an excellent idea. In practice however, things are not so simple. To measure the metallicity of a star requires precision spectroscopy, which is impossible to obtain with the telescopes currently available for all but the very nearest stars. But once again, Cepheids can come to the rescue.

Figure 6.1 shows a Petersen diagram (Petersen, 1973) for double mode Cepheids in the Milky Way, Magellanic Clouds and M33. The ratio of the two periods of funda-

mental and first overtone modes (F-O1) is known to be a strong function of metallicity (Moskalik et al., 1992), which is clear from the trends for the MW and MCs. These galaxies are known to have very small spreads in metallicity, hence the Cepheids have follow almost parallel lines in the diagram.

In 2006, Beaulieu et al. published a paper which described how the metallicity of a double-mode Cepheid could be derived using its two periods. In pulsation calculations the Cepheid envelope can be characterised by four parameters — mass, luminosity, effective temperature and metallicity. The period of pulsation must therefore be a function of these variables alone. Using a reasonable range of effective temperatures for double-mode Cepheids, a solution is found for luminosity and mass which generates the two observed periods of the Cepheid, and would also make the Cepheid unstable in both the fundamental and first overtone modes. The metallicity is then taken to be the value that gives the best fit.

Using the H06 data, Beaulieu et al. found five F-O1 Cepheids. They derived the metallicity of each of these, and found a metallicity gradient of  $-0.16 \text{ dex kpc}^{-1}$ . This is consistent with the steeper gradients from HII regions, but once again puts the shallow gradient out of the picture. This can also be seen in Figure 6.1; unlike the other galaxies the M33 Cepheids follow a steep trend. A fit to the points would cross over the LMC and MW lines, showing that the metallicity gradient must encompass these two values.

This work is being extended with new data from the INT, taken in October 2008 and September 2009. The extra data adds around 50 epochs to the CFHT survey, and should allow *every* double-mode Cepheid in M33 to be detected and both periods measured. We expect to detect around 100 double-mode Cepheids, with around 40 of these being F-O1 pulsators. Using this number of objects spread around the galaxy should allow us to measure the metallicity gradient to better precision, as well as allowing us to calculate a more precise value for  $\gamma$ .

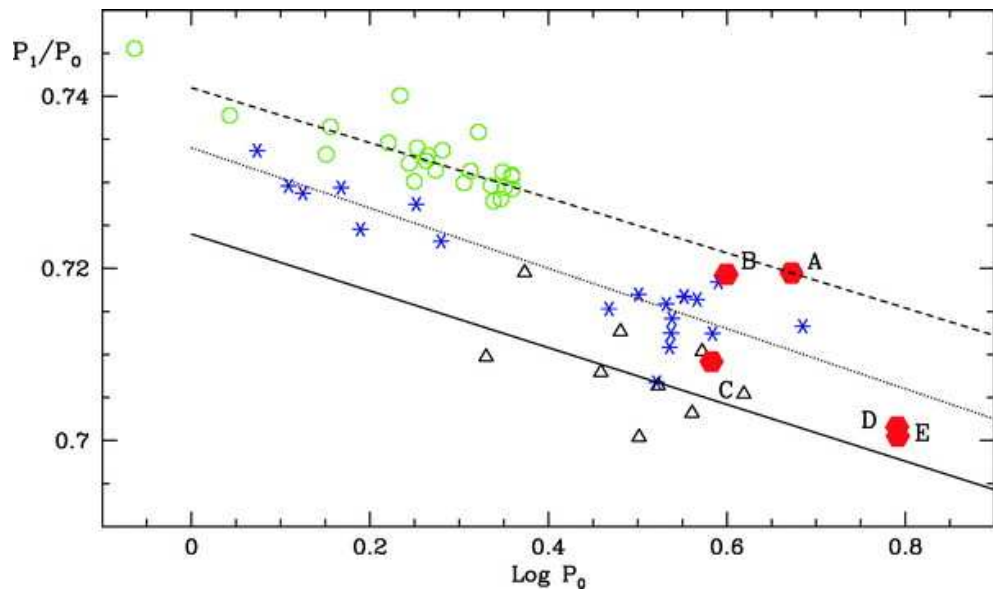


Figure 6.1: Petersen diagram for beat Cepheids in the Milky Way (black triangles), LMC (blue stars), SMC (green circles) and M33 (red hexagons). Clear trends are seen for the MW, LMC and SMC Cepheids, as these galaxies do not have large metallicity spread. The M33 Cepheids cross over the LMC and MW lines, proving that the metallicity gradient of M33 crosses over both of these galaxies. Figure taken from Beaulieu et al. (2006)

# Appendix A

## CFHT MegaCam Standard Solution

The CFHT MegaCam data were calibrated using the transformation equation

$$m_{CFHT} = m_{INT} + a + b \times Colour + c \times (Colour)^2 \quad (\text{A.1})$$

where  $m_{CFHT}$  is the instrumental reference magnitude from the H06 catalogue,  $m_{INT}$  is the calibrated magnitude from the INT M33 catalogue, and  $Colour$  refers to  $(g' - r')$  for  $g'$  and  $r'$ , and  $(r' - i')$  for  $i'$  band frames. The coefficients of the the solution for each CFHT chip that contained Cepheids are given in Table A.1.

The RMS values given in the final column are the root-mean-squared differences of the fitted and true magnitudes. The majority of these values are small; however, chip 3 in particular has larger RMS values than the others. The chips further away from the centre of the galaxy have less stars, in both the CFHT and the INT data. Hence, it becomes necessary to include stars with larger uncertainties in the fit to ensure a true representation. Whilst the RMS values for this fit are larger, they are still compatible with the uncertainties of the stars used.

Table A.1: Coefficients of the transformation equation which puts the H06 CFHT photometry on the SDSS standard system.

CFHT Chip	INT Field/Chip	Filter	<i>a</i>	<i>b</i>	<i>c</i>	RMS
2	NE 3	$g'$	0.425	-0.104	-0.057	0.024
		$r'$	0.305	-0.014	0.007	0.022
		$i'$	0.308	-0.068	0.002	0.022
3	NE 3	$g'$	0.435	-0.167	-0.047	0.083
		$r'$	0.301	-0.018	0.001	0.034
		$i'$	0.284	-0.079	0.009	0.061
4	NE 3	$g'$	0.388	-0.207	0.020	0.064
		$r'$	0.324	0.005	-0.021	0.041
		$i'$	0.289	-0.061	-0.017	0.056
5	NW 3	$g'$	0.345	-0.163	-0.007	0.056
		$r'$	0.276	-0.023	0.008	0.042
		$i'$	0.301	-0.094	0.005	0.058
6	NW 3	$g'$	0.323	-0.145	-0.010	0.031
		$r'$	0.234	-0.025	0.014	0.022
		$i'$	0.284	-0.055	-0.008	0.030
7	NW 3	$g'$	0.366	-0.231	0.040	0.023
		$r'$	0.249	-0.046	0.021	0.024
		$i'$	0.264	0.019	-0.032	0.024
11	NE 4	$g'$	0.129	-0.091	-0.034	0.040
		$r'$	0.133	0.007	-0.013	0.025
		$i'$	0.121	-0.034	-0.006	0.031
12	NE 4	$g'$	0.184	-0.187	0.008	0.055
		$r'$	0.151	-0.024	-0.005	0.039
		$i'$	0.113	-0.068	-0.005	0.049
13	NE 2	$g'$	0.233	-0.150	-0.020	0.050

*Continued on next page*

CFHT Chip	INT Field/Chip	Filter	<i>a</i>	<i>b</i>	<i>c</i>	RMS
14	NE 2	<i>r'</i>	0.042	-0.012	0.003	0.045
		<i>i'</i>	0.090	-0.022	-0.084	0.049
		<i>g'</i>	0.239	-0.144	-0.013	0.012
15	NW 4	<i>r'</i>	0.040	-0.018	0.012	0.021
		<i>i'</i>	0.121	0.051	-0.158	0.019
		<i>g'</i>	0.223	-0.145	-0.035	0.028
16	NW 4	<i>r'</i>	0.086	-0.022	0.026	0.019
		<i>i'</i>	0.146	-0.061	-0.030	0.027
		<i>g'</i>	0.138	-0.153	-0.007	0.015
20	SE 3	<i>r'</i>	0.046	0.045	-0.039	0.012
		<i>i'</i>	0.108	-0.121	0.070	0.021
		<i>g'</i>	0.266	-0.148	0.000	0.008
21	SE 3	<i>r'</i>	0.196	0.002	-0.006	0.006
		<i>i'</i>	0.227	-0.018	-0.038	0.009
		<i>g'</i>	0.258	-0.116	-0.036	0.018
22	SE 3	<i>r'</i>	0.189	-0.020	0.011	0.017
		<i>i'</i>	0.233	-0.069	-0.010	0.019
		<i>g'</i>	0.268	-0.109	-0.057	0.023
23	SE 2	<i>r'</i>	0.231	-0.065	0.037	0.016
		<i>i'</i>	0.245	-0.002	-0.187	0.017
		<i>g'</i>	0.170	-0.127	-0.021	0.024
24	SW 3	<i>r'</i>	0.237	0.015	-0.041	0.029
		<i>i'</i>	0.087	-0.109	0.022	0.024
		<i>g'</i>	0.488	-0.152	-0.030	0.019
25	SW 3	<i>r'</i>	0.354	0.006	-0.015	0.015
		<i>i'</i>	0.345	-0.036	-0.122	0.019
		<i>g'</i>	0.427	-0.172	-0.015	0.027

*Continued on next page*

CFHT Chip	INT Field/Chip	Filter	<i>a</i>	<i>b</i>	<i>c</i>	RMS
26	SW 3	<i>r'</i>	0.337	-0.032	-0.001	0.020
		<i>i'</i>	0.299	-0.093	-0.047	0.025
		<i>g'</i>	0.461	-0.094	-0.115	0.025
30	SE 1	<i>r'</i>	0.315	0.061	-0.068	0.024
		<i>i'</i>	0.288	-0.054	0.000	0.025
		<i>g'</i>	0.092	-0.108	-0.034	0.016
31	SE 1	<i>r'</i>	0.180	-0.210	0.076	0.0150
		<i>i'</i>	0.071	-0.008	-0.049	0.018
		<i>g'</i>	0.156	-0.188	0.008	0.013
32	SE 2	<i>r'</i>	0.102	0.010	-0.014	0.023
		<i>i'</i>	0.059	-0.035	-0.011	0.016
		<i>g'</i>	0.159	-0.142	-0.019	0.036
33	SW 1	<i>r'</i>	0.219	-0.019	0.006	0.039
		<i>i'</i>	0.096	-0.088	0.002	0.032
		<i>g'</i>	0.059	-0.153	-0.015	0.032
34	SW 1	<i>r'</i>	0.150	-0.003	-0.008	0.034
		<i>i'</i>	0.088	-0.067	0.010	0.035
		<i>g'</i>	0.163	-0.156	-0.009	0.026
35	SW 2	<i>r'</i>	0.053	-0.040	0.018	0.032
		<i>g'</i>	0.111	-0.027	0.026	0.035
		<i>i'</i>	0.142	-0.139	-0.019	0.020
		<i>r'</i>	0.097	0.000	0.000	0.020
		<i>i'</i>	0.131	-0.098	0.026	0.016

## Appendix B

# Fourier Analysis

Fourier analysis is a powerful technique for the analysis of light curves. By decomposing the light curve into Fourier components, the Cepheids can be classified into different categories according to their mode of pulsations.

In Fourier decomposition, a light curve can be approximated by the sum of several cosine functions. In this case the magnitude ( $M$ ) of the star at time  $t$  can be described by the equation

$$M = A_0 + \sum_i A_i \cos[i\omega(t - t_0) + \phi_i] \quad (\text{B.1})$$

where  $A_0$  is the phase averaged magnitude,  $A_i$  are the amplitude terms,  $\phi_i$  are the phase terms,  $t_0$  is the time of maximum brightness and  $\omega$  is the frequency of the pulsations. The equation is typically solved for between three and six harmonics, with the frequency  $\omega = \frac{2\pi}{P}$ .

### B.1 Fourier parameters

The method was first applied to Cepheids by Simon & Lee (1981). They also defined the Fourier parameters which are used to describe the shape of a Cepheid light curve:

$$R_{21} = \frac{A_2}{A_1}, \quad (\text{B.2})$$

$$R_{31} = \frac{A_3}{A_1}, \quad (\text{B.3})$$

$$\phi_{21} = \phi_2 - 2\phi_1, \quad (\text{B.4})$$

$$\phi_{31} = \phi_3 - 3\phi_1, \quad (\text{B.5})$$

where  $R_{21}$  and  $R_{31}$  measure the relative importance of the second and third Fourier terms, and  $\phi_{21}$  and  $\phi_{31}$  measure the phase differences between the first, second and third Fourier terms.

## B.2 Classification of M33 Cepheids

The Fourier analysis used to classify the Cepheids in the CFHT study was performed by J-B Marquette, who kindly provided the Fourier parameters as part of the Cepheid catalogue. Figure B.1 shows the values of  $R_{21}$ ,  $R_{31}$ ,  $\phi_{21}$  and  $\phi_{31}$  as a function of period. Fundamental mode Cepheids are shown in blue, with overtone pulsators in red.

The distinction between the fundamental and overtone Cepheids is seen most clearly in  $R_{21}$  (top left panel). Here there is a clear separation between the two populations along the Hertzsprung progression. There is slightly more mixing in the other parameters, but in each case it is clear that the overtone Cepheids are not following the same progression as the fundamental mode pulsators.

By selecting stars firstly by their position in the colour-magnitude diagram, then by Fourier analysis, a total of 2327 Cepheids were identified. The final H06 catalogue contains 1580 fundamental mode Cepheids. The sample was reduced for this work using amplitude ratio cuts and requiring phase averaged magnitudes to be available, and as a result contained 589 fundamental mode Cepheids.

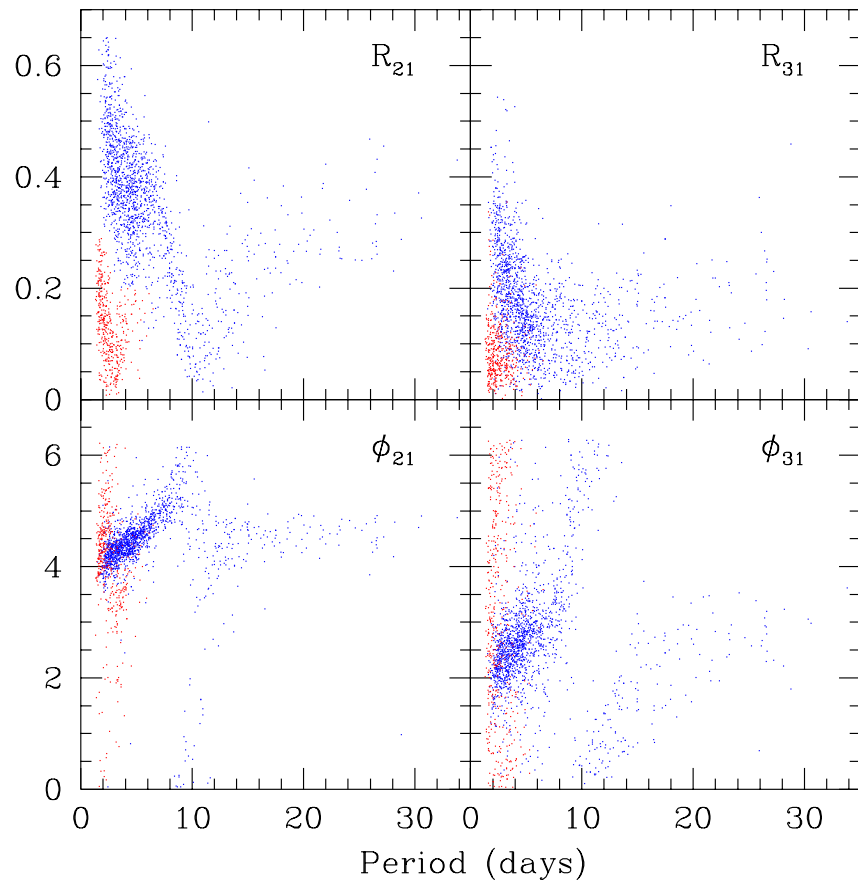


Figure B.1: Fourier parameters of the M33 Cepheids. Fundamental pulsators are shown in blue, overtones in red. All four parameters show the expected break in the Hertzsprung progression at  $P = 10$  days. This is due to the resonance between the fundamental mode and the second overtone; at  $P = 10$  days the resonance is 2:1, causing the amplitude ratios and phase differences to drop sharply.

# Bibliography

- Abazajian, K. N., Adelman-McCarthy, J. K., Agüeros, M. A., Allam, S. S., Allende Prieto, C., An, D., Anderson, K. S. J., Anderson, S. F., Annis, J., Bahcall, N. A., & 194 co-authors. 2009, ApJS, 182, 543
- Akritas, M. G. & Bershady, M. A. 1996, ApJ, 470, 706
- Alard, C. 2000, A&AS, 144, 363
- Alard, C. & Lupton, R. H. 1998, ApJ, 503, 325
- Alibert, Y., Baraffe, I., Hauschildt, P., & Allard, F. 1999, A&A, 344, 551
- Argon, A. L., Greenhill, L. J., Moran, J. M., Reid, M. J., Menten, K. M., & Inoue, M. 2004, ApJ, 615, 702
- Aubourg, E., Bareyre, P., Bréhin, S., Gros, M., Lachièze-Rey, M., Laurent, B., Lesquoy, E., Magneville, C., Milsztajn, A., Moscoso, L., Queinnec, F., Rich, J., Spiro, M., Vigroux, L., Zylberajch, S., Ansari, R., Cavalier, F., Moniez, M., Beaulieu, J.-P., Ferlet, R., Grison, P., Vidal-Madjar, A., Guibert, J., Moreau, O., Tajahmad, F., Maurice, E., Prévôt, L., & Gry, C. 1993, Nature, 365, 623
- Barlow, H. B. 1962, J. Physiol., 160, 169
- Bauer, F., Afonso, C., Albert, J. N., Alard, C., Andersen, J., Ansari, R., Aubourg, É., Bareyre, P., Beaulieu, J. P., Bouquet, A., Char, S., Charlote, X., Couchot, F., Coutures, C., Derue, F., Ferlet, R., Gaucherel, C., Glicenstein, J. F., Goldman, B., Gould, A., Graff, D., Gros, M., Haissinski, J., Hamilton, J. C., Hardin, D., de Kat, J., Kim, A., Lasserre, T., Lesquoy, É., Loup, C., Magneville, C., Mansoux, B.,

- Marquette, J. B., Maurice, É., Milsztajn, A., Moniez, M., Palanque-Delabrouille, N., Perdereau, O., Prévot, L., Renault, C., Regnault, N., Rich, J., Spiro, M., Vidal-Madjar, A., Vigroux, L., Zylberajch, S., & EROS Collaboration. 1999, *A&A*, 348, 175
- Beaulieu, J.-P., Buchler, J. R., Marquette, J.-B., Hartman, J. D., & Schwarzenberg-Czerny, A. 2006, *ApJ Let.*, 653, L101
- Becker, A. C., Silvestri, N. M., Owen, R. E., Ivezić, Ž., & Lupton, R. H. 2007, *PASP*, 119, 1462
- Benedict, G. F., McArthur, B. E., Feast, M. W., Barnes, T. G., Harrison, T. E., Patterson, R. J., Menzies, J. W., Bean, J. L., & Freedman, W. L. 2007, *AJ*, 133, 1810
- Bertin, E. & Arnouts, S. 1996, *A&AS*, 117, 393
- Bessell, M. S., Castelli, F., & Plez, B. 1998, *A&A*, 333, 231
- Binney, J. & Merrifield, M. 1998, *Galactic astronomy*, ed. J. Binney & M. Merrifield
- Bonanos, A. Z., Stanek, K. Z., Kudritzki, R. P., Macri, L. M., Sasselov, D. D., Kaluzny, J., Stetson, P. B., Bersier, D., Bresolin, F., Matheson, T., Mochejska, B. J., Przybilla, N., Szentgyorgyi, A. H., Tonry, J., & Torres, G. 2006, *ApJ*, 652, 313
- Bono, G., Caputo, F., Fiorentino, G., Marconi, M., & Musella, I. 2008, *ApJ*, 684, 102
- Bono, G., Marconi, M., & Stellingwerf, R. F. 1999, *ApJS*, 122, 167
- Boyle, W. S. & Wilson, G. E. 1970, *The Bell Systems Technical Journal*, 49, 587
- Brooks, R. S., Wilson, C. D., & Harris, W. E. 2004, *AJ*, 128, 237
- Brunthaler, A., Reid, M. J., Falcke, H., Greenhill, L. J., & Henkel, C. 2005, *Science*, 307, 1440
- Cardelli, J. A., Clayton, G. C., & Mathis, J. S. 1989, *ApJ*, 345, 245
- Chandar, R., Bianchi, L., & Ford, H. C. 1999, *ApJ*, 517, 668

- Coil, A. L., Matheson, T., Filippenko, A. V., Leonard, D. C., Tonry, J., Riess, A. G., Challis, P., Clocchiatti, A., Garnavich, P. M., Hogan, C. J., Jha, S., Kirshner, R. P., Leibundgut, B., Phillips, M. M., Schmidt, B. P., Schommer, R. A., Smith, R. C., Soderberg, A. M., Spyromilio, J., Stubbs, C., Suntzeff, N. B., & Woudt, P. 2000, *ApJ Let.*, 544, L111
- Costa, R. D. D., de Freitas Pacheco, J. A., & Idiart, T. P. 2000, in IAU Symposium, Vol. 198, The Light Elements and their Evolution, ed. L. da Silva, R. de Medeiros, & M. Spite, 234—+
- Crockett, N. R., Garnett, D. R., Massey, P., & Jacoby, G. 2006, *ApJ*, 637, 741
- Feast, M. W. & Catchpole, R. M. 1997, *MNRAS*, 286, L1
- Fernie, J. D., Evans, N. R., Beattie, B., & Seager, S. 1995, Information Bulletin on Variable Stars, 4148, 1
- Ferrarese, L., Silbermann, N. A., Mould, J. R., Stetson, P. B., Saha, A., Freedman, W. L., & Kennicutt, Jr., R. C. 2000, *PASP*, 112, 177
- Fouqué, P., Arriagada, P., Storm, J., Barnes, T. G., Nardetto, N., Mérand, A., Kervella, P., Gieren, W., Bersier, D., Benedict, G. F., & McArthur, B. E. 2007, *A&A*, 476, 73
- Freedman, W. L. & Madore, B. F. 1990, *ApJ*, 365, 186
- Freedman, W. L., Madore, B. F., Gibson, B. K., Ferrarese, L., Kelson, D. D., Sakai, S., Mould, J. R., Kennicutt, Jr., R. C., Ford, H. C., Graham, J. A., Huchra, J. P., Hughes, S. M. G., Illingworth, G. D., Macri, L. M., & Stetson, P. B. 2001, *ApJ*, 553, 47
- Freedman, W. L., Wilson, C. D., & Madore, B. F. 1991, *ApJ*, 372, 455
- Galleti, S., Bellazzini, M., & Ferraro, F. R. 2004, *A&A*, 423, 925
- Gascoigne, S. C. B. 1974, *MNRAS*, 166, 25P
- Girardi, L., Bertelli, G., Bressan, A., Chiosi, C., Groenewegen, M. A. T., Marigo, P., Salasnich, B., & Weiss, A. 2002, *A&A*, 391, 195

- Girardi, L., Grebel, E. K., Odenkirchen, M., & Chiosi, C. 2004, A&A, 422, 205
- Goodricke, J. & Bayer. 1786, Royal Society of London Philosophical Transactions Series I, 76, 48
- Groenewegen, M. A. T. & Oudmaijer, R. D. 2000, A&A, 356, 849
- Hansen, C. J., Kawaler, S. D., & Trimble, V. 2004, Stellar interiors : physical principles, structure, and evolution, ed. C. J. Hansen, S. D. Kawaler, & V. Trimble
- Hartman, J. D., Bersier, D., Stanek, K. Z., Beaulieu, J.-P., Kaluzny, J., Marquette, J.-B., Stetson, P. B., & Schwarzenberg-Czerny, A. 2006, MNRAS, 371, 1405
- Herrnstein, J. R., Moran, J. M., Greenhill, L. J., Diamond, P. J., Inoue, M., Nakai, N., Miyoshi, M., Henkel, C., & Riess, A. 1999, Nature, 400, 539
- Howell, S. B. 1993, in IAU Colloq. 136: Stellar Photometry - Current Techniques and Future Developments, ed. C. J. Butler & I. Elliott, 318–+
- Howell, S. B. 2006, Handbook of CCD astronomy, ed. S. B. Howell
- Hubble, E. 1929, Proceedings of the National Academy of Science, 15, 168
- Hubble, E. P. 1926, ApJ, 63, 236
- Jester, S., Schneider, D. P., Richards, G. T., Green, R. F., Schmidt, M., Hall, P. B., Strauss, M. A., Vanden Berk, D. E., Stoughton, C., Gunn, J. E., Brinkmann, J., Kent, S. M., Smith, J. A., Tucker, D. L., & Yanny, B. 2005, AJ, 130, 873
- Keller, S. C. & Wood, P. R. 2006, ApJ, 642, 834
- Kennicutt, Jr., R. C., Stetson, P. B., Saha, A., Kelson, D., Rawson, D. M., Sakai, S., Madore, B. F., Mould, J. R., Freedman, W. L., Bresolin, F., Ferrarese, L., Ford, H., Gibson, B. K., Graham, J. A., Han, M., Harding, P., Hoessel, J. G., Huchra, J. P., Hughes, S. M. G., Illingworth, G. D., Macri, L. M., Phelps, R. L., Silbermann, N. A., Turner, A. M., & Wood, P. R. 1998, ApJ, 498, 181
- Kim, M., Kim, E., Lee, M. G., Sarajedini, A., & Geisler, D. 2002, AJ, 123, 244

- Kowal, C. T. 1968, AJ, 73, 1021
- Kudritzki, R.-P., Urbaneja, M. A., Bresolin, F., Przybilla, N., Gieren, W., & Pietrzyński, G. 2008, ApJ, 681, 269
- Landolt, A. U. 1992, AJ, 104, 340
- Leavitt, H. S. & Pickering, E. C. 1912, Harvard College Observatory Circular, 173, 1
- Lee, M. G., Kim, M., Sarajedini, A., Geisler, D., & Gieren, W. 2002, ApJ, 565, 959
- Lejeune, T. & Schaerer, D. 2001, A&A, 366, 538
- Lupton, R. H., Ivezić, Z., Gunn, J. E., Knapp, G., Strauss, M. A., & Yasuda, N. 2002, in Society of Photo-Optical Instrumentation Engineers (SPIE) Conference Series, Vol. 4836, Society of Photo-Optical Instrumentation Engineers (SPIE) Conference Series, ed. J. A. Tyson & S. Wolff, 350–356
- Macri, L. M., Stanek, K. Z., Bersier, D., Greenhill, L. J., & Reid, M. J. 2006, ApJ, 652, 1133
- Madore, B. F. 1976, in Royal Greenwich Observatory Bulletin, Vol. 182, The Galaxy and the Local Group, ed. R. J. Dickens, J. E. Perry, F. G. Smith, & I. R. King, 153–+
- Madore, B. F. & Freedman, W. L. 2009, ApJ, 696, 1498
- Magrini, L., Stanghellini, L., & Villaver, E. 2009, ApJ, 696, 729
- Magrini, L., Vílchez, J. M., Mampaso, A., Corradi, R. L. M., & Leisy, P. 2007, A&A, 470, 865
- Massey, P., Olsen, K. A. G., Hodge, P. W., Strong, S. B., Jacoby, G. H., Schlingman, W., & Smith, R. C. 2006, AJ, 131, 2478
- McConnachie, A. W., Irwin, M. J., Ferguson, A. M. N., Ibata, R. A., Lewis, G. F., & Tanvir, N. 2004, MNRAS, 350, 243

- Monet, D. G., Levine, S. E., Canzian, B., Ables, H. D., Bird, A. R., Dahn, C. C., Guetter, H. H., Harris, H. C., Henden, A. A., Leggett, S. K., Levison, H. F., Luginbuhl, C. B., Martini, J., Monet, A. K. B., Munn, J. A., Pier, J. R., Rhodes, A. R., Riepe, B., Sell, S., Stone, R. C., Vrba, F. J., Walker, R. L., Westerhout, G., Brucato, R. J., Reid, I. N., Schoening, W., Hartley, M., Read, M. A., & Tritton, S. B. 2003, AJ, 125, 984
- Moskalik, P., Buchler, J. R., & Marom, A. 1992, ApJ, 385, 685
- Ngeow, C. & Kanbur, S. M. 2007, ApJ, 667, 35
- Ngeow, C.-C., Kanbur, S. M., Neilson, H. R., Nanthakumar, A., & Buonaccorsi, J. 2009, ApJ, 693, 691
- Onaka, P., Tonry, J. L., Isani, S., Lee, A., Uyeshiro, R., Rae, C., Robertson, L., & Ching, G. 2008, in Society of Photo-Optical Instrumentation Engineers (SPIE) Conference Series, Vol. 7014, Society of Photo-Optical Instrumentation Engineers (SPIE) Conference Series
- Petersen, J. O. 1973, A&A, 27, 89
- Phillips, M. M. 1993, ApJ Let., 413, L105
- Pietrzyński, G., Gieren, W., Fouqué, P., & Pont, F. 2002, AJ, 123, 789
- Rosolowsky, E. & Simon, J. D. 2008, ApJ, 675, 1213
- Sakai, S., Ferrarese, L., Kennicutt, Jr., R. C., & Saha, A. 2004, ApJ, 608, 42
- Sandage, A., Bell, R. A., & Tripicco, M. J. 1999, ApJ, 522, 250
- Sandage, A. & Tammann, G. A. 1968, ApJ, 151, 531
- Sandage, A., Tammann, G. A., & Reindl, B. 2004, A&A, 424, 43
- Sasselov, D. D., Beaulieu, J. P., Renault, C., Grison, P., Ferlet, R., Vidal-Madjar, A., Maurice, E., Prevot, L., Aubourg, E., Bareyre, P., Brehin, S., Coutures, C., De-labrouille, N., de Kat, J., Gros, M., Laurent, B., Lachieze-Rey, M., Lesquoy, E.,

- Magneville, C., Milsztajn, A., Moscoso, L., Queinnec, F., Rich, J., Spiro, M., Vignoux, L., Zylberajch, S., Ansari, R., Cavalier, F., Moniez, M., Gry, C., Guibert, J., Moreau, O., & Tajhmady, F. 1997, A&A, 324, 471
- Schechter, P. L., Mateo, M., & Saha, A. 1993, PASP, 105, 1342
- Schlegel, D. J., Finkbeiner, D. P., & Davis, M. 1998, ApJ, 500, 525
- Simon, N. R. & Lee, A. S. 1981, ApJ, 248, 291
- Soszynski, I., Poleski, R., Udalski, A., Szymanski, M. K., Kubiak, M., Pietrzynski, G., Wyrzykowski, L., Szewczyk, O., & Ulaczyk, K. 2008, Acta Astronomica, 58, 163
- Stebbins, J. & Brown, F. C. 1907, ApJ, 26, 326
- Stetson, P. B. 1987, PASP, 99, 191
- . 1990, PASP, 102, 932
- . 1994, PASP, 106, 250
- . 2005, PASP, 117, 563
- Stothers, R. B. 1988, ApJ, 329, 712
- Stuart, A. & Ord, J. K. 1991, Kendall's Advanced Theory of Statistics, 5th Edition, Volume 2: Classical Inference and Relationship
- Szabados, L. 2003, in Astronomical Society of the Pacific Conference Series, Vol. 298, GAIA Spectroscopy: Science and Technology, ed. U. Munari, 237–+
- Tomaney, A. B. & Croots, A. P. S. 1996, AJ, 112, 2872
- Tonry, J. & Schneider, D. P. 1988, AJ, 96, 807
- Tully, R. B. & Fisher, J. R. 1977, A&A, 54, 661
- U, V., Urbaneja, M. A., Kudritzki, R., Jacobs, B. A., Bresolin, F., & Przyilla, N. 2009, ApJ, 704, 1120

- Udalski, A., Soszynski, I., Szymanski, M., Kubiak, M., Pietrzynski, G., Wozniak, P., & Zebrun, K. 1999a, *Acta Astronomica*, 49, 223
- . 1999b, *Acta Astronomica*, 49, 437
- Udalski, A., Szymanski, M., Kaluzny, J., Kubiak, M., & Mateo, M. 1992, *Acta Astronomica*, 42, 253
- van Leeuwen, F., Feast, M. W., Whitelock, P. A., & Laney, C. D. 2007, *MNRAS*, 379, 723
- Zaritsky, D., Kennicutt, Jr., R. C., & Huchra, J. P. 1994, *ApJ*, 420, 87